Stony Brook University

OFFICIAL COPY

The official electronic file of this thesis or dissertation is maintained by the University Libraries on behalf of The Graduate School at Stony Brook University.

© All Rights Reserved by Author.

Systematic studies of soft direct photon production in Au+Au collisions at $\sqrt{s_{\mathrm{NN}}} = 200\,\mathrm{GeV}$

A Dissertation presented

by

Benjamin Bannier

to

The Graduate School

in Partial Fulfillment of the

Requirements

for the Degree of

Doctor of Philosophy

in

Physics

Stony Brook University

May 2014

Stony Brook University

The Graduate School

Benjamin Bannier

We, the dissertation committee for the above candidate for the

Doctor of Philosophy degree, hereby recommend

acceptance of this dissertation

Axel Drees — Dissertation Advisor
Professor, Department of Physics and Astronomy

Alan Calder — Chairperson of Defense
Professor, Department of Physics and Astronomy

Edward Shuryak
Professor, Department of Physics and Astronomy

Takao Sakaguchi
Physicist, Brookhaven National Laboratory

This dissertation is accepted by the Graduate School

Charles Taber
Dean of the Graduate School

Abstract of the Dissertation

Systematic studies of soft direct photon production in Au+Au collisions at $\sqrt{s_{\mathrm{NN}}} = 200\,\mathrm{GeV}$

by

Benjamin Bannier

Doctor of Philosophy

in

Physics

Stony Brook University

2014

Direct photons are produced during all stages of a heavy-ion collision. Due to their very small interaction cross section with the dense hadronic medium, they can escape the collision almost undisturbed and transport information about their production environment to a detector making them an excellent probe in heavy-ion physics.

The observation of both a large yield and strong elliptical flow v_2 of soft direct photons in heavy ion collisions at RHIC has sparked a lot of interest. While a large yield seems to point towards abundant production from the early, hot stages of the interaction, large elliptical flow can be better understood in a picture of predominately late production when the overall flow of the medium has built up. Telling different production scenarios for soft direct photons apart has be difficult.

We map out the centrality-dependence of direct photon observables and present results for dependence of the soft direct photon yield and flow as functions of centrality in the momentum range $0.4\,\mathrm{GeV}/c < p_T < 5.0\,\mathrm{GeV}/c$ from a sample of externally converted photons. Here we exploit the good momentum resolution of our detector for charged particles at low momenta

and reconstruct photons in electron-positron pairs from conversions in specific locations in the detector material. We find that the yield of soft direct photons has approximately a power-law dependence on the number of participants in the collision, and that their flow is en par with the flow of photons from hadron decays, indicative of relatively late production.

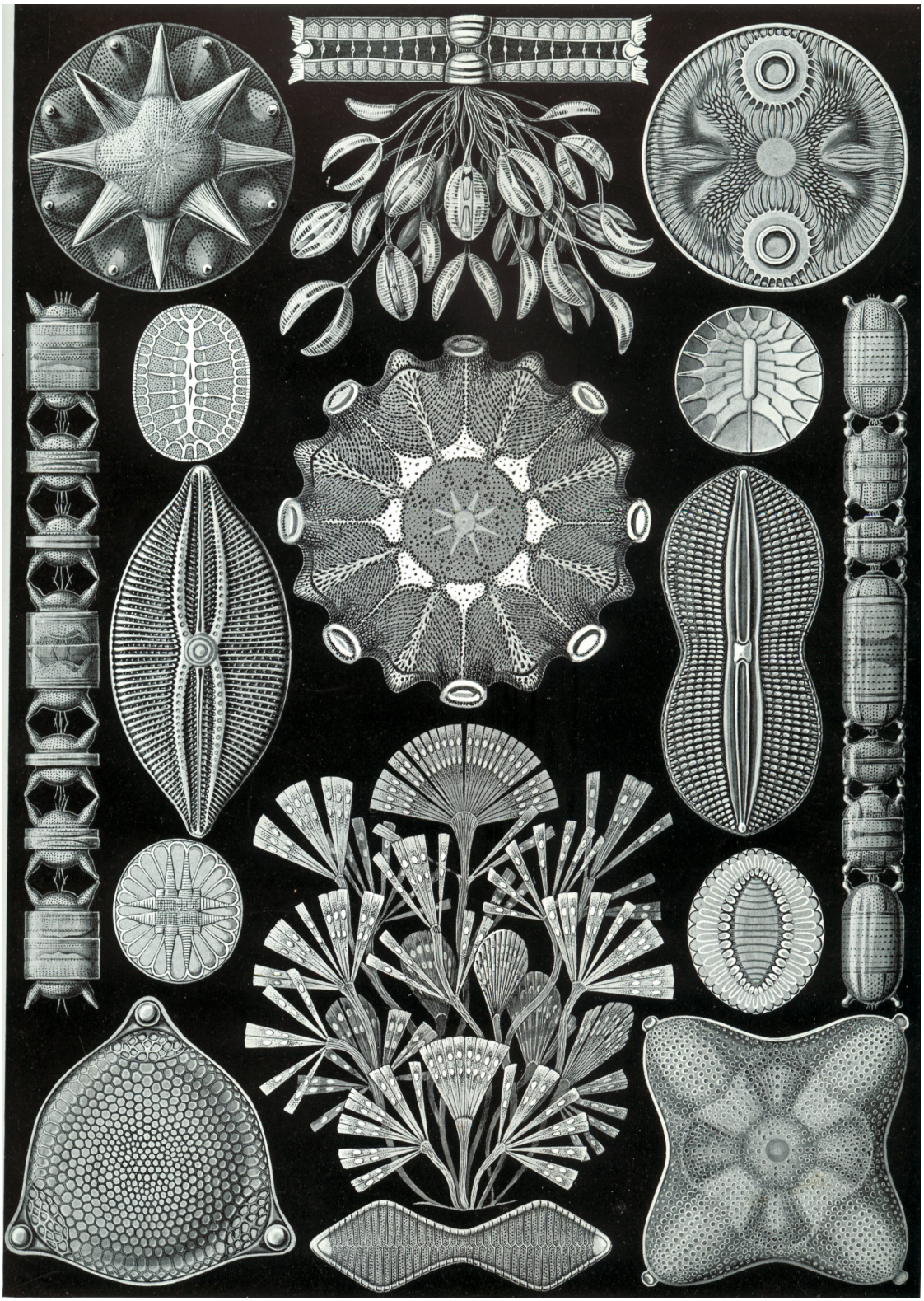

"*Diatomae*", in E. Häckel, *Kunstformen der Natur*, Bibliographisches Institut, Leipzig and Vienna, 1904

Contents

I Introduction 1

1 Introduction 2
- 1.1 Motivation . . . 2
- 1.2 Direct photons in heavy-ion collisions . . . 4
- 1.3 Models of direct photon production . . . 8
- 1.4 The direct photon flow puzzle . . . 11

2 The PHENIX experiment 15
- 2.1 Global detectors . . . 15
- 2.2 Central arm detectors . . . 20

II Data analysis 26

3 The relative direct photon yield R_γ 27
- 3.1 Event selection . . . 29
- 3.2 Inclusive photon sample . . . 29
  - 3.2.1 Single track cuts . . . 31
  - 3.2.2 Pair cuts . . . 32
- 3.3 π^0-tagged photons . . . 34
- 3.4 The conditional acceptance $\langle \varepsilon f \rangle$ . . . 47
  - 3.4.1 Base converted photon sample . . . 47
  - 3.4.2 Fast Monte Carlo for $\langle \varepsilon f \rangle$ . . . 48
- 3.5 Cocktail of hadronic photon sources . . . 54
- 3.6 R_γ results from the 2010 data set . . . 60
- 3.7 The 2010 and 2007 R_γ results . . . 66
- 3.8 Summary . . . 74

4 Direct photon flow 75
- 4.1 Method . . . 75
  - 4.1.1 Measurements of anisotropies . . . 75

4.1.2 Resolution corrections 76
4.1.3 Direct photon v_n 76
4.1.4 Propagation of uncertainties 77
4.2 Analysis 78
4.2.1 Resolution corrections 78
4.2.2 Measurements of anisotropies v_n 78
4.2.3 v_n for photons from hadron decays 80
4.2.4 Direct photon v_n 86

III Discussion **91**

5 Discussion of the measurements **92**
5.1 Direct photon momentum spectra 92
5.2 Excess photon momentum spectra 92
5.3 N_{part}-dependence of the excess photon yield 97
5.4 Anisotropies v_2 and v_3 in a larger momentum range 99

6 Comparisons with models **103**
6.1 The direct photon yield 103
6.2 Centrality-dependence of the direct photon yield 103
6.3 The direct photon v_2 and v_3 106

7 Summary and Outlook **109**

Bibliography **112**

List of Figures

1.1 Collision geometry in nucleus-nucleus collisions . . . 3
1.2 Nuclear modification factor R_{AA} for a number of different probes . . . 5
1.3 Yield of direct photons in $p+p$, Au+Au and Pb+Pb collisions . . . 7
1.4 Direct photon elliptical flow v_2 in Au+Au collisions . . . 9
1.5 Predictions in the model by Linnyk *et al.* . . . 11
1.6 Predictions in the model by van Hees *et al.* . . . 12
1.7 Predictions in the model by Holopainen *et al.* . . . 13

2.1 Schematic overview of the PHENIX detector in 2010 . . . 16
2.2 Schematic overview of the locations of global detectors . . . 18
2.3 Determination of centrality from the BBC charge sum . . . 18
2.4 Schematic diagram of the reaction plane detectors . . . 19
2.5 Schematic overview of a single drift chamber sector . . . 22
2.6 Definitions of angles used in tracking . . . 24

3.1 Drift chamber deadmaps (data) . . . 33
3.2 Pair mass under different vertex assumptions . . . 35
3.3 Statistical uncertainty on π^0 yield for different calorimeter selections . . . 37
3.4 Foreground and normalized background for the 0-20% centrality bin . . . 38
3.5 Foreground and normalized background for the 20-40% centrality bin . . . 39
3.6 Foreground and normalized background for the 40-60% centrality bin . . . 40
3.7 Foreground and normalized background for the 60-92% centrality bin . . . 41
3.8 π^0 yield extraction in the 0-20% centrality bin . . . 42
3.9 π^0 yield extraction in the 20-40% centrality bin . . . 43
3.10 π^0 yield extraction in the 40-60% centrality bin . . . 44
3.11 π^0 yield extraction in the 60-92% centrality bin . . . 45
3.12 Extracted π^0 yield with different background assumptions . . . 46
3.13 Drift chamber deadmaps (simulation) . . . 49
3.14 Single photon efficiency ε . . . 52
3.15 Conditional acceptance $\langle \varepsilon f \rangle$ . . . 55
3.16 Experimental m_T spectra . . . 57

3.17 m_T-scaling assumption for the η 57
3.18 Cocktail ratio in $p+p$ using Hagedorn and Tsallis parametrizations . . 58
3.19 Systematic uncertainty in cocktail ratio for meson/π^0 ratios 60
3.20 Simulated converted photon spectra 61
3.21 Simulated cocktail ratios 62
3.22 Data ratios $Y_{\gamma}^{\text{incl}}/Y_{\gamma}^{\pi^0}$ 64
3.23 Centrality-dependent R_{γ} results 65
3.24 Centrality-dependent R_{γ} for different EMCal photon p_T cuts 67
3.25 ϕ distribution of reconstructed converted photons 68
3.26 Centrality-dependent R_{γ} results in narrower acceptance 68
3.27 Comparisons of 2007 $\langle \varepsilon f \rangle$ calculations 70
3.28 Data ratios for different data sets and $\langle \varepsilon f \rangle$ methods 71
3.29 R_{γ} for different data sets and $\langle \varepsilon f \rangle$ methods (1) 72
3.30 R_{γ} for different data sets and $\langle \varepsilon f \rangle$ methods (2) 73
3.31 R_{γ} for different data sets and $\langle \varepsilon f \rangle$ methods (minimum bias) 74

4.1 Resolution corrections for the RXP and MPC 79
4.2 Charged track v_2 81
4.3 Charged track v_3 82
4.4 Charged track v_4 83
4.5 Inclusive photon v_n 84
4.6 Inclusive photon v_n in combined centrality bins 87
4.7 Simulated pion v_2 87
4.8 Simulated pion v_3 88
4.9 Simulated pion $v_4\{\Psi_2\}$ 88
4.10 Direct photon v_n 89
4.11 Direct photon v_n in combined centrality bins. 90

5.1 Direct photon p_T spectra for different centralities 93
5.2 Direct photon p_T spectra in Au+Au minimum bias and $p+p$ collisions 94
5.3 Excess photon p_T spectra for different centralities 96
5.4 Excess photon p_T spectra in Au+Au minimum bias and $p+p$ collisions 98
5.5 Fit residual of exponential fits 98
5.6 Integrated excess photon yields as functions of N_{part}. 99
5.7 Integrated excess photon yields as functions of N_{qpart}. 100
5.8 Comparison of our direct photon v_2 with the published PHENIX result 101
5.9 Comparison of the direct photon v_2 with the preliminary PHENIX result 101
5.10 Direct photon v_n from conversions and calorimeter 102

6.1 Direct photon p_T spectra compared to different model calculations . . . 104
6.2 Ratio of p_T spectra and different model calculations 105

6.3 Comparison of our v_2 measurement with model predictions 107
6.4 Elliptic and triangular flow v_2 and v_3 in the calculation by Shen *et al.* . . 108
6.5 Elliptical flow of direct photons in the model by Müller *et al.* 108

7.1 Direct photon yield in Au+Au and d+Au collisions 111

List of Tables

3.1 Photon production channels in the cocktail simulation 56
3.2 Hagedorn parameterizations of π^0 p_T spectra for centrality classes 59
3.3 Meson yields relative to π^0 yield 59
3.4 Summary of systematic uncertainties on R_γ 63

5.1 N_{coll}, N_{part} and N_{qpart} for centralities, inverse slopes of excess photon spectra 95

6.1 Power in the N_{part}-dependence of the direct photon yield 106

Acknowledgement

This thesis would not have been possible without the help of numerous people. My thesis advisor Axel Drees always believed in this analysis and strongly supported my work through difficult times and encouraged me finding my own approach. His strong intuition both in the face of minute details as well regarding the grand picture has made this thesis possible and profoundly formed me personally. I profited immensely from the support of my collaborators, especially to understand details of the apparatus or measurement techniques. In particular the close collaboration with Richard Petti was extremely fruitful and our many discussions have given me a better understanding. Last and foremost this thesis would not have been possible without the strong support of my wife Madlen and my parents who always backed up my endeavors in life and science.

Part I

Introduction

Chapter 1

Introduction

1.1 Motivation

One of the central questions in Heavy Ion Physics is how strongly interacting matter behaves under extreme conditions, i.e. at high temperatures or large densities. As more and more energy is added to a hadronic system an exponential increase in the number of resonances is observed [1, 2], which implies a limiting temperature $T_H \approx 174\,\mathrm{MeV}$[1] for the resonance picture of hadronic matter: when one approaches T_H less and less of the energy added to the system is used to increase its temperature but instead leads to formation of a growing number of resonance states; this also implies that above T_H hadronic resonances cannot be the relevant degrees of freedom and a crossover or phase transition to a Quark Gluon Plasma (QGP) phase is expected [3]. In the QGP picture of hot hadronic matter the relevant degrees of freedom are colored partons (quarks and gluons, or colored composite objects) instead of color-neutral resonances.

The Relativistic Heavy Ion Collider (RHIC) at the Brookhaven National Laboratory (BNL) was explicitly built to create QGP systems and study their properties. Experiments at RHIC have collected compelling evidence for the production of a new strongly interacting state of matter [4–7], i.a.

Elliptic flow: The initial state in nucleus-nucleus collision with non-zero impact parameter $b \neq 0$ is not spatially symmetric but instead almond-shaped, see Fig. 1.1. It has been found that the momentum distributions of soft particles produced in heavy-ion collisions depend on the emission angle with respect to the impact parameter plane. Here the particle momenta are modified by the collective velocity (flow) of particles. The observed efficient transformation of initial state spatial anisotropies into final state momentum anisotropies can be understood in a hydrodynamic picture which describes the produced medium as a near-perfect fluid. There initial state

[1] The temperature is given here in the conventional units where the Boltzmann constant $k \equiv 1$.

density anisotropies (density gradients) can be related to momentum anisotropies (pressure gradients) with the help of the equation of state (EoS) of the medium.

Rapid thermalization: The observed correlation lengths of particles in heavy-ion collisions, which can be accessed utilizing the Hanbury, Brown and Twiss (HBT) method [8, 9], show that the relevant source radii are relatively small, indicating thermalization of the medium on very short timescales, τ fractions of fm/c.

Jet quenching: High-energy jets passing through the medium are seen to be strongly modified, up to the point of them being completely quenched. This is indicative of them interacting with a dense, strongly interaction medium.

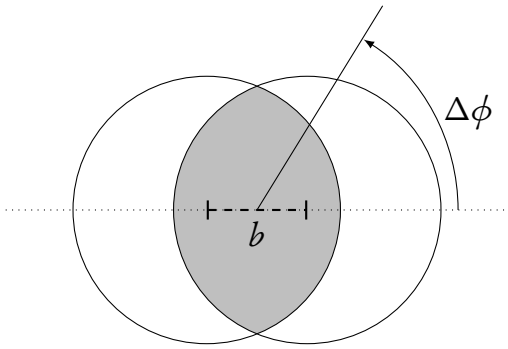

Figure 1.1: Collision geometry in a nucleus-nucleus collision in the transverse plane. Circles denote nuclei moving towards and away from the viewer with the beam direction perpendicular to the paper. Due to their large momenta at RHIC nuclei appear strongly Lorentz-contracted in the laboratory frame. The length of the dashed line connecting the centers of the two nuclei defines the impact parameter b. Together with the beam direction it defines the reaction plane. Emission angles $\Delta\phi$ of particles can be measured against the reaction plane. The array shaded gray is the almond-shaped overlap region with nucleons participating in the collision. For $b = 0$ its shape is circular and becomes more asymmetric with increasing b. The amount of overlap determines the *centrality* of the collisions: collisions with small b are called *central*, and those with large b (with still overlapping nuclei) *peripheral*. Due to the Lorentz-contraction of the nuclei regions near the top and bottom of the overlap region have lower densities than regions in the impact parameter plane.

The probes used to study heavy-ion collisions can roughly be grouped into two categories,

Final state probes, which are typically soft hadrons produced late in the reaction and are sensitive to the collective motion of the system. While soft hadrons are produced during all stages of the collision their interaction cross sections with the hadronic

medium are large so that only hadrons produced late near the *freeze-out surface* can escape the collision and reach detectors without interaction, and

Penetrating probes which carry information about the interior of the collision system. They can be accessed by relating final state hadrons to partons or hadrons in the medium, or be electromagnetic probes like leptons and photons which do not participate in the strong interaction and can escape the collision with effectively no final state interaction.

While final state probes allow to quantify the collective motion and to study correlations to extract information about medium properties, penetracting probes can be used to study the full time evolution of the collision. The goal of this thesis is to study the production of soft direct photons in heavy-ion collisions.

1.2 Direct photons in heavy-ion collisions

Photons are penetrating, electromagnetic probes produced during all stages of a heavy-ion collision. Since photons carry no color charge they do not interact strongly with the hadronic medium and carry information about their production environment practically unmodified to a detector. In heavy-ion collisions photons are produced in a number of processes during all times of the collision, i.a.

1. In the initial hard scattering of partons in the colliding nuclei $\tau \sim 0$ photons are produced primarily in hard scattering processes of partons like quark annihilation $q + \bar{q} \rightarrow g + \gamma$, quark-gluon scattering $q(\bar{q}) + g \rightarrow q(\bar{q}) + \gamma$, quark-quark scattering $q + q \rightarrow q + q + \gamma$ and gluon fusion $g + g \rightarrow \gamma$ processes.

2. In the pre-equilibrium phase $\tau < 1\,\mathrm{fm}/c$ photons can be produced from quarks in the medium.

3. In QGP and hadron gas phase $\tau \approx 1 - 10\,\mathrm{fm}/c$ photons can be produced in scattering processes of the medium's colored, strongly interacting degrees of freedom.

4. In the hadron gas phase after hadronization $\tau \approx 10 - 100\,\mathrm{fm}/c$ photons can be produced in scattering processes involving hadrons, e.g. meson-meson and meson-baryon Bremsstrahlung $m + m \rightarrow m + m\gamma$ and $m + B \rightarrow m + B\gamma$.

5. Photons are produced in decays of short- and long-lived hadrons, $h \rightarrow X\gamma$.

Of particular interest are *direct photons*, which are photons not originating from decays of hadrons. While photons from hadron decays can be understood by studying the spectra of hadrons, direct photons directly probe the conditions of their production environment

and carry information about e.g. the local temperature or flow velocity. Similarly, photons produced in hard processes can be understood by studying their production in elementary collisions of hadrons like $p+p$; their yield can be calculated by properly accounting for the number of hard collisions N_{coll} occurring in a particular heavy-ion collision which allows to isolate medium-induced components of the direct photon measurement.

The direct photon yield

As a baseline testing our understanding of Quantum Chromodynamics (QCD) in heavy-ion collisions, hard photons with large momenta have been measured, see Fig. 1.2. These photons carry too much momentum to be produced from late scattering processes of hadrons or from hadron decays; instead they are predominately created in early, hard scattering processes involving partons. The yield of hard photons with $p_T > 5\,\text{GeV}/c$ produced in Au+Au collisions is experimentally consistent with the yield expected from interactions in the vacuum as observed in $p+p$ collisions when taking the number of binary collisions among nucleons N_{coll} into account.

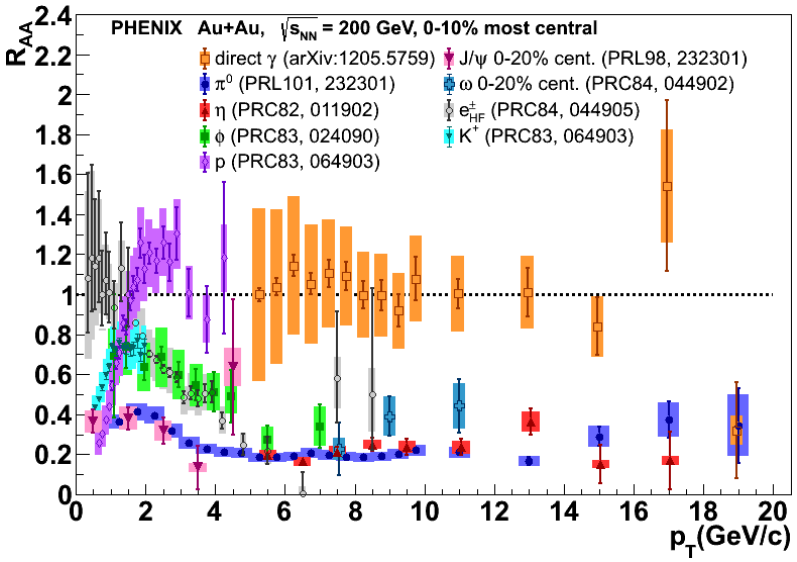

Figure 1.2: Nuclear modification factor R_{AA} for a number of different probes in most central Au+Au collisions [10]. Photons are plotted as open squares. R_{AA} is the ratio of the yield seen in Au+Au collisions to the yield from $p+p$ collisions scaled by the number of binary collisions N_{coll} in Au+Au. High p_T photons behave like expected from $p+p$ collisions, i.e. their R_{AA} is consistent with unity.

The situation is different for soft, low momentum photons that can be produced in all processes listed above. To isolate medium-induced effects one typically removes the sizable contribution from hadron decays and directly examines the direct photon signal.

If the momentum of the photons is not much larger than the typical energy density, but still large compared to the typical local velocity of the medium, their properties can on a simplistic, macroscopic level be understood with an analogy to a black body radiator. One expects their yield to depend on the temperature analogous to a Stefan-Boltzmann law

$$j \propto T^4 \tag{1.1}$$

where j is the radiated power and T the temperature of the medium, so that hotter, earlier phases of the interaction should produce the bulk of the photon yield. The momentum spectra would be described by Maxwell-Boltzmann-like distributions

$$\frac{\mathrm{d}N(p_T)}{\mathrm{d}p_T} \propto e^{-c\,p_T/T} \tag{1.2}$$

where $p_T = \sqrt{p_x^2 + p_y^2}$ is the transverse momentum of the photon, c the speed of light, $N(p_T)$ the yield of soft photons in the interval $[p_T, p_T + \mathrm{d}p_T]$ and the inverse slope T the typical temperature of the radiating medium in energy units (i.e. we set $k \equiv 1$). The framework for more realistic models is outlined in Section 1.3. Figure 1.3 shows the measured momentum spectra of photons down to $p_T \approx 1\,\mathrm{GeV}/c$ [11]. While the hard part of the spectrum $p_T > 3\,\mathrm{GeV}/c$ is described well by the expectation from hard processes the low-momentum part of the spectrum shows a clear enhancement with exponential shape over the expectation from $p + p$. Given the T^4-dependence of the photon yield of a black-body radiator it is natural to assume that the additional photon signal at low p_T in heavy-ion collisions is predominately due to emission from the earliest, hottest times of the interaction. Indeed, analyses of the inverse slopes in Au+Au extracted $T = 221 \pm 19(\mathrm{stat}) \pm 19(\mathrm{syst})\,\mathrm{MeV}$ [11] and in Pb+Pb $T = 304 \pm 51(\mathrm{stat+sys})$ [12], both well above $T_H \approx 174\,\mathrm{MeV}$, all indicative of soft photon production happening predominately early in the interaction.

The direct photon flow

Another axis to understand the production of soft photons is their correlation with the collision geometry. In off-central heavy-ion collisions the overlap region of the nuclei is not symmetric in the azimuthal angle ϕ but instead of almond shape. With the direction of the impact parameter plane at $\phi_{\mathrm{EP}} = \psi$ defining the event plane, and the angular difference between the photon and the event plane direction $\Delta\phi = \psi - \phi$ one can write the correlation functions as

$$\frac{\mathrm{d}N}{\mathrm{d}(\Delta\phi)} = N_0 \left(1 + \sum_{n=1}^{\infty} 2v_n \cos(n\Delta\phi)\right) \tag{1.3}$$

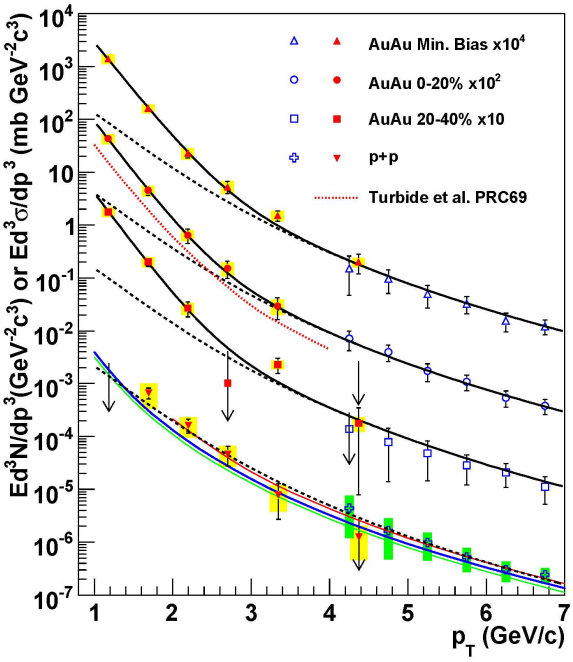

(a) Invariant yield or cross section of direct photons in $p+p$ and Au+Au collisions [11]. The dashed lines show a modified power-law fit to the $p+p$ data, scaled by the number of binary collisions N_{coll}. The black lines are fits to the Au+Au data with an exponential plus the fixed N_{coll}-scaled $p+p$ fit.

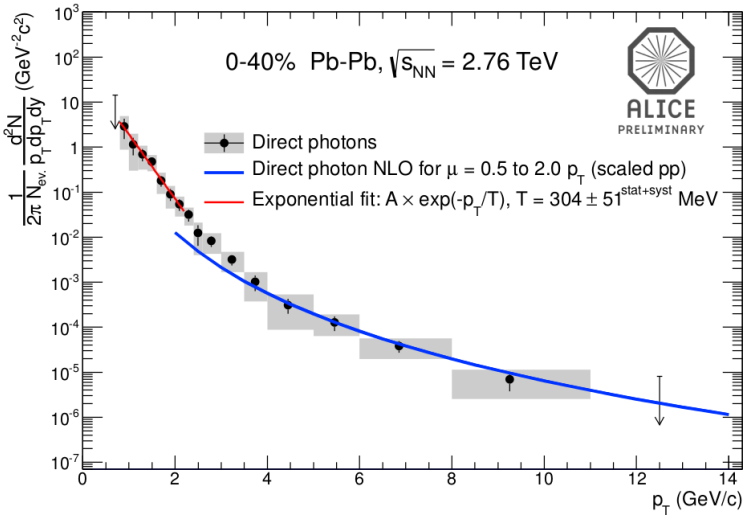

(b) Invariant yield of direct photons in Pb+Pb collisions [12].

Figure 1.3: Invariant yield or cross section of direct photons in $p+p$, Au+Au and Pb+Pb collisions [11, 12]. In heavy-ions systems a clear enhancement of the soft direct photon signal is seen which has roughly exponential shape.

where N is the photon yield in the interval $[\Delta\phi, \Delta\phi + \mathrm{d}\Delta\phi]$, v_n a number of Fourier coefficients and N_0 a constant. For photons completely uncorrelated with the event plane one would expect that all $\Delta\phi$ are equally probably, i.e. all $v_n = 0$. Light hadrons on the other are known to show strong correlation with the event plane with v_2 up to $0.2 \ldots 0.3$, which is understood in a hydrodynamic picture as transformation of initial spatial anisotropies (density gradients) into momentum anisotropies (pressure gradients) manifest in non-flat $\Delta\phi$ distributions happening on relatively long timescales on the order of a couple of fm/c. Consequentially for photons produced early in the collision one would expect small v_n since the flow of the medium has not yet fully developed. On the other hand, direct photons produced in the hadron gas phase are emitted from an already rapidly flowing medium which makes them appear strongly Doppler blue- or redshifted in frequency in the laboratory rest frame when observed along the collective direction of motion of their production environment; by this the collective flow of the hadron gas is imprinted on the photons it produces. In Fig. 1.4 we show results for the elliptical flow v_2 measured in Au+Au collisions [13] where one found v_2 of direct photons to be as large as the flow of hadrons. In the conventional picture of flow buildup taking a couple of fm/c large direct photon flow would indicate that photons are produced late in the interaction.

1.3 Models of direct photon production

A nuclear collision goes through a number of different phases, see the listing on Page 4, with photons being produced at all times. Realistic models of photon production differ in how they prepare the initial state of system, evolve it during the different phases and model their typical interactions, and in how they interpolate different physics descriptions during transition periods. An extensive review of the different models is given in Ref. [14] from which we recall the crucial ingredients in the following.

The initial state

In the initial state of the collision of two heavy ions the two nuclei appear strongly Lorentz-contracted in the collision rest frame. Depending on the centrality of the collision the nuclei overlap to different degrees with large densities in the overlap region. To describe the distribution of partons in the initial state, Glauber or saturation-inspired descriptions are used. For Glauber initial conditions the initial state of the collision is given by smooth nuclear density profiles inside the nuclei (optical Glauber models) or by randomly sampling the initial distribution of individual partons in the colliding nuclei (Monte Carlo Glauber models) [for a comprehensive review see e.g. 15]. In saturation-inspired models [16, 17] the initial state is determined in terms of overpopulated color fields in the strongly accelerated colliding nuclei before the collision. Models allow for event-by-event fluctuations in the initial conditions to varying degrees.

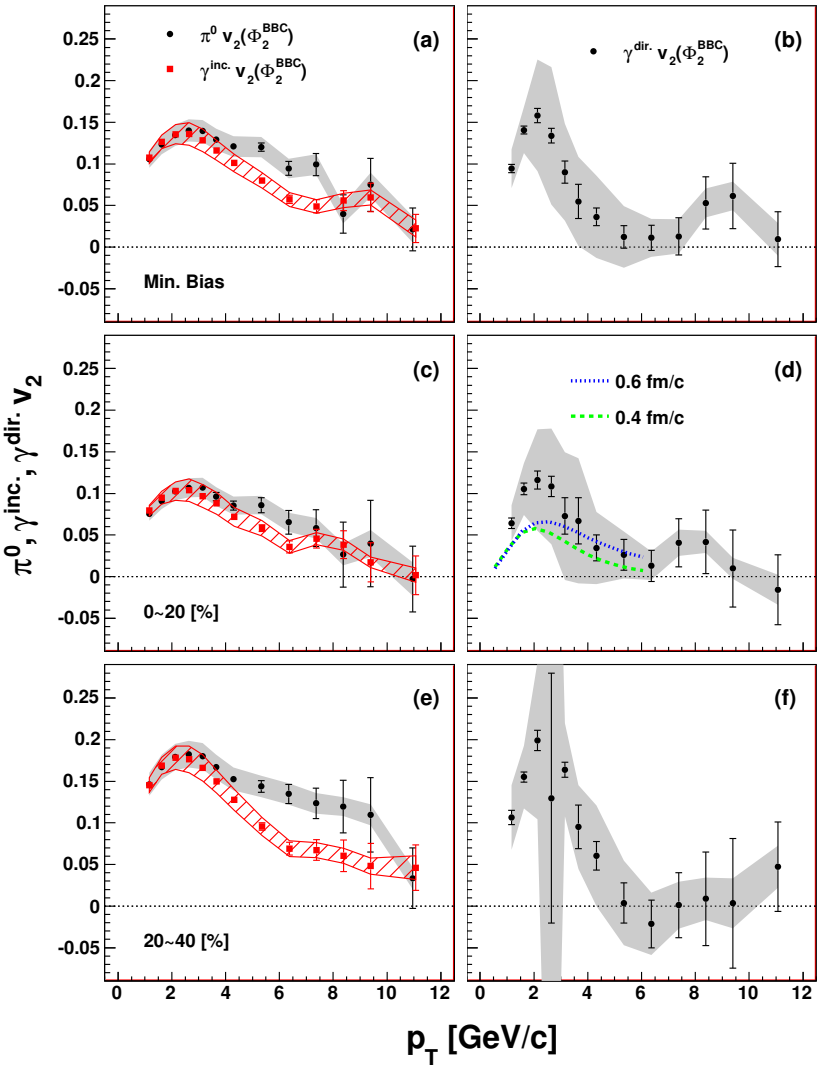

Figure 1.4: Direct photon elliptical flow v_2 in Au+Au collisions [13]. The left column shows results for pions (black circles) and inclusive photons (red squares). The right column show results for direct photons after subtraction of the contribution from hadron decay photons. The different rows show results for minimum bias , most central 0-20%, and mid-central 20-40% collisions. The direct photon v_2 is as large as the pion v_2.

Dynamic evolution during the QGP and Hadron Gas phases

Models can roughly be classified into three categories by how the dynamics of the system are described,

Transport models [18, 19] use solutions of the microscopic transport equations (e.g. Kadanoff-Baym or Boltzmann transport equations) to describe the transport of the individual partons or hadrons of the medium from which the collective behavior emerges; parameterizations or extrapolations of scattering cross sections for all considered particles are a crucial ingredient for transport models.

In Fig. 1.5 we show as an example results for the direct photon yield and flow calculated in the PHSD framework [19]. Since the model explicitly tracks single particles and all their microscopic interactions the authors were able to explicitly examine the individual contribution of each process to the total yield. Similarly, the microscopic treatment of interactions allows to study the dependence on the input parameters of the model, e.g. extrapolated and unmeasured scattering cross sections between hadron resonances.

Fireball models [20, 21] parametrize the collective motion and time evolution of the medium. Photon emission rates in each phase of the collision are also typically parametrized.

An example comparison of the fireball model by van Hees, Gale, and Rapp [21] and experimental data is shown in Fig. 1.6. To constrain the dynamic and flow evolution of the medium the model input was tuned for two different temperatures, $T \simeq 170\,\mathrm{MeV}$ and $T \simeq 100\,\mathrm{MeV}$ with the assumption that dynamics and flow of the medium at the lower temperature is responsible for momentum and flow properties of light hadrons measured experimentally, and similarly the state of the medium at the higher temperature reflected in the final state properties of multi-strange hadrons. This calculation uses photon rates in leading order in the (running) strong coupling constant; photon rates in the hadron gas phase are calculated in an effective theory using a large set of mesonic and baryonic states embedded in a thermal heat bath of hadrons. This calculation does not include Bremsstrahlung processes like $\pi\pi \to \pi\pi\gamma$.

Hydrodynamic models [22–26] describe dynamics in terms of ideal or viscous fluid dynamics in either (2+1)-dimensions in the transverse plane, or in the full (3+1)-dimensional space; here transport coefficients of the medium are crucial inputs.

As an example we show predictions for the direct photon yield and flow from an ideal hydrodynamic model by Holopainen, Räsänen and Eskola [27] in Fig. 1.7. In the hydrodynamic picture of the evolution the authors can study the effect of different equations of state and different assumptions for photon emission rates on the direct photon observables.

All types of models constrain or tune their input parameters to experimental results, currently typically the yields and anisotropies of light or strange hadrons.

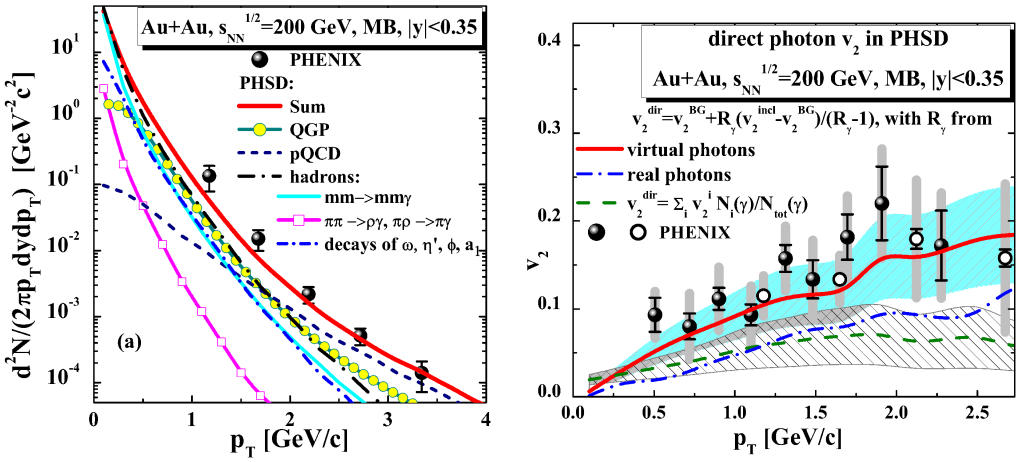

(a) Predictions for the direct photon yield in minimum bias Au+Au collisions. The full line denotes the summed yield from all contributions. The PHENIX data is shown with full circles. Note that the authors include contributions of certain mesons in their direct photon signal which are not included in the experimental data.

(b) Predictions for the direct photon elliptic flow v_2 in minimum bias Au+Au collisions. The dashed lines are predictions for real direct photons calculated with different techniques, see the reference.

Figure 1.5: Direct photon yield and elliptical flow v_2 in minimum bias Au+Au collisions in the transport model by Linnyk, Konchakovski, Cassing and Bratkovskata [28].

Phase transitions

As the rate for photon production is different in the different phases of the interaction how transitions from one to another description are implemented is an important detail for the overall sample of photons predicted. The transition between the QGP and hadron gas phase is typically implemented as rapid cross-over process. Photon production rates are either interpolated in a temperature interval around the transition point or rapidly switched.

1.4 The direct photon flow puzzle

The apparently conflicting information extracted from direct photon measurements has been dubbed the *direct photon flow puzzle*. While the observed large direct photon yield

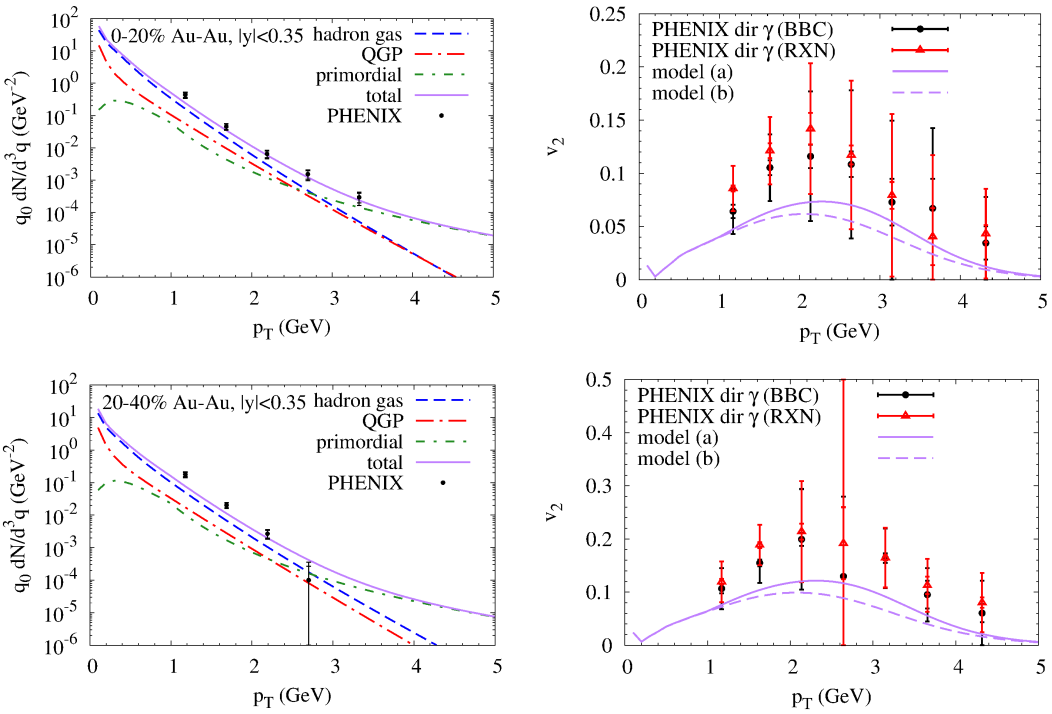

Figure 1.6: Comparison of the fireball model by van Hees, Gale and Rapp [21] to the PHENIX results for the direct photon yield [11] (*left column*) and elliptical flow v_2 [13] (*right column*) for two centrality classes. The predicted summed yield from all sources is given by the full line. The different model predictions for v_2 model (a) and (b) are using different parameterizations for the contribution from hard (primordial) processes.

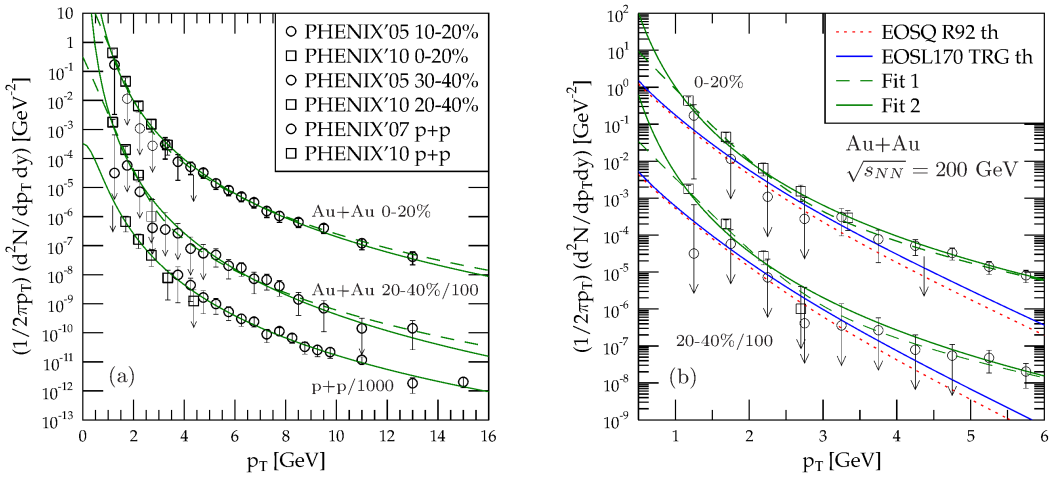

(a) The direct photon yield. The left panel shows power law and exponential+power law fits to the data. The right panel shows predictions from the model.

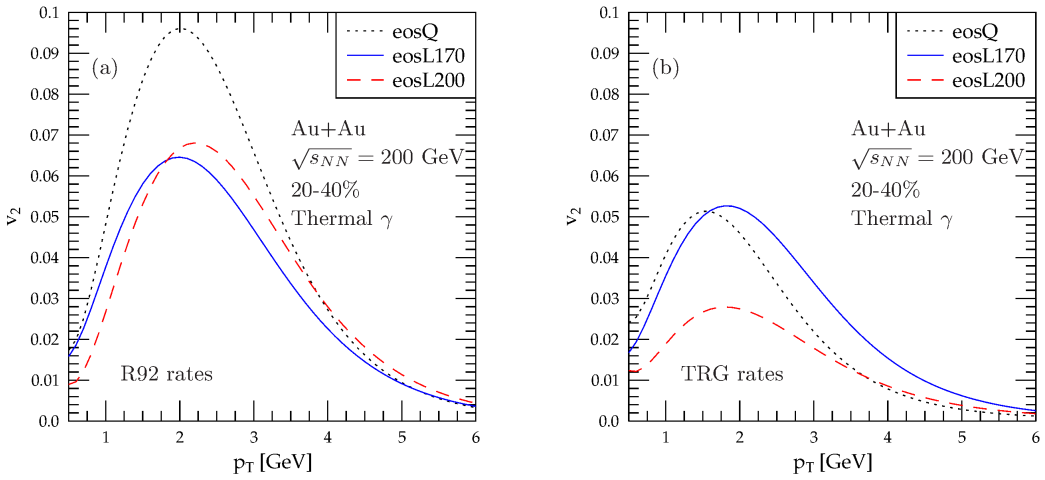

(b) Predictions for the direct photon elliptical flow v_2. *R92* and *TRG* are two different models for photon emission rates in the hadron gas phase, while *eosQ*, *eosL170* and *eosL200* are different EoSs, see the reference for details. The direct photon v_2 is sensitive to the model assumptions.

Figure 1.7: Direct photon yield and elliptical flow v_2 in central Au+Au collisions as predicted in the (2+1) ideal hydrodynamic model of Holopainen, Räsänen and Eskola [27].

seems in the black body analogy indicative of early emission while the medium is hot, their large elliptical flow suggest late production from a hadronic medium whose flow has been build up.

Successful models of direct photon production need to describe both the yield and the flow of direct photons, but existing models have difficulties reaching consistent results in that typically both the elliptical flow and even more so the yield of direct photons are underpredicted by factors of two or more [19, 21, 26]. We have shown comparisons of a few example calculation and data in the previous section in Figs. 1.5 to 1.7. Currently a number of novel approaches are discussed to reconcile models with the experimental data, i.a.

- saturation physics-inspired Glasma models which predict a larger yield of photons originating from the pre-equilibrium phase than conventional models [29],
- fluctuations leading to less smooth initial conditions could create hot and cold spots which when evolved pre-equilibrium can produce flow early in the interaction [24, 25],
- the strong magnetic fields produced in heavy-ion collisions might lead to additional photon production due to the Chiral Magnetic effect [30] or Magneto-Sono-Luminescence [31],

In addition existing frameworks are being reexamined to ensure that e.g. interaction cross sections are up-to-date with the current understanding, or that the modeled quantities do conceptually seamlessly map onto the experimental quantities [14].

To provide additional experimental constraints soft direct photon production can be studied depending on the size of the produced medium (i.e. its dependence on centrality in a heavy-ion system) or with different initial conditions (i.e. in systems like d+Au or Cu+Au), so that the relative contributions of the different mechanisms of direct photon production vary. A successful model should be able to not only simultaneously describe the yield and flow of direct photons in Au+Au collisions, but also its dependence on system size and initial conditions. The goal of this thesis is to study the centrality-dependence of both the direct photon yield and anisotropies. We will use a method using converted photons to extend the covered momentum range to much lower momenta.

Chapter 2

The PHENIX experiment

PHENIX is a large, multipurpose experimental setup installed at the Relativistic Heavy Ion Collider (RHIC) at the Brookhaven National Laboratory (BNL), built specifically to study properties of nuclear matter in A+A, d+A and $p+p$ collisions with hadrons or electromagnetic probes like leptons and photons, as well as to investigate the spin structure of the proton. The detector consists of many specialized subsystems that can perform dedicated measurements, see the schematic drawing in Fig. 2.1 for a global view. Based on their location along the beam axis subsystems are roughly grouped into the central arms, and forward (muon) arms. Additionally, other subsystems measure global properties of the collision like e.g. the time of the collision, its vertex or the particle multiplicity. A very detailed description of the detector is given in [32–38]; in the following we give a brief summary of the global detectors and subsystems used to measure charged particles and photons at midrapidity in 2010.

2.1 Global detectors

The global detectors [36] measure global properties of the event like the time of the collision, its location along the beam axis, or the multiplicity of charged particles. This information is used later to e.g. correlate time information from different subsystems, to reconstruct the trajectories of charged particles, or to classify the centrality of the collision and to the characterize the initial geometry. The locations of the different global detectors are shown schematically in Fig. 2.2 as a function of their location in pseudorapidity $\eta = -\ln\left[\tan\left(\frac{\theta}{2}\right)\right]$.

The Beam-Beam Counters

The Beam-Beam Counters (BBCs) are used to provide a global time of the collision which is used e.g. as a primary trigger, and to measure the collision vertex along the beam axis z. The

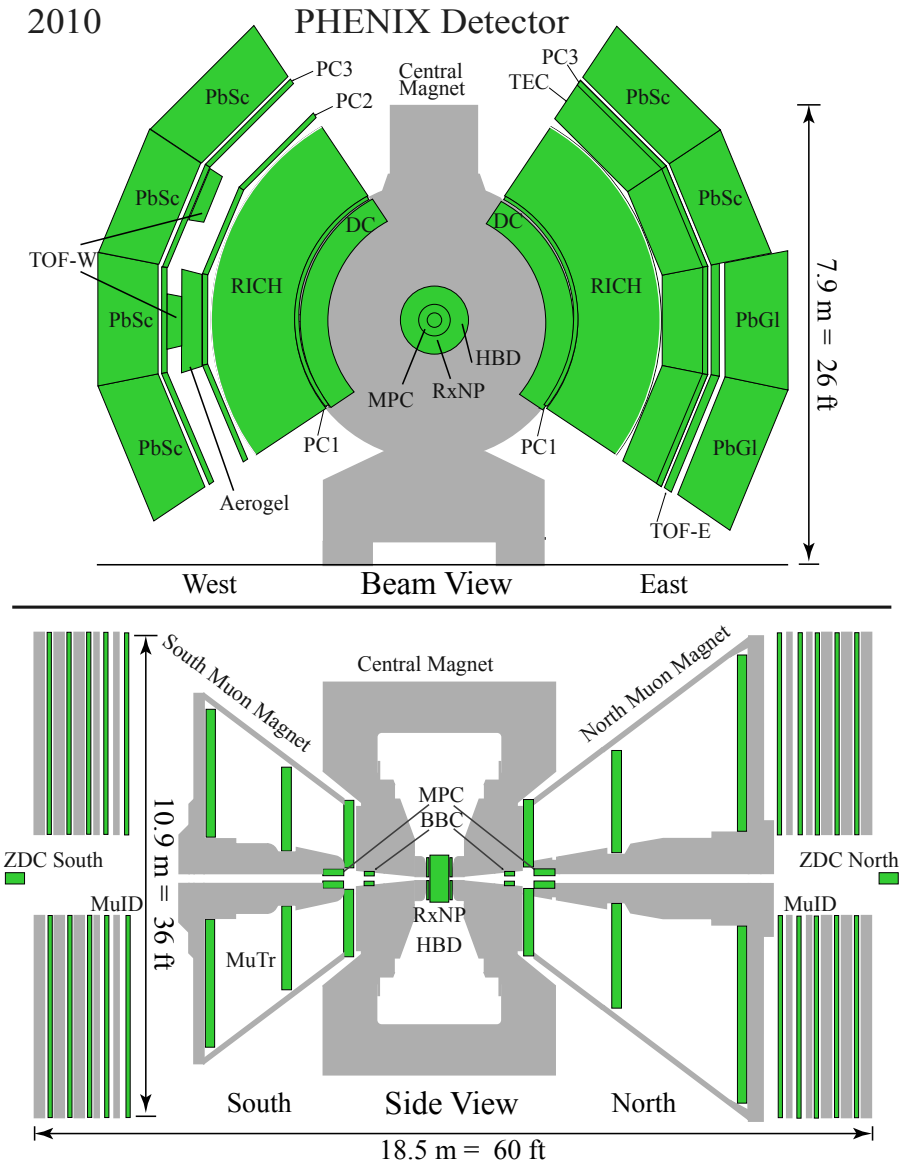

Figure 2.1: Schematic overview of the PHENIX detector setup in 2010. The top panel shows the central arms with the beams running perpendicular to the page with the interaction point in the middle of the detector. The bottom panel shows a side view where the beams enter from the left and collide in the center.

two BBCs are installed ±144 cm from the nominal interaction vertex around the beam pipe. Their acceptance covers the full azimuth and a pseudorapidity range $3.0 < |\eta| < 3.9$. Each BBC consists of 61 2.54 cm×2.54 cm photomultiplier tubes mounted on top of 3 cm quartz crystals which act as Cherenkov radiators. In central Au+Au collisions each element is hit by ∼ 15 particles. Averaging the hit times from each element in a single BBC gives an average arrival time of particles along the beam axis with time resolutions on the order of 60 ps. From the known distance between the BBCs and the arrival times measured in each detector the time of the collision and its vertex along the beam axis z_{vertex} can be calculated. The time information is used to trigger recording of the event with the LVL1 trigger; the vertex position is used in the reconstruction of particle trajectories. To classify the centrality of the collision its monotonic relation to the total charge collected in both BBCs is used. Here the underlying argument is that as collisions become more central, i.e. $b \to 0$, more nucleons participate in the collision and consequentially more particles are produced. By grouping events by the charged collected in the BBC centrality classes can be formed, see Fig. 2.3. Experimentally a certain centrality value quantifies how many events are more central, i.e. create more particles and so also more charge in the BBC, e.g. for a collision classified as 40% more central, 40% of events produce more particles in the final state. In this definition of centrality equally wide classes of centrality contain the same number of events. By recording the BBC charge sum from each event centrality classes can be mapped to BBC charge sum values via the cumulative distribution of the charge.

The Muon Piston Calorimeters

The Muon Piston Calorimeters (MPCs) [40] are two electromagnetic calorimeters installed ±220 cm from the nominal interaction vertex along the beam axis. Both the north and south detectors cover the full angle in azimuth; the north detector can measure in the pseudorapidity range $3.1 < \eta < 3.9$ and the south detector in $-3.7 < \eta < -3.1$. They consist of $PbWO_4$ towers 2.2 cm×2.2 cm large and can be used to measure photons or charged particles at very forward pseudorapidities. We here use the MPC to measure the event planes of the collision: in the transverse plane each tower in the MPC is located in a certain transverse direction ϕ_k from the interaction vertex. The n-th order event plane is then given experimentally by the weighted average of angles ϕ_k with periodicity $\frac{2\pi}{n}$,

$$\psi_n = \frac{1}{n} \tan^{-1} \left(\frac{\sum_{k=1}^{N} w_k \sin(n\phi_k)}{\sum_{k=1}^{N} w_k \cos(n\phi_k)} \right) . \tag{2.1}$$

Here the weights w_k are the energies measured in each tower k. The calculation of the event planes is here performed in terms of towers, but just for an additional drop in efficiency would give equivalent results when carried out with reconstructed clusters corresponding to particles. This uses the angular anisotropies of particles observed in the detector to relate back to the event plane (e.g. for $n = 2$ the impact parameter plane).

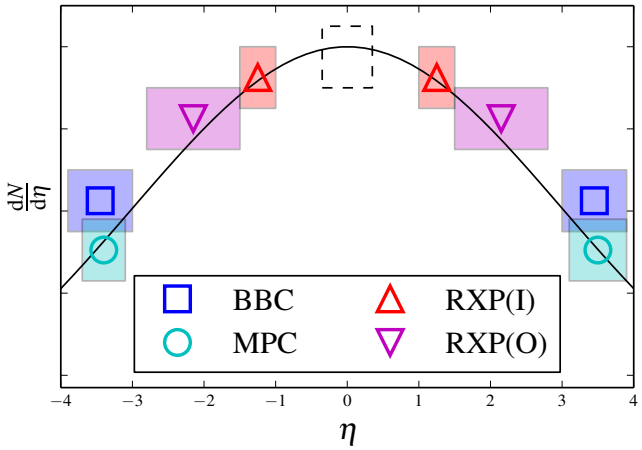

Figure 2.2: Schematic overview of the locations of global detectors. The horizontal axis shows the extent of each detectors in terms of its coverage in pseudorapidity η which is related to the polar angle θ by $\eta = -\ln\left[\tan\left(\frac{\theta}{2}\right)\right]$. The central arms measure in the pseudorapidity range indicated by the dashed box. The black line gives a schematic overview of the pseudorapidity distribution of charged particles emitted in an Au+Au collision.

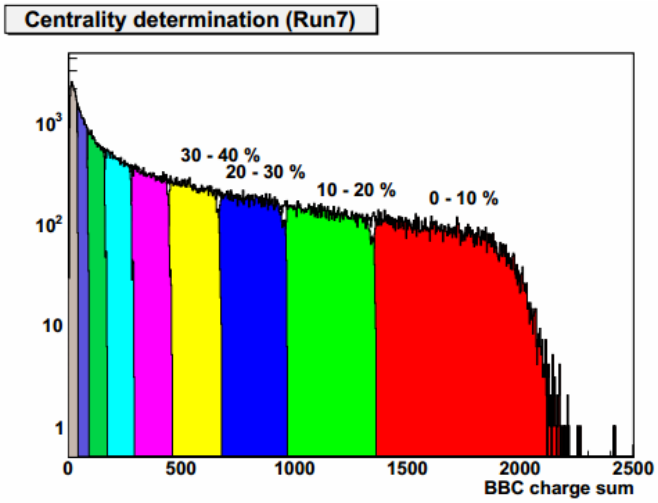

Figure 2.3: Determination of centrality from the BBC charge sum [39], here showing an example for 2007 Au+Au data. Events are classified by the amount of charge collected in the BBC with each centrality class containing an equal fraction of the recorded events.

The quality of the event plane determination depends on the number N of particles used like $\sqrt{N}$ so that the small particle multiplicity at very forward pseudorapidities limits the event plane resolution in the MPC. Since anisotropies of particles are used to quantify the event plane, the resolution is also directly proportional to the flow magnitude.

The Reaction Plane Detectors

The Reaction Plane Detectors (RXPs) [41] were designed specifically to address shortcomings in measuring the event planes in the MPC, specifically the limits on the resolution of event plane measurements imposed by very low multiplicity in forward directions. The RXPs were installed at less forward locations covering pseudorapidities $1.0 < |\eta| < 2.8$ and full azimuth. The detectors are located $\pm 39\,\text{cm}$ from the nominal interaction vertex along the beam axis. Each detector consist of 24 scintillators detecting traversing charged particles, and are arranged in two concentric circles around the beam axis, c.f. Fig. 2.4. The scintillators closer to the beam pipe are collectively referred to as the *inner* and the

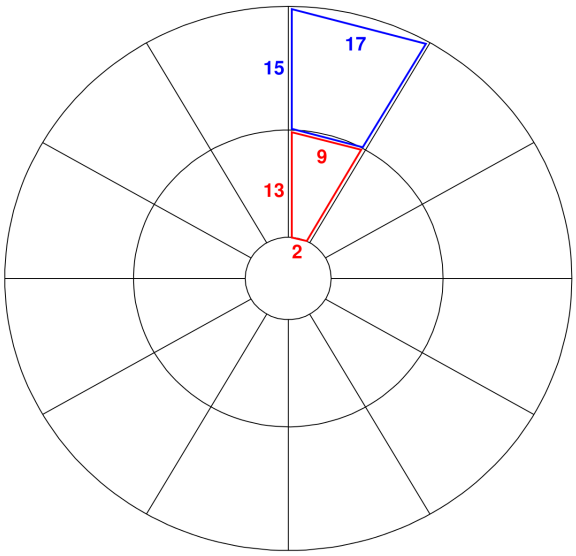

Figure 2.4: Schematic diagram of the reaction plane detectors, showing one detector [41]. The beam pipe goes through the hole in the center of the detector around which the scintillator paddles of the detector are arranged in concentric circles. The inner reaction plane detector is shown in red, the outer in blue. Numbers give dimensions of the scintillator in cm.

ones further as the *outer* RXP, and cover ranges in pseudorapidity $1.0 < |\eta| < 1.5$ and $1.5 < |\eta| < 2.8$, respectively. To additionally increase the charged particle multiplicity the collision-facing sides of the RXP detectors are covered with lead converters of 2 cm thickness which cause production of conversion electrons from otherwise undetected

photons. The event planes are measured with the same method as for the MPC, i.e. from raw hits in the detector and Eq. (2.1). Due to the substantially larger particle multiplicity in its rapidity range the resolution of the RXP is about a factor 2 better than that of the MPC, see Section 4.2.1.

2.2 Central arm detectors

The central arm contains the detectors to identify and measure charged particles and photons at midrapidity $|\eta| < 0.35$. Going outside in radius from the beam axis the detectors are the cylindrical Hadron-Blind Detector (HBD) used for electron identification followed by region of strong magnetic field which bends trajectories of charged particle. Detectors further out are split into two functionally similar arms with cover $\sim \pi/2$ in azimuth and are used to reconstruct trajectories of charged particle and photons. The so called *west arm* covers roughly the azimuthal range $-\frac{\pi}{4} < \phi < \frac{\pi}{4}$ while the *east arm* measures in $\frac{3\pi}{4} < \phi < \frac{5\pi}{4}$.

Magnet

The momenta of particles produced in heavy-ion or elementary particle collisions are typically measured via the curvature of their trajectories in a strong magnetic field where the Lorentz force exerted by the magnetic field forces charged particles to move on curved trajectories. For homogeneous fields particles would move on circular trajectories with the radius directly proportional to the particle momentum.

In PHENIX a strong axial magnetic field [38] is used to bend trajectories of particles emitted at midrapidity in the transverse plane. The field is supplied by two sets of inner and outer coils located outside of the central region along the beam axis. Flux is returned with a return yolk located outside of the detector at $R > 3\,\mathrm{m}$. The inner and outer coil can be operated so that their fields add ("++" configuration) or so that they partially cancel ("+−" configuration). For the 2010 run the HBD detector which cannot be operated in strong fields was installed around the beam pipe, so the magnet was operated in the $+-$ configuration with a minimal field out to a radius of $R = 50\,\mathrm{cm}$. At a radius of $R \approx 1\,\mathrm{m}$ the field reaches its maximal value of approximately 3.5 kG and then decrease until in becomes very small at $R = 2.5\,\mathrm{m}$, supplying a total field integral of approximately 0.78 Tm.

The Hadron-Blind Detector

The Hadron-Blind Detector (HBD) [42] is a Cherenkov detector installed around the beam pipe. The detector consists of a cylindrical volume of radius $R = 50\,\mathrm{cm}$ filled with

CF_4 gas acting as the radiator, followed by a series of gas electron multipliers (GEMs) amplifying the photon signal which is then measured in CsI photocathodes evaporated onto the detector surface and passed along for processing by readout electronics of radiation length $X/X_0 = 2$ to 3% at a radius $R \approx 60\,\text{cm}$. In this analysis we use the HBD solely as a spatially well-defined source of photon conversions in its readout electronics and their mounts.

The primary design goal of the HBD was to identify photon conversion pairs $\gamma \rightarrow e^+e^-$ originating in the beam pipe and electron pairs from π^0 Dalitz decays $\pi^0 \rightarrow e^+e^-$ which are the main source of background in dielectron measurements. Since the inside of the HBD is practically field-free these pairs would be observed in the HBD with minimal opening angle, i.e. lead to HBD clusters containing double the signal seen for single electrons.

The tracking detectors

The Drift Chamber (DC) and Pad Chamber (PC) [both described in 33] are the primary detectors used to reconstruct trajectories of charged particles in PHENIX. In this section we first introduce the detectors and then discuss how trajectories of charged particles are reconstructed.

The Drift Chambers

The Drift Chambers (DCs) consists of two identical detectors located in the east and west half of the central arm. Trajectories are measured by collection ionization charge when a charged particle traverses the gas in the DC which consists of equal amounts of argon and ethane and 1% of C_2H_5OH. The drift chambers are operated at radii $2.0\,\text{m} < R < 2.4\,\text{m}$ where the residual magnetic field is less than $0.6\,\text{kG}$ and extend $\pm 180\,\text{cm}$ in the z-direction. Each detector is segmented into north and south halves consisting of 20 equal sectors covering $4.5°$ in ϕ each where combinations of adjecent sectors in the north and south are read out by the same electronics and are referred to as *board*. In each sector multiple layers of wires at constant azimuth ϕ are used to create and shape an electric field causing drift of ionization to dedicated sense wires, see Fig. 2.5 for a schematic overview of a sector. The X1 and X2 wire layers run parallel to the beam axis and are used to measure trajectories in radius r and azimuth ϕ and are followed by the U and V layers running at angles $\pm 6°$ to the X wires which are used to constrain the positions of trajectories along the z-direction. With the used wire layout each wire has a spatial resolution $< 120\,\mu\text{m}$ in the $r - \phi$ plane.

The drift chambers use the charge of fast moving electrons from ionization as a signal. As a charged particle moves through the chamber it ionizes gas molecules creating both positively charged ions and electrons with negative charge. Due to their higher mobility electrons move much faster than the heavier ions and create an avalanche as they approach

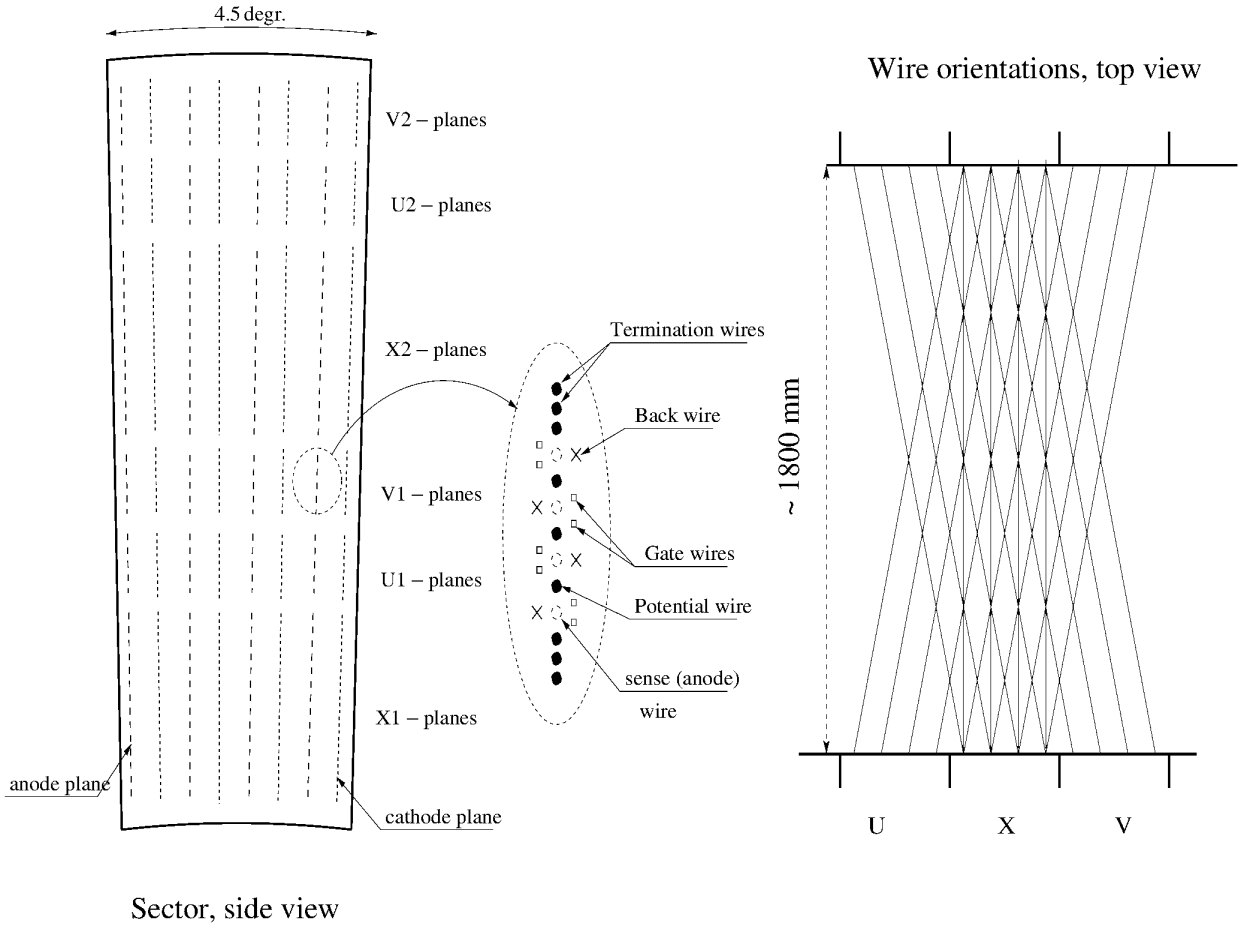

Figure 2.5: Schematic overview of a single drift chamber sector [33]. The left panel shows the positions of the different wire planes along the beam axis; the right panel the wire orientations when viewed from the top. In the middle positions of the different wire types are shown. Filled circles and open squares denote the position of wires used to create or shape the electric field, wires denoted by open circles are used to collect and measure the ionization.

the anode wire, thus leading to an amplification of the signal [43]. To properly integrate the charge from electrons (a short integration window of only 6 ns is used) an accurate determination of wire timing offsets and a calibration of the electron drift velocity are crucial. In PHENIX this calibration is performed automatically for each data collection run of roughly 50 min to account for changes in environmental conditions affecting the drift velocity, i.e. changes in pressure, temperature or the gas mixture. Here we measure an average arrival time of fast electrons and the maximal time needed by ions for each layer in every sector from which one can calculate both specific drift velocities and zero points of the time. After calibration the single wire efficiency reaches ∼90-95% and track finding efficiency is ∼99% in detector areas with all wires operational.

The Pad Chambers

The Pad Chambers (PCs) are multiwire proportional chambers arranged in three layers of increasing radius outside of the drift chambers. In this analysis only information from the first layer (PC1) is used which is positioned just outside the drift chamber. Each pad chamber contains one layer of anode wires sandwiched between two cathode planes and is filled with a gas mixture. As a charged particles moves through the gas it creates ionization which drifts to the anodes or cathodes. One cathode is finely segmented in z and ϕ direction and instrumented so that collected charged can be read out providing position measurements. We use hit information from the PC1 to constrain the quality of tracks reconstructed in the drift chamber.

Track reconstruction

To reconstruct the trajectories of charged particles primarily information from the drift chambers and the PC1 is used in a combinatorial Hough transform assuming that all tracks originate from the nominal interaction vertex as measured in the BBC. For all combinations of hits in the X1 and X2 layers of the drift chamber two angles α and ϕ as defined in Fig. 2.6 are calculated. A greedy algorithm then identifies clusters in the Hough space (α, ϕ) where clusters in Hough space correspond to track candidates. The track candidates are then spatially constrained further by associating with hits in the UV layers and in the PC1 around the direction of the track candidate. The *quality* of a track is given by whether it could be associated uniquely with hits in the UV layers and/or the PC1. To calculate the transverse momentum p_T and initial angle ϕ_0 before entering the magnetic field for a particle, a look-up table mapping α, and θ and ϕ at the reference radius to the initial direction and p_T is used; values between stored entries are interpolated with splines. The used look-up table was filled by a simulating transport of individual particles with $p_T > 170\,\mathrm{MeV}/c$ through the field for experimentally relevant emission angles ϕ_0 and θ.

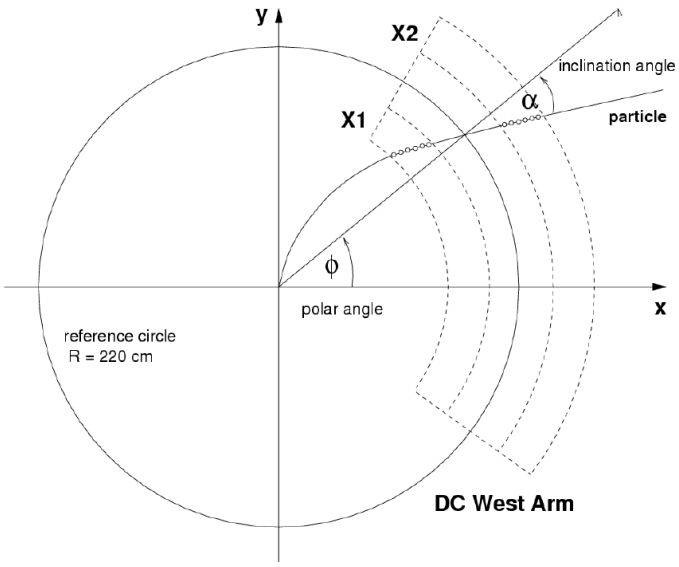

Figure 2.6: Definitions of angles used in tracking, [44]. Here the polar angle ϕ is the location of the intersection of line connecting hits in the X1 and X2 layers in the drift chamber and a cylinder with a reference radius $R = 2.2\,\mathrm{m}$. The angle α is the relative orientation of the hit line to the ϕ direction in the transverse plane.

The Ring-Imaging Cherenkov Detectors

The Ring-Imaging Cherenkov Detectors (RICHs) [34] are one of two primary detector systems used for electron identification (the other being the electromagnetic calorimeters described in the next section). Each RICH is located in one central arm between the PC1 and PC2 and consists of large CO_2 volumes and two spherical mirrors focusing Cherenkov light onto photomultiplier readout planes located on top of the PC1 in the north and south direction. The gas is chosen so that electrons emit Cherenkov radiation at all relevant momenta while the main background, charged pions, do only start to radiate until $p_T > 4.65\,\mathrm{GeV}/c$. An electron emits on average 12 photons with a ring diameter of about 11.8 cm. With reconstructed tracks pointed towards the RICH mirror surface as seeds a ring search algorithm can then identify hits likely to be associated with the electron track. The search algorithm is specifically tuned to search for rings caused by electrons. The quality of the information found in the RICH is quantified as the number of hit photomultipliers in rings of different sizes; we use n_0 which is the number of hit photomultipliers in a ring with $3.4\,\mathrm{cm} < R < 8.4\,\mathrm{cm}$ where the individual photomultipliers have dimensions on the order of 2.5 cm.

The Electromagnetic Calorimeters

The Electromagnetic Calorimeters (EMCals) [35] are designed specifically to measure photons, and to provide electron identification together with the RICH. PHENIX operates two types of calorimeters to be able to study systematic effects, the lead-scintilator calorimeter (PbSc) and the lead-glass calorimeter (PbGl). While the PbSc excels with a good time resolution, the PbGl has the better energy resolution,

$$\frac{\sigma_{\mathrm{PbSc}}(E)}{E} = 8.1\%\sqrt{E\,[\mathrm{GeV}]} \oplus 2.1\% \tag{2.2}$$

$$\frac{\sigma_{\mathrm{PbGl}}(E)}{E} = \frac{(5.9 \pm 0.1)\%}{\sqrt{E\,[\mathrm{GeV}]}} \oplus [0.8 \pm 0.1]\% \tag{2.3}$$

$$\delta(t)_{\mathrm{PbSc}} = 120\,\mathrm{ps}\ (\text{electrons and protons}),\ 270\,\mathrm{ps}\ (\text{pions}) \tag{2.4}$$

$$\delta(t)_{\mathrm{PbGl}} \gtrsim 200\,\mathrm{ps} \tag{2.5}$$

The PbGl is a Cherenkov detector and constitutes of two sectors of 9,216 individual towers installed in the lower east central arm. Each tower is $40\,\mathrm{mm} \times 40\,\mathrm{mm} \times 400\,\mathrm{mm}$ in size. The PbSc is a shashlik-type sampling calorimeter with six sectors installed consisting of 15,552 individual towers, four sectors in the west arm and two above the PbGl in the east arm. The size of a PbSc tower is $5.25\,\mathrm{cm} \times 5.25\,\mathrm{cm} \times 37\,\mathrm{cm}$.

The radiation thickness of both detectors is similar at about 18 radiation lengths. Electrons are separated from hadrons by measuring the ratio of their total momentum and the energy deposited in the calorimeter. While in an electromagnetic calorimeter electrons deposit most of their energy, i.e. $\frac{E}{p} \approx 1$, hadrons loose much less energy, especially at larger momenta, i.e. for them $\frac{E}{p} \ll 1$.

Part II

Data analysis

Chapter 3

The relative direct photon yield R_γ

The goal of this analysis is to measure the properties of direct photons as low in momentum as conventionally feasible with PHENIX, i.e. well into the region $p_T < 1\,\mathrm{GeV}/c$.

Measurements with electromagnetic calorimeters like the PHENIX EMCal are possible in that range, but become more and more polluted with misidentified hadrons, minimal-ionizing particles (MIPs), or even fake clusters, especially in high-multiplicity heavy-ion collisions. Ultimately, there will remain some irreducible background consisting to a large part of MIPs which needs to be understood very well to reach conclusions about the photons in the sample. This is the fundamental challenge to low p_T measurements in EMCals.

In order to avoid these complications this analysis follows another strategy. Here photons are not measured directly in the EMCal, but instead we reconstruct them indirectly through an electron-positron pair from a photon conversion. Electrons/positrons in PHENIX are primarily reconstructed from curved tracks in the PHENIX DCs, detectors which have a very different performance at low p_T:

- The lower the momentum of a track, the better its momentum can be reconstructed, i.e. typically the resolution increases towards lower p_T until it reaches a limit set by multiple scattering processes in the detector material.
- Fake tracks are orders of magnitude rarer in this momentum range than for a measurement in the EMCal.

By requiring good quality electron and positron tracks the amount of background is reduced further.

In general the experimental inclusive count of converted photons as a function of the converted photon momentum N_{ee}^{incl} measured with this method is a complicated quantity,

$$N_{ee}^{\mathrm{incl}}(p_{T\,ee}) = Y_\gamma a_{ee} \varepsilon_{ee} p_{\mathrm{conv}} \tag{3.1}$$

since its relation to the actual inclusive photon yield $Y_{\gamma}^{\text{incl}}(p_{T\gamma})$ is obscured by potentially complicated and possibly p_T-dependent dependencies on the geometrical acceptance of the conversion pair a_{ee}, the reconstruction efficiency of the pair ε_{ee}, which depends on both the efficiency with which each electron or positron was reconstructed as well as on the pair selection criteria, or the probability for a photon to actually undergo a conversion process p_{conv} which is directly related to the material budget. Most of these quantities (a_{ee}, ε_{ee}, but only extremely weakly p_{conv}) are functions of the photon p_T.

If we simultaneously measure the yield of converted photons from π^0 decays as a function of converted photon p_T

$$N_{ee}^{\pi^0}(p_{Tee}) = Y_{\gamma}^{\pi^0} a_{ee}\varepsilon_{ee} p_{\text{conv}} \langle \varepsilon f \rangle , \tag{3.2}$$

which is again a complicated function of the true photon yield from π^0 decays $Y_{\gamma}^{\pi^0}$, the conversion pair acceptance a_{ee} and reconstruction efficiency ε_{ee}, the conversion probability p_{conv} and a conditional acceptance $\langle \varepsilon f \rangle$ which quantifies the efficiency with which we successfully tag the conversion pair as coming from a π^0 decay given that we already have reconstructed the conversion pair, we get some handle on the ratio of the true yields,

$$\frac{N_{ee}^{\text{incl}}}{N_{ee}^{\pi^0}} = \frac{Y_{\gamma} a_{ee}\varepsilon_{ee} p_{\text{conv}}}{Y_{\gamma}^{\pi^0} a_{ee}\varepsilon_{ee} p_{\text{conv}} \langle \varepsilon f \rangle} = \frac{Y_{\gamma}}{Y_{\gamma}^{\pi^0} \langle \varepsilon f \rangle} \tag{3.3}$$

where the identically appearing and possibly p_T-dependent factors a_{ee}, ε_{ee} and p_{conv} cancel explicitly for each p_T and we get as a function of converted photon p_T

$$\frac{Y_{\gamma}^{\text{incl}}}{Y_{\gamma}^{\pi^0}} = \langle \varepsilon f \rangle \frac{N_{ee}}{N_{ee}^{\pi^0}} \tag{3.4}$$

where we only need to determine the p_T-dependent conditional acceptances $\langle \varepsilon f \rangle$ to go from the ratio of measured p_T-dependent converted photon yields N_{ee}^{incl} and $N_{ee}^{\pi^0}$ to ratio of the true photon yields Y_{γ}^{incl} and $Y_{\gamma}^{\pi^0}$ as functions of p_T.

To translate the already useful yield ratio from Eq. (3.4) to a quantity which is more straight-forward to interpret we will perform one more transformation. Given a model of hadronic sources producing photons in decays, i.e. a hadron decay cocktail, we can calculate our expectation for a cocktail ratio $Y_{\gamma}^{\text{hadrons}}/Y_{\gamma}^{\pi^0}$ where $Y_{\gamma}^{\text{hadrons}}$ is the yield of photons from hadron decays. Since the ratio in Eq. (3.4) is independent of detector effects we can calculate the p_T-dependent R_{γ}

$$R_{\gamma} = \frac{Y_{\gamma}^{\text{incl}}}{Y_{\gamma}^{\text{hadrons}}} = \frac{\frac{Y_{\gamma}^{\text{incl}}}{Y_{\gamma}^{\pi^0}}}{\frac{Y_{\gamma}^{\text{hadrons}}}{Y_{\gamma}^{\pi^0}}} = \frac{\langle \varepsilon f \rangle \frac{N_{ee}^{\text{incl}}}{N_{ee}^{\pi^0}}}{\frac{Y_{\gamma}^{\text{hadrons}}}{Y_{\gamma}^{\pi^0}}} \tag{3.5}$$

If we observe more photons than what is expected from hadron decays we will find $R_\gamma > 1$. In the following we will call any such excess photon yield *direct* photons. Given a cocktail of hadronic sources this unambiguously denotes a photon sample. The interpretation of the sources of these photons is experimentally less clear, and the name does not imply one exclusive source.

For an expected invariant yield of photons from hadron decays $Y_\gamma^{\text{hadrons}}$ we can also directly compute the invariant yield of direct photons

$$Y_\gamma^{\text{direct}} = (R_\gamma - 1) Y_\gamma^{\text{hadrons}} \tag{3.6}$$

In the following we will describe our event sample in Section 3.1, the inclusive converted photon sample N_{ee}^{incl} in Section 3.2 and the π^0-tagged photon sample in Section 3.3. The conditional acceptance $\langle \varepsilon f \rangle$ is described in Section 3.4 and the cocktail of hadronic photon sources in Section 3.5. Section 3.6 presents the results for R_γ.

3.1 Event selection

To ensure uniform detector acceptance we make use of an existing Run QA [45] which identified runs where all needed detectors were fully functional. The remaining useful runs were grouped into 5 groups with similar acceptance for electrons and positrons measured in the central arm.

To construct and recalibrate conversion pairs coming from the HBD backplane only events from a narrow z_{vertex} range can be used since only there the PHENIX magnetic field is uniform enough. We require

$$|z_{\text{vertex}}| < 10\,\text{cm} \tag{3.7}$$

With these selections we are left with a sample of 2.6×10^9 events out of 3.3×10^9 physics events recorded.

3.2 Inclusive photon sample

The inclusive photon sample is measured from conversions of real photons in a well-defined location in the detector material in the readout planes of the HBD detector.

PHENIX reconstructs tracks of charged particles outside of the magnetic field by correlating hits in the DC and PC. Since the magnetic field is parallel with the beam axis tracks are bent in the plane transverse to the beam. Tracks are then characterized by

ϕ_{DC}**:** the azimuth of the track at a reference radius of $R = 220\,\text{cm}$

z_{DC}**:** the z-location of the track along the beam axis at the reference radius

α: the difference between the direction of the track at the reference radius and the radial direction

z_{vertex}: the location of the event vertex along the beam axis

Since tracks are only bent in the transverse plane and mostly before they enter the tracking detectors knowledge of the starting point of tracks and their location and orientation after the field contains enough information to calculate their 3-momenta. In the PHENIX tracking procedure a starting point along the beam axis is assumed for fitting track momenta to the measured DC and PC hits, i.e. $R = 0$. This faithfully reconstructs tracks originating from the nominal event vertex. If however a track originates from an off-vertex location, i.e. from $R \neq 0$, this extrapolation to the vertex leads to an overestimate of the field integral experienced by the particles and causes the momentum to be overestimated by the reconstruction. For off-vertex photon conversion pairs which have practically no mass and are produced with zero opening angle the assumption of production at the nominal vertex leads to an artificially enlarged opening angle at the vertex so that they acquire fake mass. Since the magnetic field seen is roughly homogeneous in ϕ for all tracks considered in this analysis and the momentum reconstruction of off-vertex tracks is a direct function of the field integral wrongly attributed to them the fake mass of off-vertex conversion pairs is directly proportional to their radius of production.

In this analysis we use a second, alternative track model [39]. In this model tracks are not assumed to originate from the nominal event vertex, but instead from $R = 60\,\text{cm}$ which correspond to locations behind the radiation volume of the HBD, i.e. in the HBD backplanes, i.e. readout boards and electronics, which have a radiation thickness of $X/X_0 \approx 2$ to 3% [39, 42]. With the magnetic field roughly homogeneous in ϕ for all tracks in this analysis the alternative track model can be implemented as a parameterization of the track variables reconstructed under assumption of production at the nominal event vertex for a sample of tracks originating from the HBD backplanes. This parameterization can then be used to calculate a second, alternative set of track variables. The parameterizations we use are

$$\phi_{\text{ATM}} = \phi_{\text{DC}} + 0.163\alpha^3 + 0.03171\alpha^2 + 0.7076\alpha - 9 \times 10^{-5} \tag{3.8}$$

$$\theta_{\text{ATM}} = \arccos\left(4.425 \times 10^{-3}(z_{\text{DC}} - z_{\text{vertex}}) - 5.15 \times 10^{-5}\right) \tag{3.9}$$

$$p_{T,\text{ATM}} = \left|\frac{m_p}{\alpha} + b_p\right| \tag{3.10}$$

with (3.11)

$$m_p = 2.72 \times 10^{-6}|z_{\text{vertex}}|^2 - 7.11 \times 10^{-6}|z_{\text{vertex}}| + 0.0679 \tag{3.12}$$

$$b_p = 9.422 \times 10^{-6}|z_{\text{vertex}}| + 4.2 \times 10^{-3} \tag{3.13}$$

These relations are valid for $p_{T,\text{ATM}}$ measured in units of GeV/c, the angles ϕ_{DC}, ϕ_{ATM}, θ_{ATM} and α in mrad, and coordinates z_{vertex} and z_{DC} in cm. Here ϕ_{DC}, α, z_{vertex} and z_{DC}

are the variables under assumption of production at the nominal vertex while $p_{T,\mathrm{ATM}}$, ϕ_{ATM} and θ_{ATM} are under the assumption of production at the HBD backplane. The alternative variables are already in the usual global spherical coordinates and can be used directly to calculate alternative track 3-momenta.

$$\vec{p}_{\mathrm{ATM}} = p_{T,\mathrm{ATM}} \begin{pmatrix} \cos\phi_{\mathrm{ATM}} \\ \sin\phi_{\mathrm{ATM}} \\ \cot\theta_{\mathrm{ATM}} \end{pmatrix} \tag{3.14}$$

3.2.1 Single track cuts

Summarizing, to select electrons and positrons the following standard PHENIX electron selection criteria for Au+Au running are used:

I. Momentum cut: $0.2\,\mathrm{GeV}/c < p_T < 20\,\mathrm{GeV}/c$

II. Track quality cut: quality $\in \{31, 51, 63\}$

III. Fiducial cut: DC deadmap

IV. RICH electron ID cuts: $n_0 \geq 3$, disp < 5.0, $\chi^2/\mathrm{npe} < 10$

V. calorimeter electron ID cuts: $E > 0.15\,\mathrm{GeV}$, $E/p > 0.5$

Cut I and II These cuts are made to ensure a good sample of well-reconstructed tracks is selected. In PHENIX tracking is performed for tracks with $p_T > 0.17\,\mathrm{GeV}/c$, and a limit at $p_T > 0.2\,\mathrm{GeV}/c$ is made to avoid edge effects. The upper limit $p_T < 20\,\mathrm{GeV}/c$ is traditionally imposed to remove obviously misreconstructed or fake tracks which typically produce tracks with extremely large p_T. With the available sample size here there are by several orders of magnitude not enough tracks for the imposed upper limit to remove any appreciable number of real tracks.

The quality variable is a bit pattern encoding the hits used to form the track in the DC and PC. The respective mappings are

63: track has hits in both X1 and X2 layers, and unique hits in both UV and PC1 were found

51: hits in both X1 and X2 layers, and unique hit in PC1 found

31: hits in both X1 and X2 layers, unique hit in UV, and a non-unique hit in PC1 found

Since only charged particles cause tracks, by requiring a track we have implicitly rejected neutral tracks.

Cut III To homogenize the efficiency of charged tracks over the DC we reject tracks from detector edges or, depending on the particular run group, badly performing parts of the DC, see also Section 3.1. The run group dependent cuts we use were developed for a dielectron analysis in the same data set [45]. These cuts are parametrized as a function of track α, z_{DC}, ϕ_{DC} and hit board in the DC. See Fig. 3.1 for example visualizations of the used deadmaps.

Cuts IV These cuts on variables from the RICH are made for electron identification. n_0 is the number of phototubes hit in a ring with $3.4\,\mathrm{cm} < r < 8.4\,\mathrm{cm}$ around the track projection to the RICH. The variable disp measures the distance between the track projection and the center of the ring reconstructed in the RICH. χ^2/npe quantifies the quality of the reconstructed ring: χ^2 is a "χ^2-like" variable measuring the match of the fired phototubes to a ring shape; npe is the number of phototubes used in the ring. The combination of the cut in n_0 and disp are the major selections associating a track with a RICH ring; the cut in χ^2/npe is very weak and gives only very little additional discriminating power.

Cuts V These criteria on the energy reconstructed in the EMCal provide additional rejection of hadrons passing the RICH cuts. Charged pions start to go over the radiation threshold in the RICH above $p_T \gtrsim 4\,\mathrm{GeV}/c$. An electron or positron typically deposits a large part or all of its energy in the EMCal. We impose a lower limit on the energy reconstructed in the EMCal E as a sane lower limit, and require at least half of the energy expected from the track to be recovered in the EMCal, $E > 0.5p$.

3.2.2 Pair cuts

After we have selected a good sample of electron and positron tracks we can create electron-positron pairs which are candidates for having come from a conversion. In the low mass region $m_{ee} < 100\,\mathrm{MeV}/c^2$ the electron-positron spectrum is composed of pairs from Dalitz decays $\pi^0 \to \gamma ee$ and from photon conversions $\gamma \to ee$. Wrong combinations, i.e. combinatorial background, is negligible [46].

For each pair the invariant mass can be calculated from the 4-momenta of the electron and positron,

$$m^2 = (E^+ + E^-)^2 - \sum_{i=x,y,z} (p_i^+ + p_i^-)^2 \tag{3.15}$$

where $E^\pm$ and $p_i^\pm$ are the energy and 3-momentum components of positrons/electrons, respectively. We have suppressed terms in the electron mass m_e in above relation since $m_e \ll |p|$ for electrons in the considered momentum range. We can calculate a second mass value m_{ATM} using recalibrated 4-momenta assuming production at the HBD backplane. When comparing the usual and recalibrated pair mass any conversion pairs from the

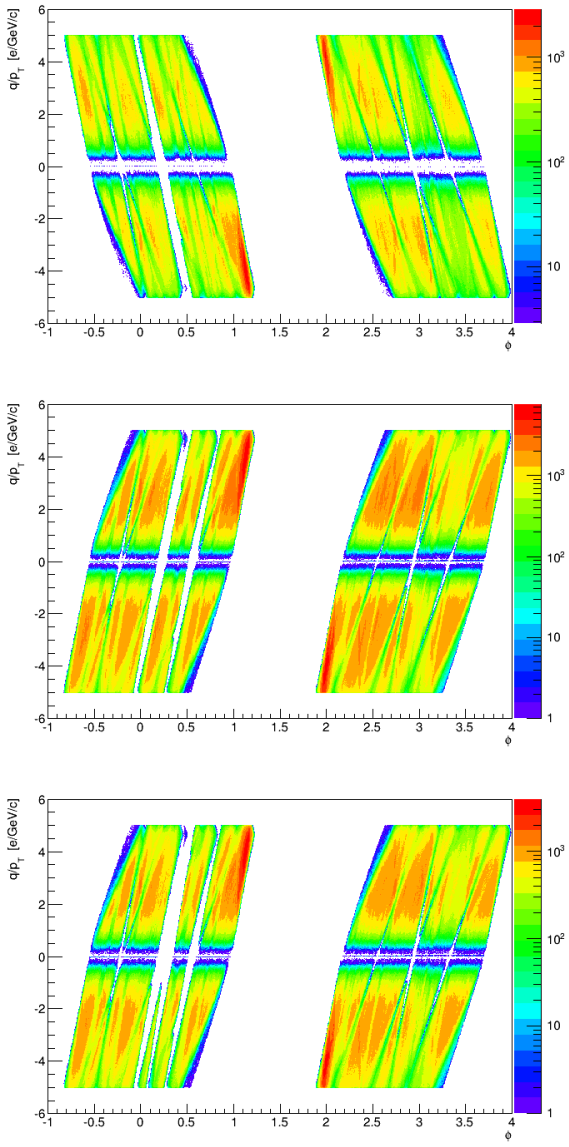

Figure 3.1: DC deadmaps for run groups 1, 3 and 4. Shown are histograms from tracks in data after applying the acceptance selections. The x-axes show the ϕ of the reconstructed track, the y-axes are the reconstructed q/p_T with q the charged assigned to the track. Run group 1 has a different field orientation than groups 3 and 4. The segmentation of the EMCal is visible from the 4 diagonal regions separated by a detector edges. The cuts imposed by the deadmap are visible as diagonal bands less steep than the edges between EMCal sectors.

off-vertex location will move to lower masses in the alternative model, while all other pairs will be less well reconstructed and be moved to larger masses, see Fig. 3.2.

To select conversion pairs we then impose the following selection criteria:

- electron and positron emitted into same arm
- $10\,\mathrm{MeV}/c^2 < m < 15\,\mathrm{MeV}/c^2$
- $m_{\mathrm{ATM}} < 4.5\,\mathrm{MeV}/c^2$
- $1 - P_{k=2}(\left(\frac{\Delta\phi}{\sigma_{\Delta\phi}}\right)^2 + \left(\frac{\Delta z}{\sigma_{\Delta z}}\right)^2) > 0.995$, with $\sigma_{\Delta z} = 4\,\mathrm{cm}$ and $\sigma_{\Delta\phi} = 10\,\mathrm{mrad}$

$10\,\mathrm{MeV}/c^2 < m < 15\,\mathrm{MeV}/c^2$, $m_{\mathrm{ATM}} < 4.5\,\mathrm{MeV}/c^2$ This cut selects conversion pairs produced away from the vertex at $R \approx 60\,\mathrm{cm}$. These pairs acquire a fake mass around $10 - 15\,\mathrm{MeV}/c^2$ and have very small invariant mass in the alternate track model. This cut leaves less than 1% pairs from π^0 Dalitz decays in the sample [39].

$1 - P_{k=2}(\left(\frac{\Delta\phi}{\sigma_\phi}\right)^2 + \left(\frac{\Delta z}{\sigma_z}\right)^2) > 0.995$ Δz and $\Delta\phi$ are the distances of the projections of the electron and positron tracks to the EMCal which are normalized to the resolution of in the projection. $P_{k=2}$ is the cumulative distribution for the χ^2 distribution for 2 degrees of freedom, so that $1 - P_{k=2}$ measures the probability for the two tracks to point to the same location given the actual Δz and $\Delta\phi$. The cut which is formulated as a cut in probability here corresponds to roughly a 10σ cut, and ensures that clusters in the EMCal are not used twice in a pair.

3.3 π^0-tagged photons

To measure the π^0 yield we pair the inclusive photons reconstructed from conversions with a second photon which we reconstruct in the PHENIX EMCal. Using a photon measured in the EMCal for the second photon is desirable since to identify a *likely* photon in the EMCal only very weak cuts are needed, which in turn keeps the efficiency to reconstruct the second photon large and the systematic uncertainties from these cuts small. The selections on the second photon will need to be accounted for when calculating the conditional acceptance efficiency $\langle \varepsilon f \rangle$. Since we cannot know if a pairing is genuine or just random and uncorrelated we will estimate the combinatorial background with a mixed event technique, so that impurities in the second photon sample can potentially only dilute the signal and reduce its significance, but not masquerade as a real measurement.

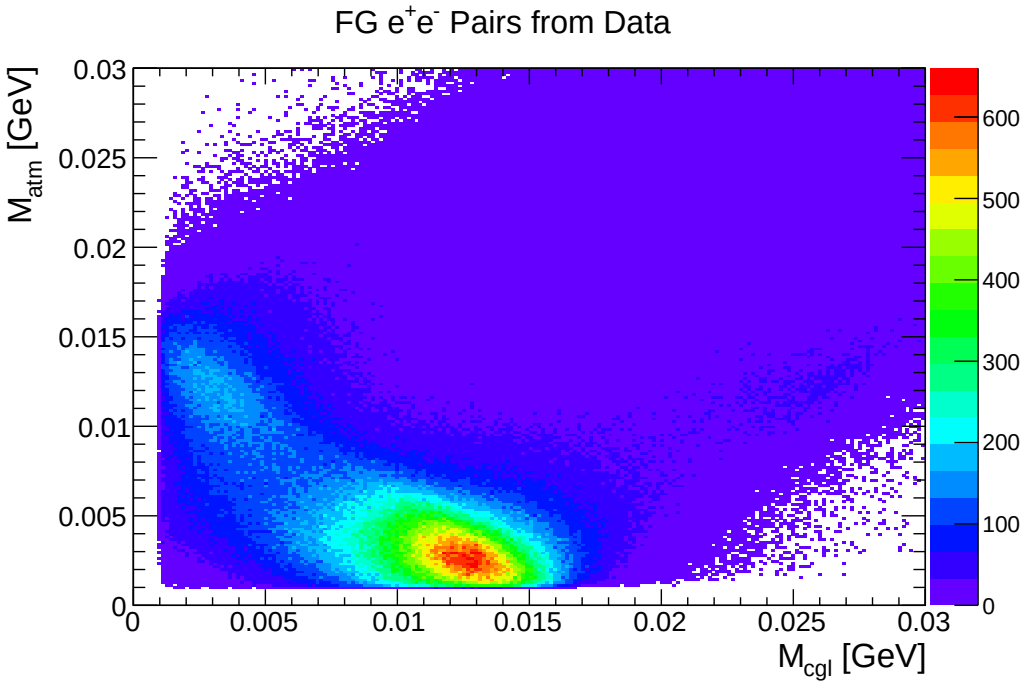

Figure 3.2: Pair mass reconstructed in reconstruction assuming production at the nominal event vertex M_{CGL} and in the HBD backplane M_{ATM} [39]. The blob around $(M_{\mathrm{CGL}}, M_{\mathrm{ATM}}) = (0.002, 0.012)\,\mathrm{GeV}/c^2$ corresponds to virtual photons pairs from π^0 Dalitz decays, $\pi^0 \to \gamma ee$; the blob around $(M_{\mathrm{CGL}}, M_{\mathrm{ATM}}) = (0.012, 0.02)\,\mathrm{GeV}/c^2$ corresponds to conversion pairs selected by our cuts.

EMCal Photon cuts

To minimize edge effects we reject clusters whose center lie on sector edges. In addition we also require that the 3x3 area around the cluster center does not contain randomly firing or inefficient towers. To determine which towers were hot/cold we recorded how often each tower was seen in any reconstructed EMCal clusters with $E > 900\,\mathrm{MeV}$. These count distributions were then fitted for each EMCal sector with Gaussian probability distributions. We then rejected towers which were more than 3σ away from the fitted mean. This analysis rejected 2907 out of $\sim$ 25,000 towers as hot/cold, some of which already lay on sector edges and would not have been used in the analysis anyway.

Since the EMCal photons are used only to confirm if a converted photon came from a π^0 decay we make additional cuts on them as loose as possible to gain efficiency. To ensure a reasonable shape of the cluster we require in the EMCal $\chi^2 < 3$. Here χ^2 is a "χ^2-like" variable which measures the distance of the seen cluster shape from a template for the same energy. The cut we use rejects some fraction of clusters with a strong mismatch between reconstructed energy and cluster shape, but has no strong effect on the EMCal photon efficiency.

Additionally, we require the clusters to have some minimal energy $p_T > 400\,\mathrm{MeV}/c$. This selection is motivated by statistics and a cut in the region $p_T = 400 \ldots 600\,\mathrm{MeV}/c$ optimizes the signal to background ratio in the π^0 yield extraction, see Fig. 3.3. Note that the clustering software already imposes some minimal energy requirement $E \gtrsim 120\,\mathrm{MeV}/c$ well below the choose cutoff. Since we already require each electron or positron in the conversion pair to have $p_T > 200\,\mathrm{MeV}/c$, i.e. $p_T > 400\,\mathrm{MeV}/c$ for the conversion pair, the additional momentum requirement on the EMCal photon puts strong kinematic restrictions on the observable yield from low p_T π^0; we will show in Section 3.6 that our results is stable under variations of this restriction.

To avoid combining electron-positron pairs with EMCal clusters produced by themselves we reject clusters which are too close to the projections to the EMCal of any conversion pair leg. We use an identical cut as used for the pair, $1 - P_{k=2}(\left(\frac{\Delta\phi}{\sigma_\phi}\right)^2 + \left(\frac{\Delta z}{\sigma_z}\right)^2) > 0.995$, but now measure the distance between the projection of an electron or positron track, and the EMCal cluster. See Page 34 for additional explanations of the different ingredients.

π^0 yield extraction

We now pair the converted photons with photons from the EMCal. To estimate the shape of purely random combinations we mix photons from different events with similar characteristics. Specifically, we mix events from the same 20% bin in centrality, with a reaction plane angle within $2\pi/5$, or with event vertex z within 2 cm. Pairings from the same event are the foreground, from different events the background sample. This yields

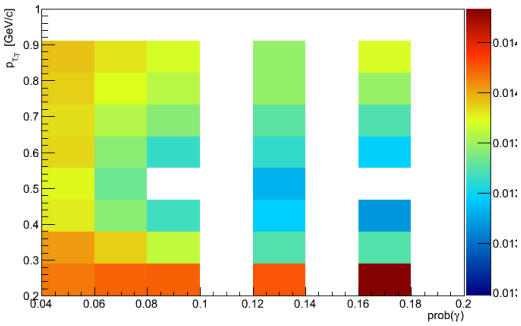

Figure 3.3: Relative statistical uncertainty on the measured π^0 yield for different calorimeter cuts. The used p_T cut on the calorimeter photon is varied along the y-axis. Variations along the x axis correspond to the probability of finding a cluster with a certain χ^2 containing n_{dof} clusters. The relative statistical uncertainty is shown color-coded for each set of cuts on the z-axis. White regions were not calculated. Independent of χ^2 we observe that cuts $0.4 < p_T < 0.6\,\text{GeV}/c$ minimize the relative statistical uncertainty.

2D-histograms in converted photon p_T and triplet mass $m_{ee\gamma}$.

To normalize and shape the mixed event background to the foreground we fit the foreground-background ratio away from the π^0 mass peak $0.10\,\text{GeV}/c^2 < m_{ee\gamma} < 0.18\,\text{GeV}/c^2$ to a normalization function given by a slowly varying 2nd order polynomial in $m_{ee\gamma}$. Since the normalization function can depend on the converted photon p_T the normalization needs to be determined for each slice of converted photon p_T separately; however, since we do not expect *strong* variations of the normalization function with p_T and our foreground sample has only limited size at large p_T we can describe the variation of the normalization function with p_T with another 2nd order polynomial, this time in converted photon p_T, so that instead of fitting many 1-dimensional functions we fit one 2-dimensional normalization function that ensure smooth variations under changing p_T,

$$n(p_T, m_{ee\gamma}) = N \times (a_0 + a_1 p_T + a_2 {p_T}^2) \times (b_0 + b_1 m_{ee\gamma} + b_2 m_{ee\gamma}^2) \tag{3.16}$$

We then scale the 2-dimensional background spectrum with n to obtain a scaled combinatorial background spectrum, see Figs. 3.4 to 3.7.

After subtracting the scaled background from the foreground distributions, we obtain the signal distributions show in Figs. 3.8 to 3.11. We then fit the π^0 peak region $0.10\,\text{GeV}/c^2 < m_{ee\gamma} < 0.22\,\text{GeV}/c^2$ in each slice in converted photon p_T with a Gaussian function and an additional 1st order polynomial to account for the normalization uncertainty or residual background. The extracted π^0 yield is then the integral of the Gaussian. To quantify the description of the combinatorial background with mixed event pairs we additionally use 0th and 2nd order polynomials as descriptions of the residual background, see Fig. 3.12. We find that the different assumptions for the residual

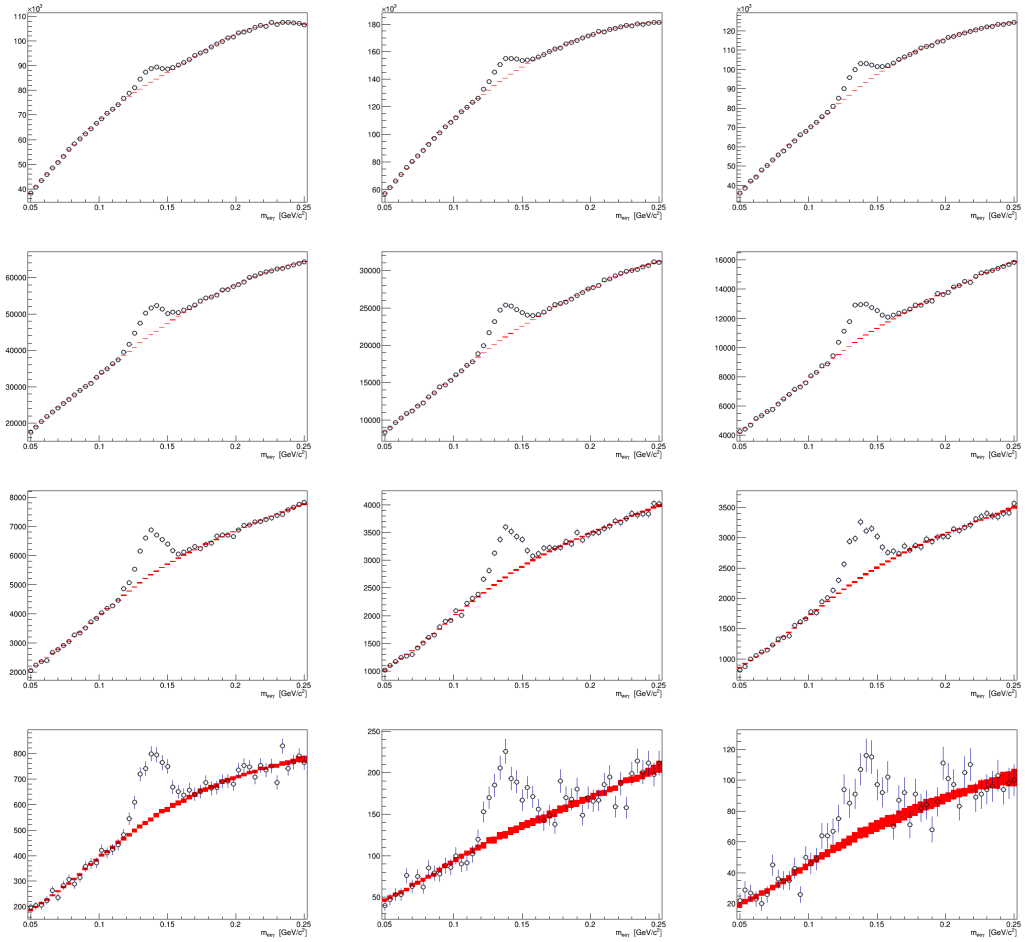

Figure 3.4: Foreground (black) and normalized background (red) for the 0-20% centrality bin in converted photon p_T bins of $0.4-0.6, 0.6-0.8, 0.8-1.0, 1.0-1.2, 1.4-1.6, 1.6-1.8, 1.8-2.0, 2.0-2.5, 2.5-3.0, 3.0-3.5, 3.5-5.0\,\mathrm{GeV}/c$. The uncertainty on the background includes both its statistical uncertainty and the uncertainty in the normalization with CL=0.66 which for Gaussian uncertainties corresponds to $\approx 1.26\sigma$.

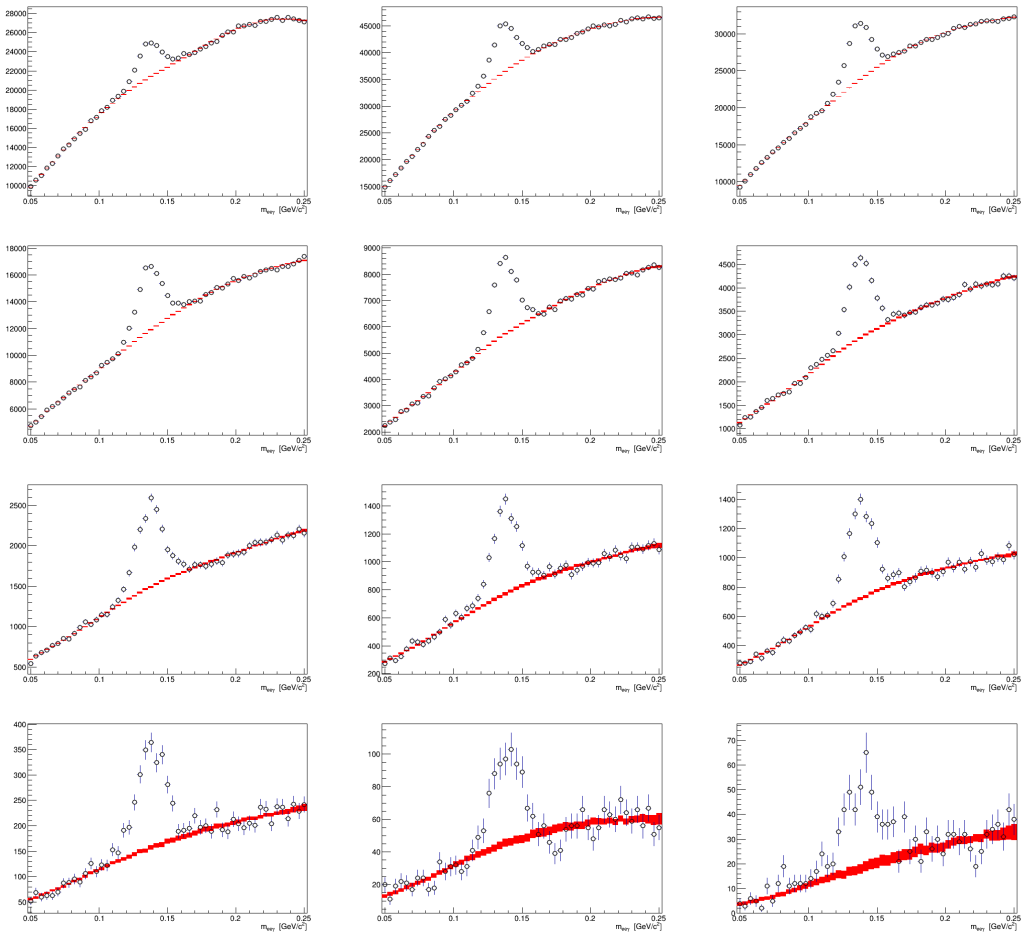

Figure 3.5: Like Fig. 3.4, but for the 20-40% centrality bin.

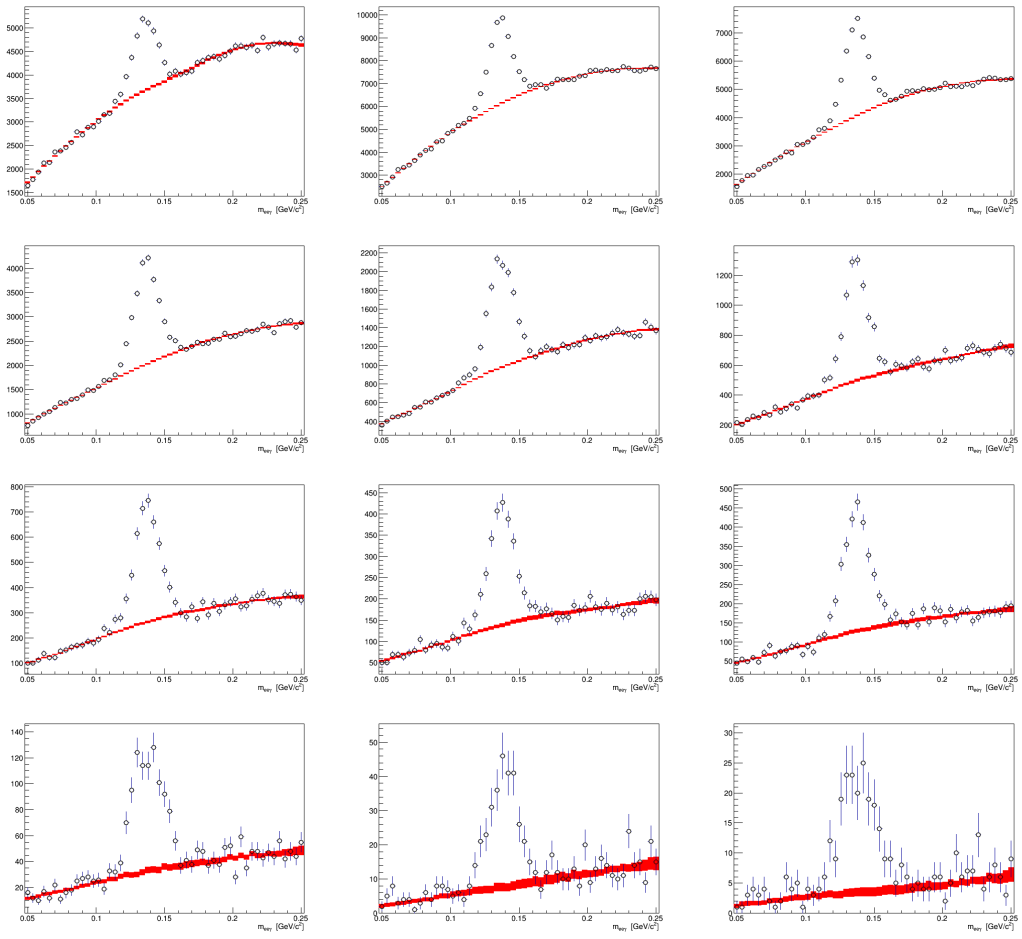

Figure 3.6: Like Fig. 3.4, but for the 40-60% centrality bin.

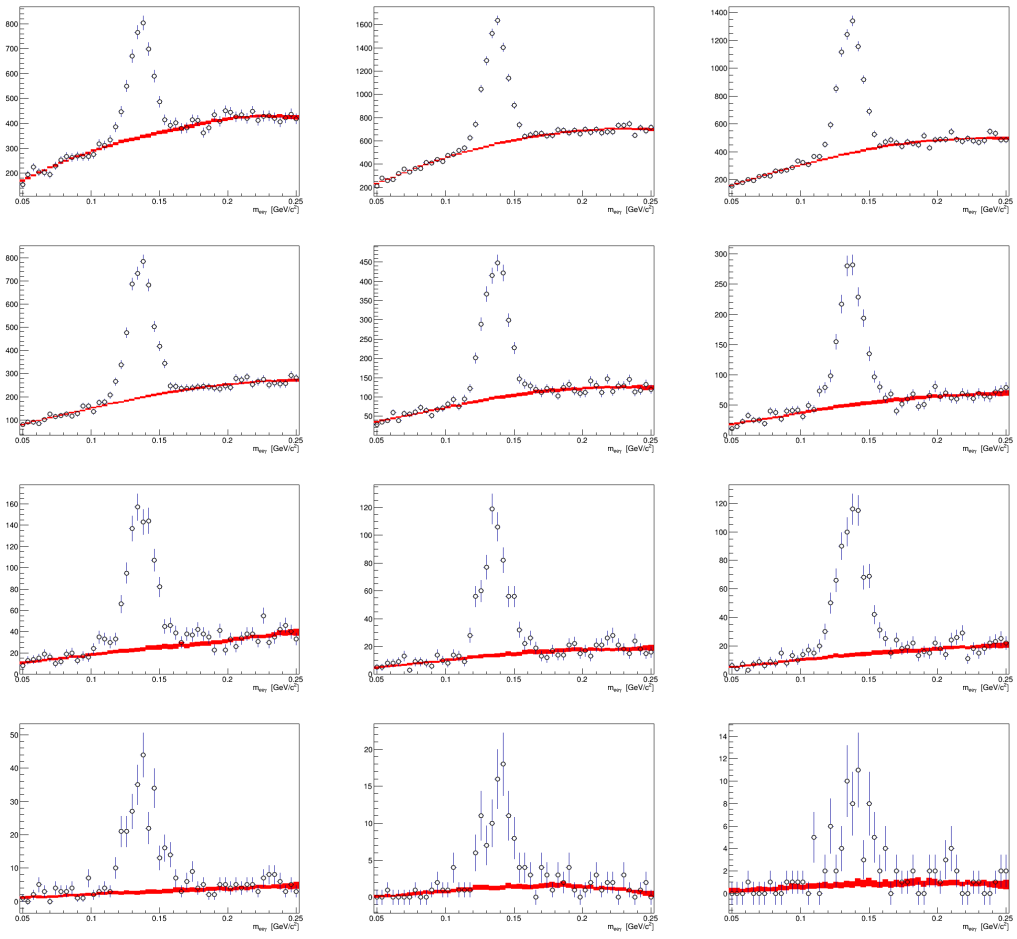

Figure 3.7: Like Fig. 3.4, but for the 60-92% centrality bin.

background fluctuate around our best value in a statistical way and assign an additional 4% statistical uncertainty in addition to the uncertainty from the fitted integral of the Gaussian, and add them both in quadrature.

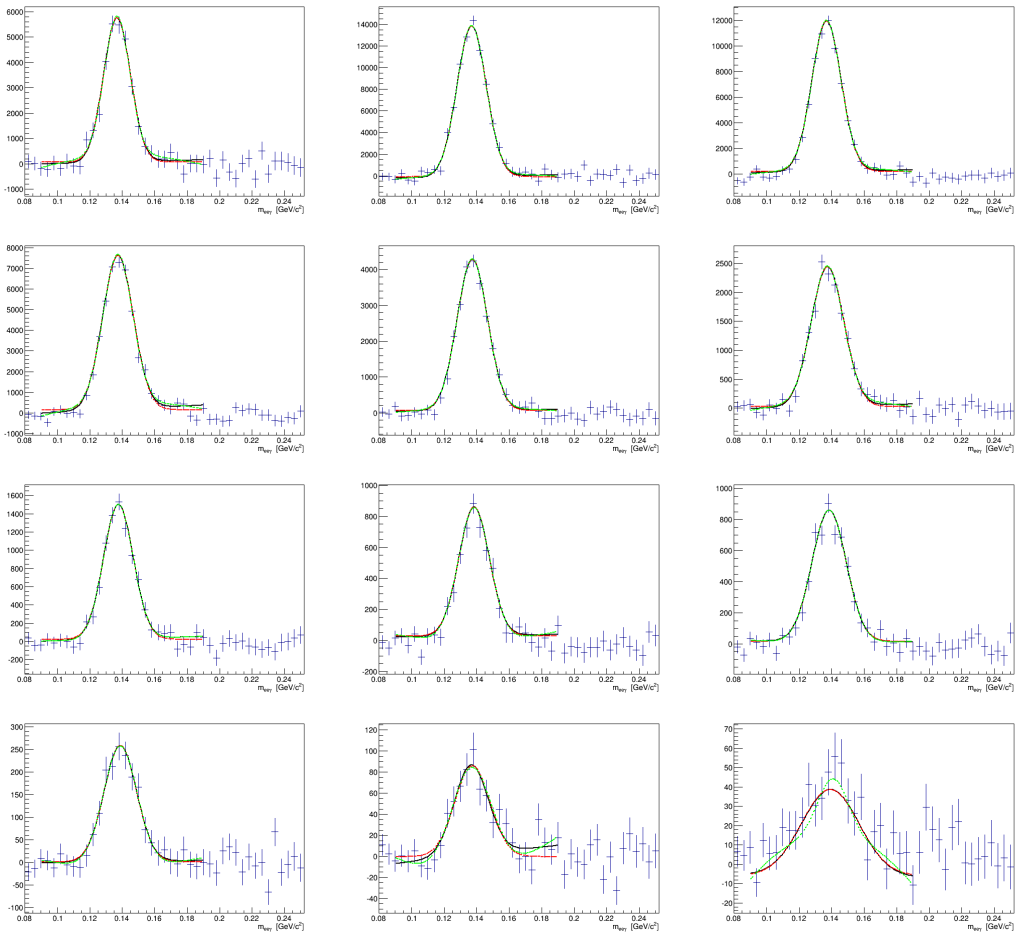

Figure 3.8: π^0 yield extraction in the 0-20% centrality bin in converted photon p_T bins of $0.4-0.6, 0.6-0.8, 0.8-1.0, 1.0-1.2, 1.4-1.6, 1.6-1.8, 1.8-2.0, 2.0-2.5, 2.5-3.0, 3.0-3.5, 3.5-5.0\,\mathrm{GeV}/c$. The different lines correspond to different assumptions about the residual background under the peak together with a Gaussian for the peak; here we use 0th, 1st and 2nd order polynomials in $m_{ee\gamma}$. For the best value a 0th order polynomial is used.

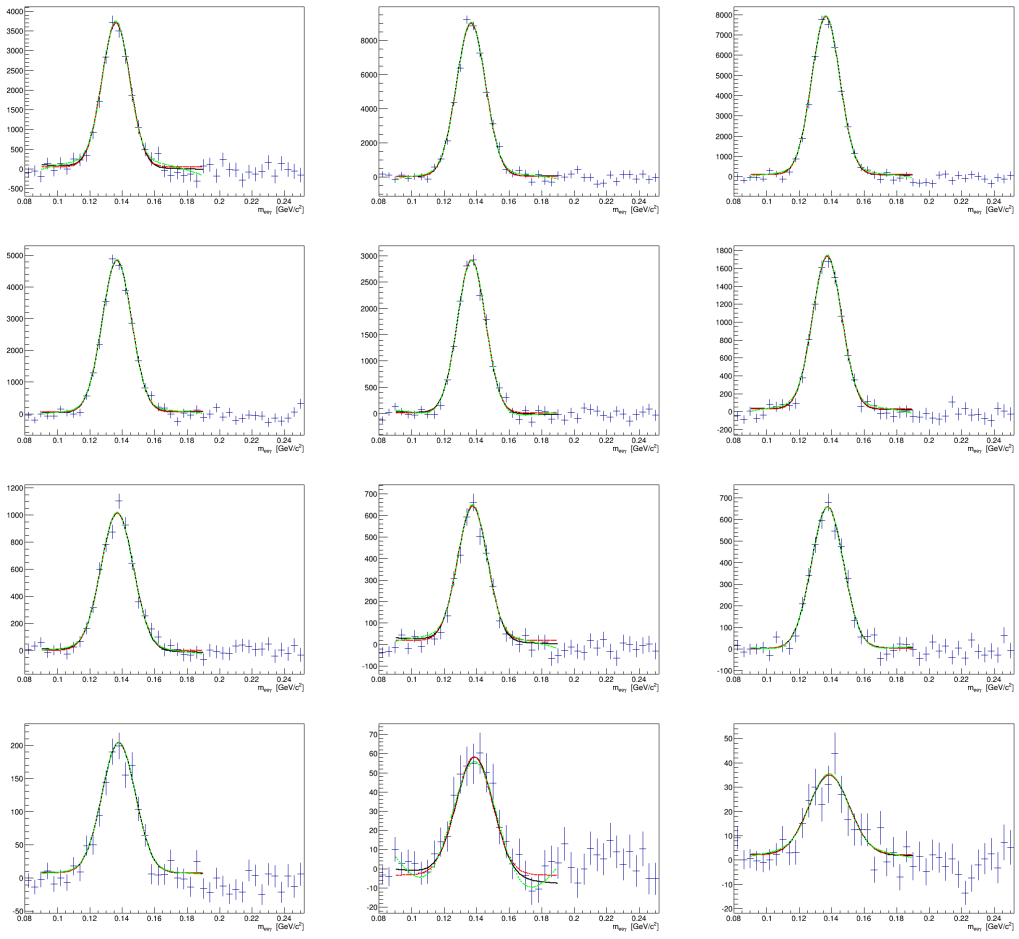

Figure 3.9: Like Fig. 3.8, but for the 20-40% centrality bin.

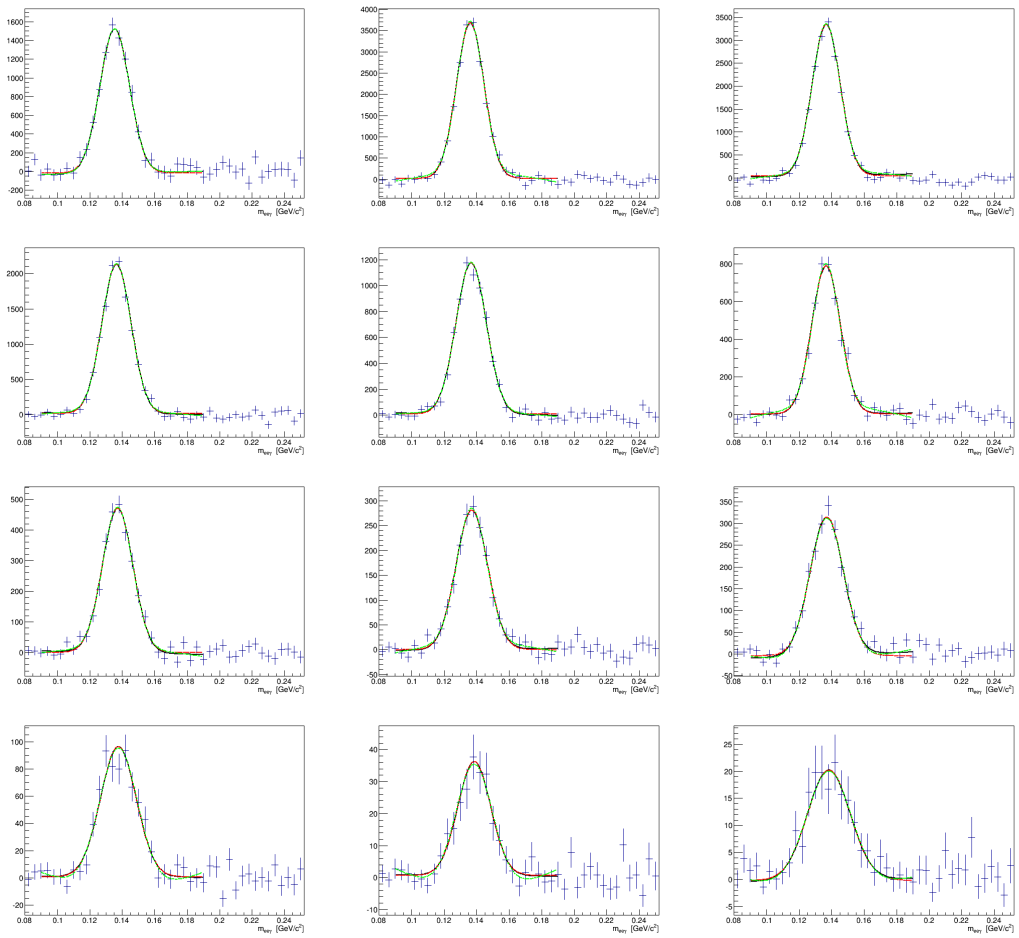

Figure 3.10: Like Fig. 3.8, but for the 40-60% centrality bin.

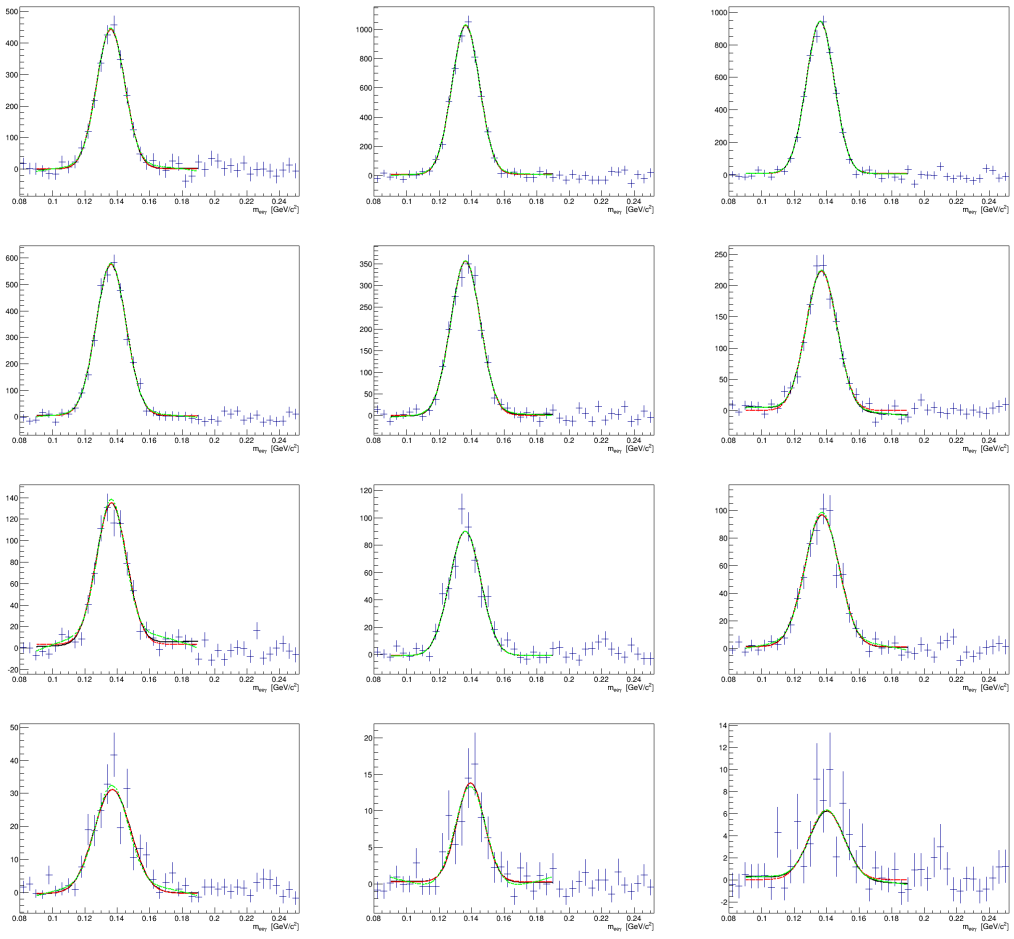

Figure 3.11: Like Fig. 3.8, but for the 60-92% centrality bin.

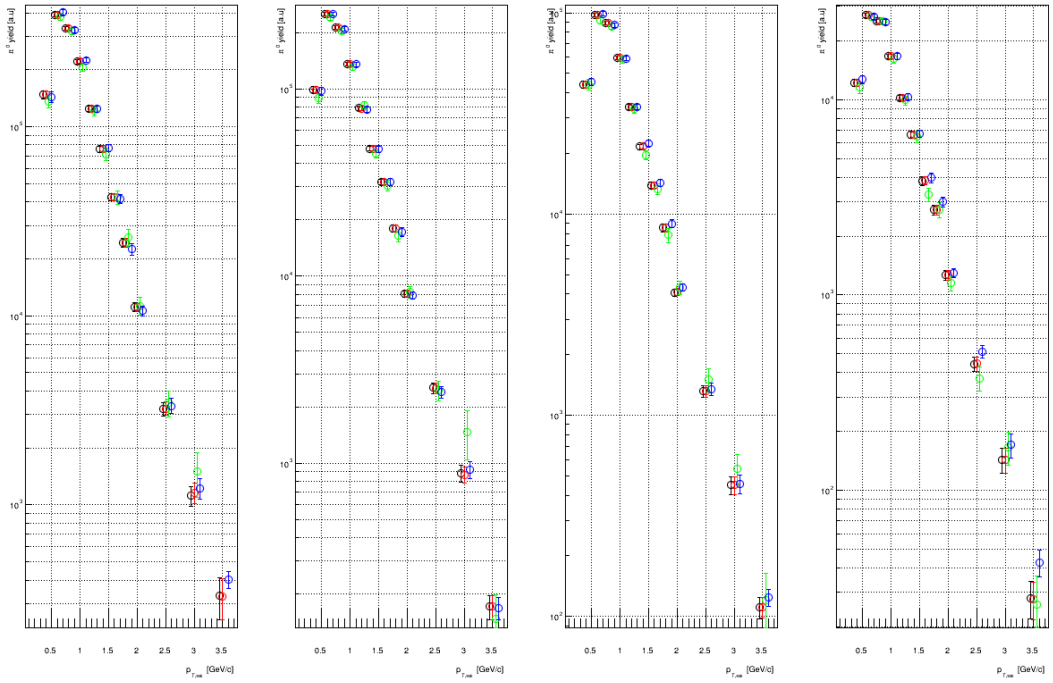

(a) Raw π^0 spectra extracted assuming a residual background described by a 1st order polynomial (black), a constant (red), a 2nd order polynomial (green) and from just counting the yield in the π^0 mass region assuming a flat background (blue).

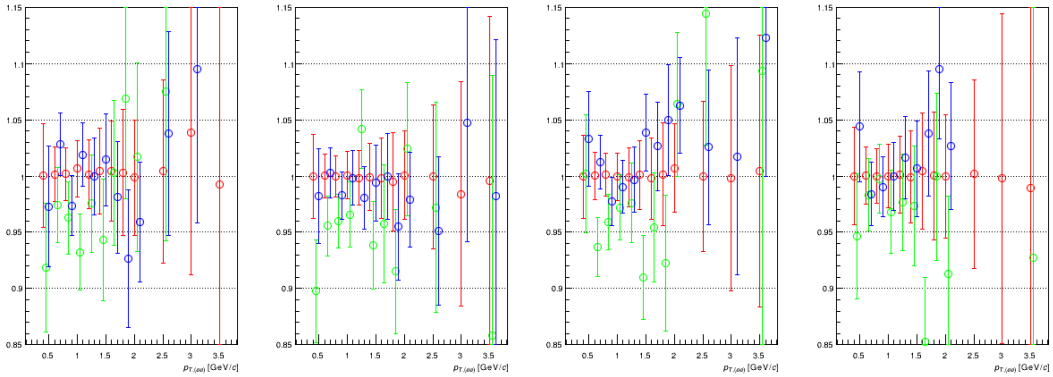

(b) Ratio of the raw π^0 yields extracted with different residual background assumptions to yields assuming a shaped described by a 1st order polynomial. Color coding like above.

Figure 3.12: Extracted π^0 yield with different assumptions for the residual background in centrality bins 0-20%, 20-40%, 40-60% and 60-92%.

3.4 The conditional acceptance $\langle \varepsilon f \rangle$

We have now extracted the raw counts for inclusive converted photons and for converted photons tagged as coming from π^0 decays. To translate the ratios of these raw counts to ratios of physical yields with Eq. (3.4) we need to determine the conditional acceptance $\langle \varepsilon f \rangle$ which quantifies the acceptance for the second photon in the EMCal from a π^0 decay given that we already reconstructed the first photon in a conversion pair. Since we require already having reconstructed the converted photon, $\langle \varepsilon f \rangle$ is a conditional acceptance and efficiency.

The main contributors to the behavior of the conditional acceptance $\langle \varepsilon f \rangle$ are in order of importance

1. kinematic constraints on the second photon
2. geometrical acceptance of the calorimeter
3. the reconstruction efficiency for the photon in the EMCal

where we only have a handle on the reconstruction efficiency which we keep large by applying only very weak cuts on the second photon. The kinematics are constrained by the momentum distribution of the parent π^0 and the decay kinematics. The geometrical acceptance depends on the azimuthal coverage of the EMCal which is roughly one unit in ϕ, the actual live area in the detector and indirectly through our separation requirement in the calorimeter the opening angle the photon pair from the π^0 decay.

3.4.1 Base converted photon sample

To calculate $\langle \varepsilon f \rangle$ we use a Monte Carlo simulation. We first generate π^0's from realistic, centrality-dependent momentum distributions and decay them into in a pair of photons using an exodus-based generator [47]. For the parent π^0 momentum spectra we use the centrality-dependent modified Hagedorn parametrizations described in Section 3.5. In exodus the decay $\pi^0 \to \gamma\gamma$ is modelled as a pure phase space decay with isotropic angular distribution, e.g. $E_{\gamma,1}$ flat in $0 \ldots E_{\pi^0}$ and $E_{\gamma,2} = E_{\pi^0} - E_{\gamma,1}$. We then convert one photon to an electron-positron pair with an equivalent angularly isotropic pure phase space decay which is a good approximation for a conversion process in our momentum range for photons [48]. We then determine if both conversion electron and positron would have been reconstructed. The efficiency turn-on and plateau of positrons and electrons is parametrized [46] as

$$\begin{aligned}
\varepsilon_{e^+} = &-4.00118\times10^{-2}/p_T - 4.31929\times10^{-3}/{p_T}^2 - 3.48514\times10^{-3}p_T \\
&- 6.62125\times10^{-1} + e^{4.17003\times10^{-1}+5.60212\times10^{-9}p_T} \\
\varepsilon_{e^-} = &-2.44424\times10^{-1}/p_T + 9.62876\times10^{-3}/{p_T}^2 - 2.59690\times10^{-2}p_T \\
&+ 9.90749\times10^{-1} + e^{-4.77995\times10^{-1}-2.00747p_T};
\end{aligned} \tag{3.17}$$

for electron or positron momenta $p_T > 0.2\,\mathrm{GeV}/c$ The central arm acceptance is modeled using the same run group-dependent dead maps we use for the analysis of real data, described in Section 3.2.1. These deadmaps were formulated in terms of α, z_{DC}, hit board, and ϕ_{DC}. To calculate the ϕ angle where a track crosses the DC at $R = 220\,\mathrm{cm}$ we use the standard PHENIX field lookup table also used in the track reconstruction. To match the experimental distribution of run groups we sample a random run group from the observed distribution of run groups. For a given field direction α can be calculated from the charge and the transverse momentum p_T

$$\alpha = \pm(3.28688 \times 10^{-5} + 0.0753907 \frac{q}{p_T}) \tag{3.18}$$

with the positive sign for run group 3 and the negative sign for all other run groups. The hit board is a simple function of ϕ_{DC} and we use the parametrization

$$\mathrm{board} = \frac{1}{0.01963496} \times \begin{cases} 3.72402 - \phi_{\mathrm{DC}} + 0.008047\cos(\phi_{\mathrm{DC}} + 0.87851) & \text{if } \phi_{\mathrm{DC}} > \frac{\pi}{2} \\ 0.573231 - \phi_{\mathrm{DC}} + 0.0046\cos(\phi_{\mathrm{DC}} + 0.05721) & \text{else} \end{cases} \tag{3.19}$$

Since a board in the drift chamber extend either in the positive or negative z-direction with no other features but a break at $z_{\mathrm{DC}} = 0$ it is sufficient to uniformly distribute tracks in both directions. We sample a random z_{DC} from a uniform generator with equal probabilities for the track hitting a board in the positive or negative z direction. The simulated acceptance maps are shown in Fig. 3.13.

Additionally we require the crossing location of the tracks in the EMCal to have at least one live tower in the 3x3 area around the crossing and to not lie in a tower on a EMCal sector edge. To determine the crossing location we use the same field lookup table to determine the location at the radius of the EMCal $R = 540\,\mathrm{cm}$. Towers are modelled as flat rectangles packed without gaps with proper dimensions and in their proper locations on the nominal front surfaces of the EMCal sectors.

Like in real data we require both the conversion electron and the positron to be emitted into the same arm. The effect of the separation cut on the track projections in the EMCal was studied, and we found no effect on genuine conversion pairs which open up in the magnetic field and end up well-separated in the EMCal.

3.4.2 Fast Monte Carlo for $\langle \varepsilon f \rangle$

For all potentially reconstructed conversion pairs we then check if the second photon would get reconstructed and pass cuts in the EMCal which we factorize into two components only,

- the probability f for the photon to hit an EMCal sector and a live set of towers,

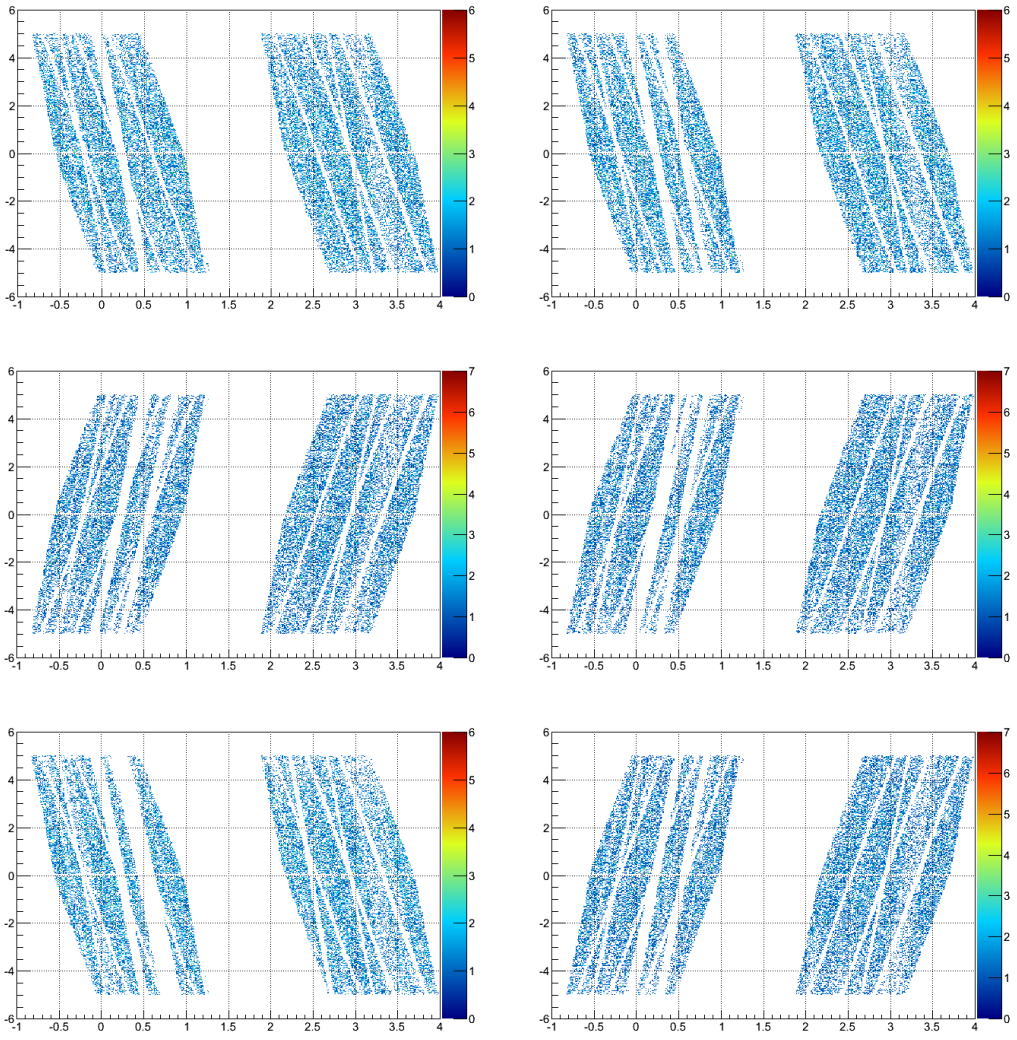

Figure 3.13: Simulated drift chamber deadmaps for electrons/positrons for different run groups with ϕ in mrad plotted on the horizontal and q/p_T in GeV/c on the vertical axes. The panel row-wise from top to bottom for run groups 1,2; 3,4; 5;6. For display-purposes no efficiency loss of tracks is simulated, i.e. $\varepsilon_{e^\pm} = 1$. This can be compared with Fig. 3.1.

- the probability to pass the cuts if the photon hit a live detector ε.

We measure centrality-dependent ε and energy resolutions in PHENIX's full Geant3-based detector simulation for single photon using a fully live detector, and then use these ε as inputs for a fast Monte Carlo simulation incorporating the decay kinematics and detector live areas. The final conditional acceptance $\langle \varepsilon f \rangle$ will be from an average over many possible parent π^0 contributing to the same converted photon p_T.

Single photon efficiency ε

To determine the centrality- and p_T-dependent efficiency of photons in a fully live EMCal, a full simulation with PHENIX's Geant3-based simulation framework PHENIX Integrated Simulation Application (PISA) is performed. To account for occupancy effects the simulated photons are embedded into real data.

We first generate photons uniformly in

- $-0.7 < \cos\theta < 0.7$,
- $0 < \phi < 2\pi$ and
- $1/30\,\mathrm{GeV}/c < 1/p_T < 1/0.15\mathrm{GeV}/c$.

The ranges chosen extend well beyond the acceptance limits in the real measurement to avoid edge artifacts. Photon momenta are thrown flat in $1/p_T$ to ensure a sufficiently large sample of photons at low p_T.

To account for effects from the underlying event on the photon reconstruction, the simulated detector response is merged with clusters reconstructed in real events with similar centrality from real data of 882 output files of the same Run10 data set used in the analysis. Clusters in the EMCal are reconstructed using the combined simulated and the real detector response. Since the real data is measured with a real detector with towers unusable for measurements, we use photons pointing to EMCal detector regions with fully live towers in the 3x3 area around the projection. We use the same tower deadmap also used in the analysis of real data described in Section 3.3.

A generated photon can contribute to a certain cluster in primarily one of two possible ways:

- a photon can directly deposit energy in one or multiple towers which make it into reconstructed clusters, or
- a photon can convert close enough to the EMCal or outside the magnetic field so that both the electron and the positron from the conversion point to the same cluster. In this case the reconstructed cluster will closely resemble the cluster the photon would have produced. If the electron and positron tracks from a conversion

are bent so much that each of them is reconstructed in mutually distinct cluster the energy in each cluster will be notably different from the original photon's energy. Roughly 5% of all photons will fall into this category.

To associate generated photons with reconstructed clusters, we choose a list of all clusters a photon directly contributed energy to and associate with the clusters with the biggest fraction of the photon deposited. If the photon converted before reaching the EMCal it will not directly contribute energy to any reconstructed cluster. In that case we find the cluster the conversion electron and positron contributed most of their energy to. If we identify the same cluster for the electron and the positron we associate it with the generated photon.

After applying the same cuts as in the real data analysis to the clusters reconstructed in the simulation, we end up with two sets of photons

- input photons pointing to fully live detector regions H_{in}
- photons reconstructed in clusters passing all cuts H_{out}.

Here H_{out} is a subset of H_{in}. For both sets we know the true, thrown photon momentum and can calculate their ratio as a function of the true momentum so that the input photon distribution used in the generator drops out.

$$\varepsilon(p_{T,\gamma}) = \frac{H_{\text{out}}(p_{T,\gamma})}{H_{\text{in}}(p_{T,\gamma})} \tag{3.20}$$

The centrality-dependence of ε is introduced by recording the centrality of the real event used in the embedding and performing the above analysis in each subclass. We determine ε in 10% centrality bins for the PbGl and PbSc detectors separately. The resulting single photon efficiencies are shown in Fig. 3.14.

Single photon energy resolution

We use the same full detector simulation described in the previous section to extract centrality-dependent energy resolution functions for photons. Like for the efficiency we only consider photons hitting a fully live 3x3 area in the calorimeter, just like is the case for real photon clusters passing our cuts.

For each generated photon with energy E, under original angles θ and ϕ we record the reconstructed energy $\hat{E}$, and angles $\hat{\theta}$ and $\hat{\phi}$. Assuming approximate factorization of

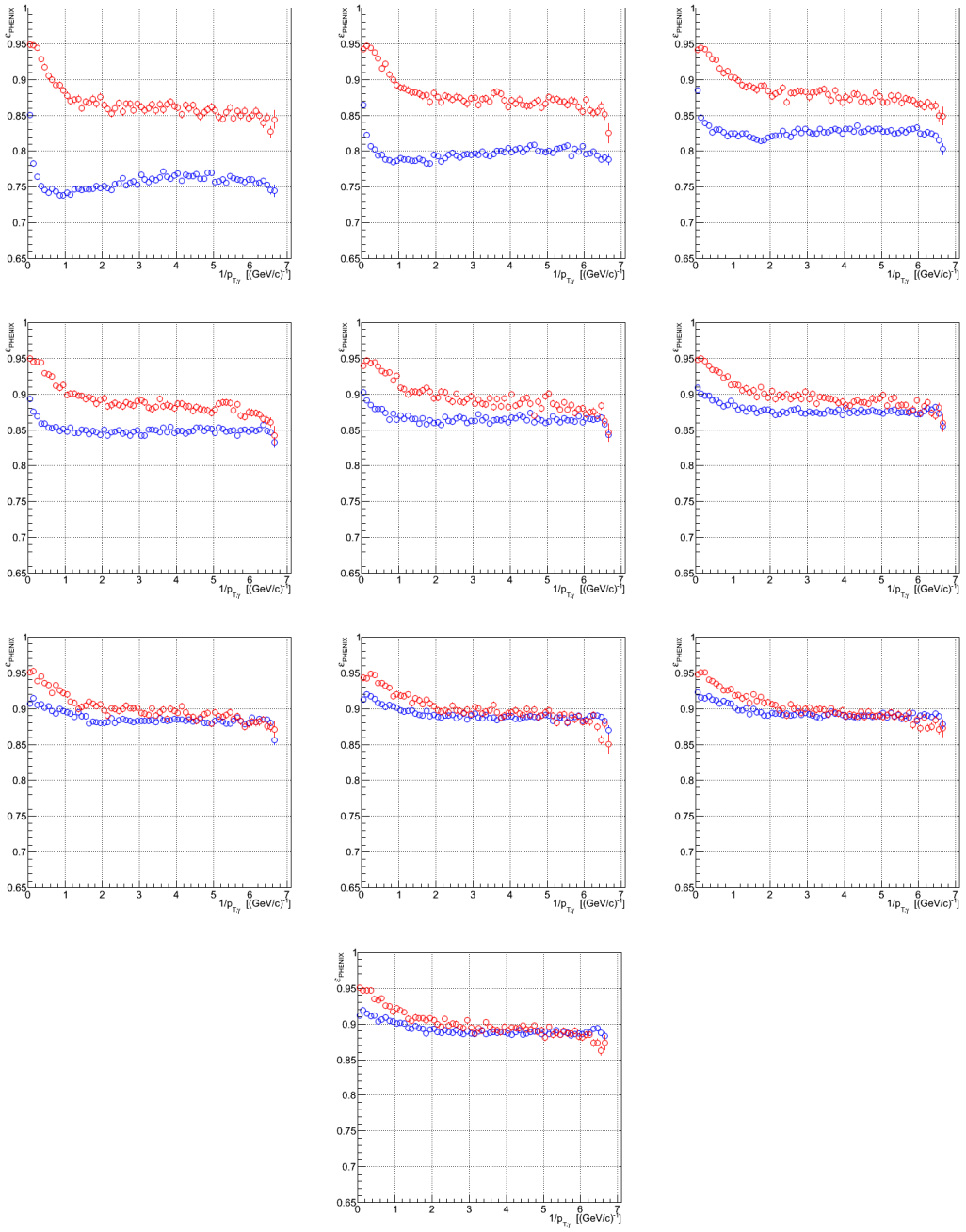

Figure 3.14: Single photon efficiency ε into the live detector as a function of one over the true momentum of the photon in 10% centrality classes for the PbGl (blue) and PbSc (red). Systematic uncertainties are not shown.

the resolution functions we can then histogram centrality-dependent functions

$$H_E\left(\frac{1}{E}\right) = \frac{E - \hat{E}}{E} \tag{3.21}$$

$$H_\theta\left(\frac{1}{E}\right) = \frac{\theta - \hat{\theta}}{\theta} \tag{3.22}$$

$$H_\phi\left(\frac{1}{E}\right) = \frac{\phi - \hat{\phi}}{\phi} \tag{3.23}$$

where we again store information as a function of the inverse of the true, generated energy E to ensure good resolution of eventual features at lower energies. We do not parametrize the histograms, but will use them as lookup tables in the later simulation for $\langle \varepsilon f \rangle$. We store E in the histograms in the range $142\,\text{GeV} < E$, the energy resolution $|\frac{E-\hat{E}}{E}| < 1$, and the angular resolutions $|\frac{\theta-\hat{\theta}}{\theta}| < 0.2$ and $|\frac{\phi-\hat{\phi}}{\phi}| < 0.02$. Values outside of these limits were extremely unlikely in the simulation and should not contribute in the final measurement. We perform this analysis for 10% centrality bins determined from the real event embedded into, again for the PbGl and PbSc calorimeter subdetectors separately.

Complete simulation for $\langle \varepsilon f \rangle$

At this point we have assembled all the pieces needed in for the calculation of $\langle \varepsilon f \rangle$. Summarizing, the fast Monte Carlo simulation will perform the following steps to determine $\langle \varepsilon f \rangle$ for each centrality class

- We generate a parent π^0 with a p_T from a realistic, centrality-dependent p_T distribution. The parametrization used is described in Section 3.5. We generate the parent in the momentum range $0 < p_T < 15\,\text{GeV}/c$, flat in rapidity $|y| < 1$ and isotropically in ϕ.
- All parent π^0 are decayed into photon pairs with angular distributions isotropic in the π^0 rest frame.
- One photon is converted into a electron-positron pair. For both leptons of the conversion we check if they hit a live, run group-dependent region in the DC and a 3x3 area in the EMCal with at least one live tower. Run groups are sampled from a distribution matching the real data. We also sample the electron and positron efficiency. If not both conversion electron and positron pass the acceptance checks and are efficient we discard this iteration and start again with a new parent π^0.
- We check if the second photon points to a fully live 3x3 area in the EMCal. Given the true, thrown momentum of the photon p_T we look up the centrality-dependent

efficiency $\varepsilon(p_T)$. With a uniformly distributed random number r we reject the photon as inefficient if $\varepsilon(p_T) < r$.

- After determining which EMCal subdetector the photon would hit, we look up the resolution functions using the true variables, e.g. for a true energy E we look up the distribution of $\frac{E-\hat{E}}{E}$ in a narrow slice around the true energy and then generate a random number r from the distribution. The smeared energy is then $\hat{E} = E(1-r)$. We follow an identical procedure for θ and ϕ and can after recalculating the photon 4-momentum check the simulated photon against our EMCal photon p_T cut.

- If the second photon points to a live detector area, has a randomly sampled efficiency larger than the efficiency required for photons of this p_T and passes our p_T cut we count the converted photon as tagged.

- The conditional acceptance $\langle \varepsilon f \rangle$ is then the ratio of accepted converted photons with a successfully reconstructed EMCal photon and the full sample of accepted converted photons. We record $\langle \varepsilon f \rangle$ as a function of the converted photon p_T.

The resulting conditional acceptances $\langle \varepsilon f \rangle$ are shown in Fig. 3.15.

3.5 Cocktail of hadronic photon sources

To translate the acceptance-corrected ratio of the inclusive photon yield and the yield of photons from π^0 decays from Eq. (3.4) to the ratio of the inclusive photon yield to the photon yield from hadron decays R_γ from Eq. (3.5), we need to determine the expected ratio of photons from hadrons and π^0, the cocktail ratio. Since the ratio in data is corrected for detector and acceptance effects with $\langle \varepsilon f \rangle$ we can calculate the cocktail ratio at midrapidity without having to take detector effects into account.

We take the production channels listed in Table 3.1 which directly produce at least on photon into account and do not include channels which produce photons only in decays of daughter particles, e.g. decays which produce just π^0, since production from these sources is already explicitly accounted for.

The parent particle momentum spectra are centrality-dependent parameterizations of real data with modified Hagedorn functions [46],

$$\frac{1}{2\pi p_T}\frac{\mathrm{d}^2 N}{\mathrm{d}y\,\mathrm{d}p_T} = \frac{c\,p_T}{\left(e^{-(a m_T{}' + b m_T{}'^2)} + \frac{m_T{}'}{p_0}\right)^n} \tag{3.24}$$

with $m_T{}' = \sqrt{m_T{}^2 - m_{\pi^0}^2}$ and the transverse mass $m_T = \sqrt{m^2 + p_T{}^2} = \sqrt{m^2 + p_x^2 + p_y^2}$. To determine the parameters a, b, c, p_0 and n for the π^0 p_T spectra centrality-dependent

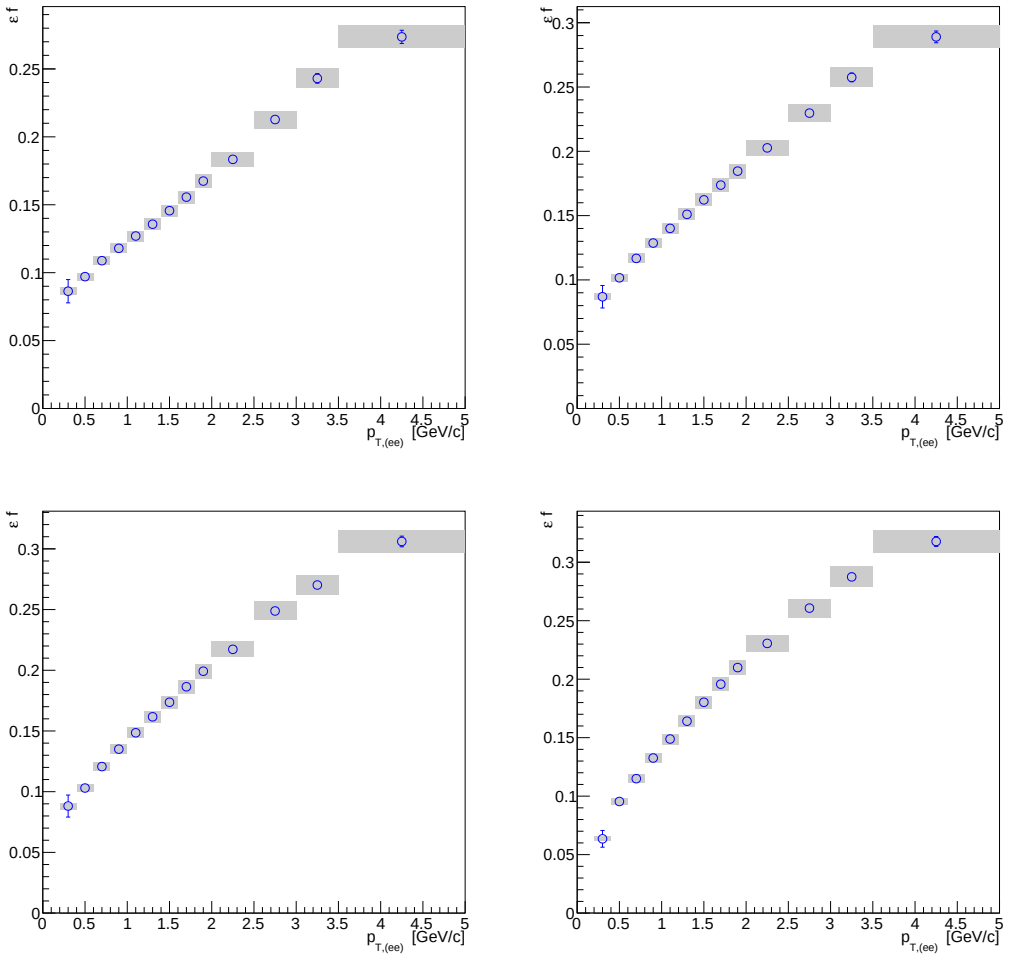

Figure 3.15: Conditional acceptance $\langle \varepsilon f \rangle$ in centrality bin 0-20%, 20-40%, 40-60% and 60-92%. The vertical extend of the gray boxes corresponds to the systematic uncertainty. The p_T binning corresponds to the binning for the final R_γ measurement.

Table 3.1: Photon production channels in the cocktail simulation.

parent particle	decay products	branching ratio
π^0	$\gamma\gamma$	98.8%
η	$\gamma\gamma$	39.3%
η	$\pi^+\pi^-\gamma$	4.6%
η'	$\gamma\gamma$	2.1%
η'	$\pi^+\pi^-\gamma$	23.0%
η'	$\omega\gamma$	2.8%
ω	$\pi^0\gamma$	8.3%

neutral and charged pion data was fitted [46] yielding the values shown in Table 3.2. There we also give the integrated π^0 yield into one unit in rapidity $\mathrm{d}N/\mathrm{d}y$.

While enough data is available for π^0 to directly fit the experimental spectra, this is not the case for the other mesons η, η' and ω. For these we use m_T scaling to give the shape while we can constrain the invariant yield from data. Specifically, while in Eq. (3.24) for π^0 parents ${m_T}' = p_T$ for other mesons we now use ${m_T}' = \sqrt{{m_T}^2 - m_{\pi^0}^2} = \sqrt{p_T + (m^2 - m_{\pi^0}^2)}$. Under the m_T-scaling assumption, spectra of different mesons have then the same shape and relative yields are determined from the flat, p_T-independent ratio of m_T spectra. In Fig. 3.16 we show experimental m_T spectra and a cross-check of the shape similarity. The next biggest contributor to the hadron decay cocktail after the π^0 are η mesons. To more carefully check the available data with the m_T scaling assumption at low p_T we fit the lowest n data points of the η to π^0 m_T spectra ratio with straight lines and extrapolate to $m_T = 0$, and find that the extrapolations are consistent with the ratio we use, see Fig. 3.17.

To ensure that the particular choice of parametrization and the m_T scaling assumption does not affect the final R_γ result we additionally check with parametrizations of the meson spectra with Tsallis functions [53]

$$E\frac{\mathrm{d}^3\sigma}{\mathrm{d}p^3} = \frac{1}{2\pi}\frac{\mathrm{d}\sigma}{\mathrm{d}y}\frac{(n-1)(n-2)}{(nT)^2}\left(1+\frac{m_T}{nT}\right)^{-n} \tag{3.25}$$

against the parametrization of the $p+p$ data with a modified Hagedorn function [46]. We find that the differences between the parametrizations are much smaller than other systematic uncertainties in the cocktail, notably the η/π^0 ratio, see Fig. 3.18 for the result.

The absolute yields are then calculated from the π^0 yield in the particular centrality bin, [46] and also in Table 3.2, and the ratios of the m_T spectra of the particular meson to

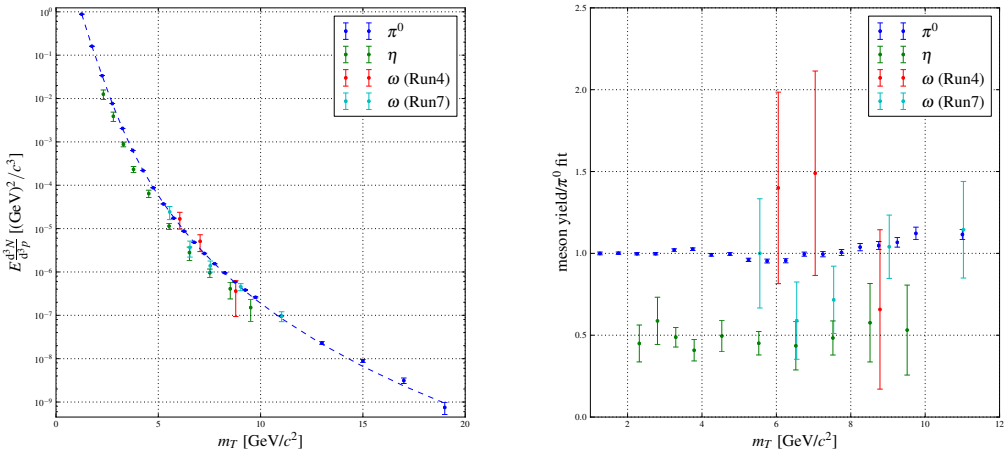

(a) Experimental m_T spectra for π^0 [49, 50], η [51], and ω [52] from minimum bias Au+Au data. The dashed line corresponds to a modified Hagedorn parametrization with Eq. (3.24).

(b) Cross checks of the m_T-scaling assumption. The experimental spectra are divided by the modified Hagedorn parametrization of the π^0 spectra. The experimental π^0 spectra were used for the fit. The ratios are flat in uncertainties – which are large for e.g. the ω.

Figure 3.16: Experimental m_T spectra.

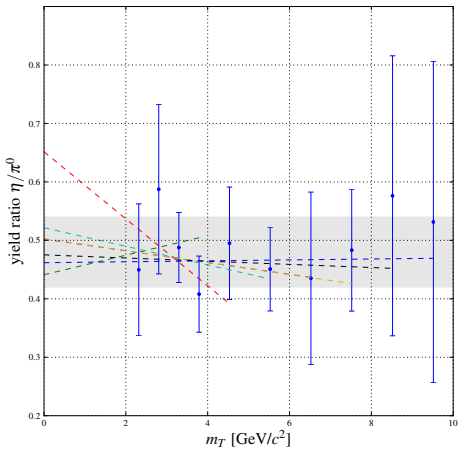

Figure 3.17: Check of the m_T-scaling assumption for the η. Shown is the ratio of the observed minimum bias Au+Au η m_T spectrum [51] and a parametrization of the minimum bias π^0 m_T spectra, cf. Fig. 3.16. The dashed lines are straight line fits to the first 3, 4, ...points, extrapolated to $m_T = 0$.

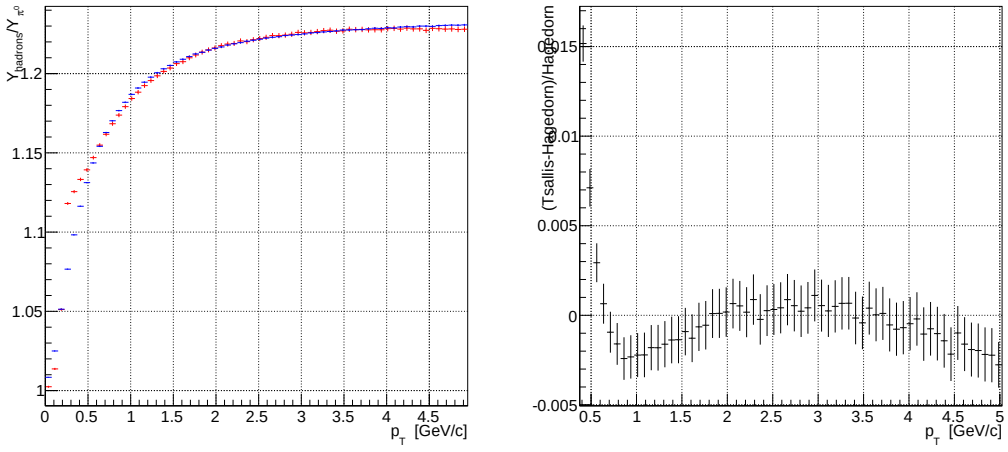

(a) Cocktail ratio using a modified Hagedorn function and a m_T-scaling assumption for the shape (red) with parameters from [46] and individual Tsallis parametrizations for each source [53].

(b) Normalized difference (Tsallis-Hagedorn)/Hagedorn of the cocktail ratios on the left. In the relevant momentum range $p_T > 0.4\,\mathrm{GeV}/c$ the difference is smaller 1.5%.

Figure 3.18: Comparison of cocktail ratio in $p + p$ using parametrizations with modified Hagedorn functions and Tsallis functions.

Table 3.2: Hagedorn parameterizations of π^0 p_T spectra for different centrality classes [46], see Eq. (3.24) for their use. Since fits to the experimental spectra are used to extract all parameters of Eq. (3.24) c cannot be interpreted as a normalization constant. $\mathrm{d}N/\mathrm{d}y$ gives the p_T-integrated π^0 yield into one unit in rapidity.

centrality	c	a	b	p_0	n	$\mathrm{d}N/\mathrm{d}y$
0-10%	1331.0	0.5654	0.1945	0.7429	8.361	280.9
10-20%	1001.0	0.5260	0.1628	0.7511	8.348	200.6
20-30%	750.7	0.4900	0.1506	0.7428	8.299	140.5
30-40%	545.3	0.4534	0.1325	0.7525	8.333	93.8
40-50%	364.5	0.4333	0.1221	0.7385	8.261	59.2
50-60%	231.2	0.4220	0.1027	0.7528	8.220	35.0
60-70%	118.1	0.4416	0.0559	0.7320	8.163	17.9
70-80%	69.2	0.2850	0.0347	0.7787	8.532	8.8
80-92%	51.1	0.2470	0.0619	0.7191	8.453	5.0

π^0 m_T spectrum from [46] for η' and ω mesons, and from [54] for η mesons. Table 3.3 summarizes the centrality-independent ratios we use.

Table 3.3: Meson yields relative to π^0 yield, scale factor determined at $p_T = 5\mathrm{GeV}/c$.

meson	yield relative to π^0	reference
π^0	1	defined
η	0.46 ± 0.06	[54]
η'	0.25 ± 0.075	[46]
ω	0.90 ± 0.06	[46]

The systematic uncertainty in the cocktail ratio from the hadrons to π^0 production was evaluated with a Monte Carlo simulation. The individual p_T distributions of all hadron were calculated and scaled with the hadron to π^0 production ratios sampled many times from Gaussian distributions centered around the nominal values with widths corresponding to the individual systemtatic uncertainties. The relative uncertainty is found to be largest at large p_T where it is around 2.2%, see Fig. 3.19 for the numerical

value and more details. For the final cocktail ratio we assign a conservative systematic uncertainty of 2.5% for all p_T to account for all uncertainties. We use a relative uncertainty constant in p_T to account for additional small systematically uncertainties, e.g. from the used parameterization of the pion data (see Fig. 3.18) or the assumed validity of the m_T-scaling assumptions down to small p_T; a systematic uncertainty flat in p_T can cover all of these since the systematic uncertainty on the cocktail ratio becomes small at small p_T, exactly where the other contributors become less certain.

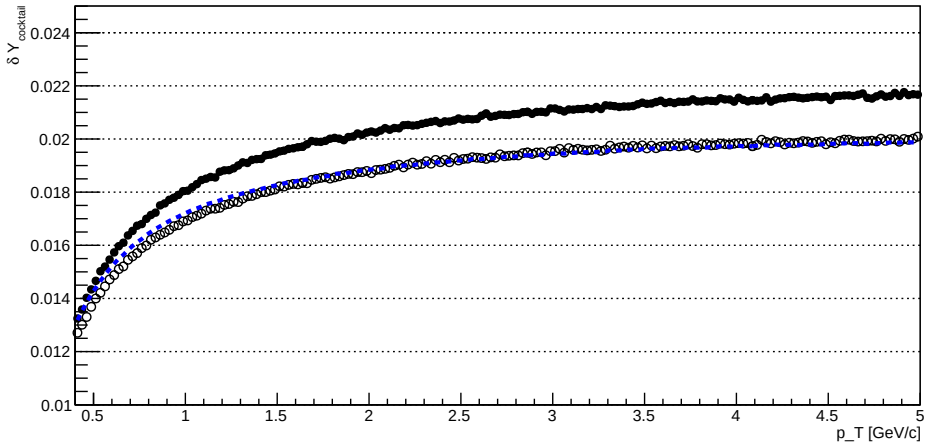

Figure 3.19: Relative uncertainty on the cocktail ratio taking into account all hadron to π^0 production rate uncertainties (•), and only the uncertainty from the η/π^0 production rate (◦). The blue dashed line is an analytical form $\delta Y_{\text{cocktail}} = \frac{0.06/0.46}{Y_{\text{cocktail}}} \frac{Y_{\text{cocktail}}-1}{Y_{\text{cocktail}}}$ which can be derived when assuming all uncertainty only coming from the η production rate and with identical shape of the p_T distributions of η and π^0 mesons.

We can calculate the yield ratio between the yield of photons from all hadrons and from π^0 decays. If a source would produce photons in secondary decays of π^0 daughter particles we do not double-count these photons but instead calculate the yield from π^0 decays exclusively from primary π^0. The final centrality-dependent yield from all hadron decays and from π^0 decays exclusively are shown in Fig. 3.20; their ratios, the centrality-dependent cocktail ratios $Y_\gamma^{\text{hadrons}}/Y_\gamma^{\pi^0}$ are shown in Fig. 3.21.

3.6 R_γ results from the 2010 data set

As a first intermediate result we calculate the ratio of the inclusive and photon yield from π^0 decays with Eq. (3.4) which is independent of model assumptions since $\langle \varepsilon f \rangle$ has virtually no model dependence on the used π^0 p_T distribution. We use yields N_{ee}

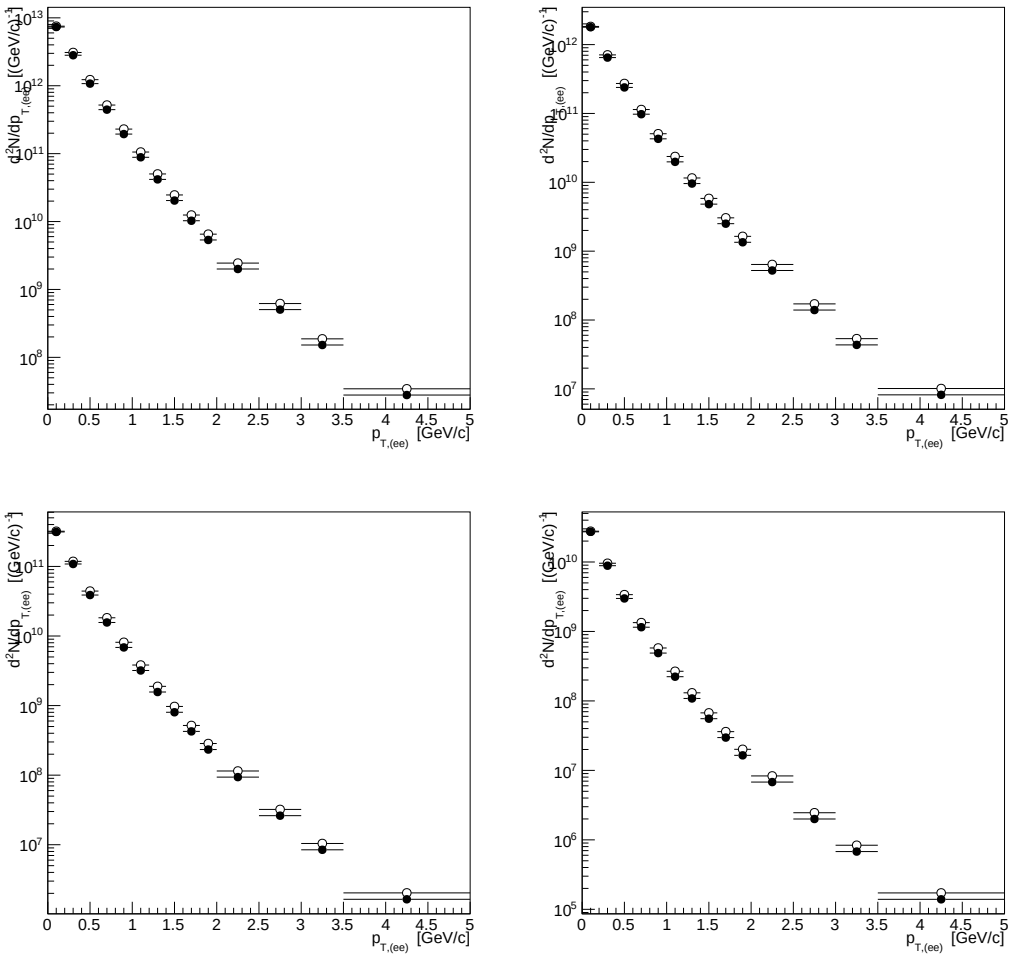

Figure 3.20: Simulated converted photon spectra of all photons (open circles) to photons from π^0 decays (filled circles) in 20% centrality bins, going from more central to less central, 0-20%, 20-40%, 40-60% and 60-92%. Systematic uncertainties are not shown.

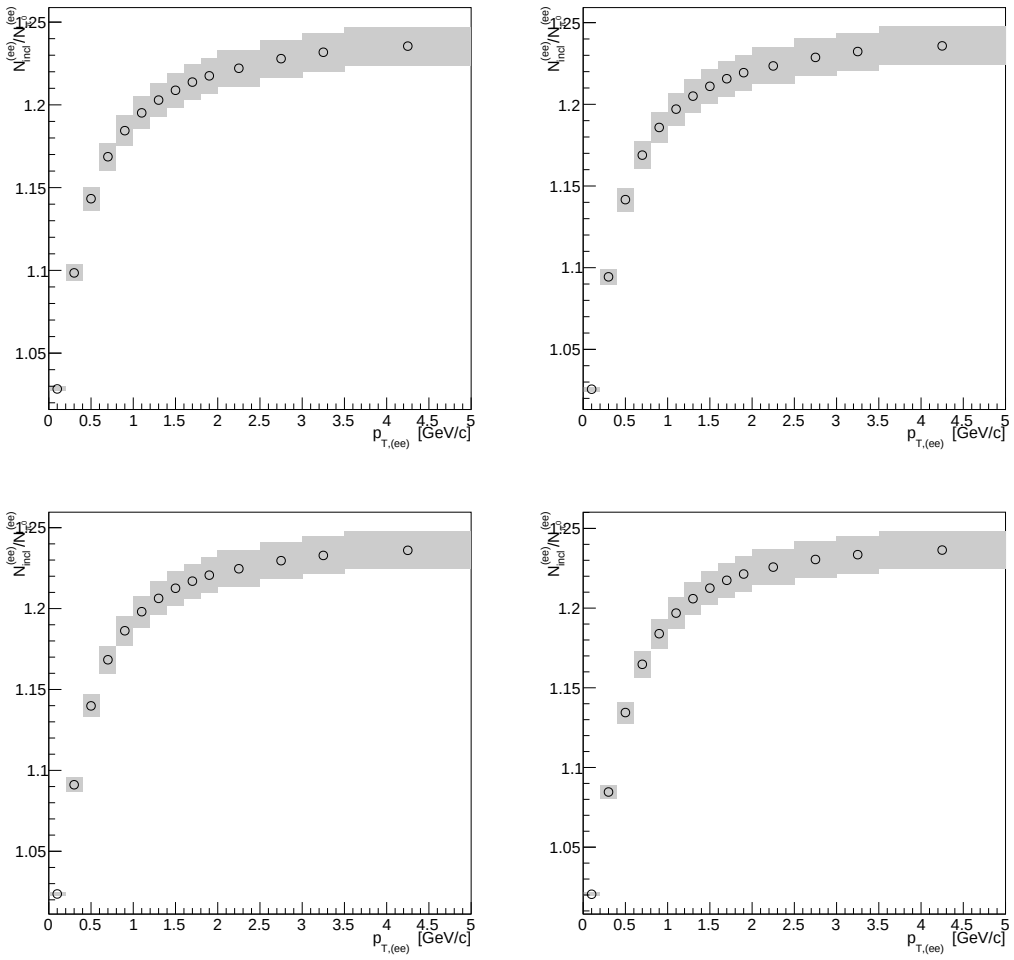

Figure 3.21: Simulated ratio of all photons to photons from π^0 decays in 20% centrality bins, going from more central to less central, 0-20%, 20-40%, 40-60% and 60-92%.

Table 3.4: Summary of systematic uncertainties on R_γ. Uncertainties are classified by type: Type A uncertainties are p_T-uncorrelated, Type B uncertainties are p_T-correlated, and Type C uncertainties correspond to overall scale uncertainties. We fold type A uncertainties into the statistical uncertainties.

Source	$\sigma_{\text{syst}}/R_\gamma$	Type
π^0 reconstruction		
(tagged photon yield)	4%	A
γ purity	1%	C
conditional acceptance		
energy scale	4%	B
conversion loss	2%	C
γ efficiency	1%	B
active area	1%	C
input p_T spectra	1%	B
$\gamma^{\text{hadron}}/\gamma^{\pi^0}$		
η/π^0 ratio	2.2%	C
other mesons	<1%	C

and $N_{ee}^{\pi^0}$, and conditional acceptance corrections $\langle \varepsilon f \rangle$ determined in the same centrality bins 0-20%, 20-40%, 40-60% and 60-92% and with identical, final binning in p_T. The systematic uncertainties are summarized in Table 3.4. The resulting yield ratios are shown in Fig. 3.22. Using the known cocktail ratios of photons from π^0 and all hadron decays

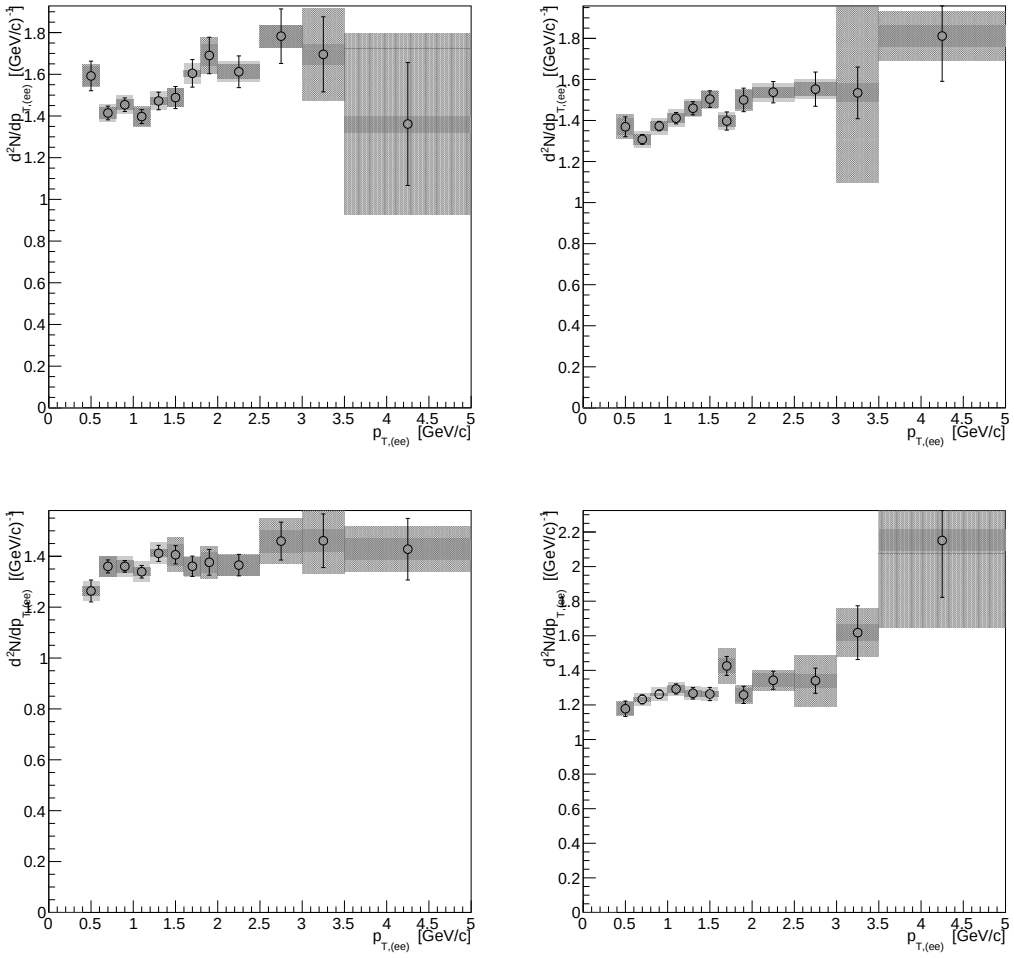

Figure 3.22: Data ratios $Y_\gamma^{\text{incl}}/Y_\gamma^{\pi^0}$ in centrality bins 0-20%, 20-40%, 40-60% and 60-92%, also see Eq. (3.4). These data ratios are practially model-independent measurements since $\langle \varepsilon f \rangle$ has virtually no model dependencies on the used π^0 parametrizations.

$Y_\gamma^{\text{hadrons}}/Y_\gamma^{\pi^0}$, see Fig. 3.21, we can then calculate R_γ with Eq. (3.5). Here the cocktail ratios were again calculated for centrality bins 0-20%, 20-40%, 40-60% and 60-92% and in the same final p_T binning as all other components in R_γ. The centrality-dependent results for R_γ are shown in Fig. 3.23. We find that like expected R_γ is very close to but slightly above unity in most peripheral collisions. That R_γ is slightly above unity can be due to

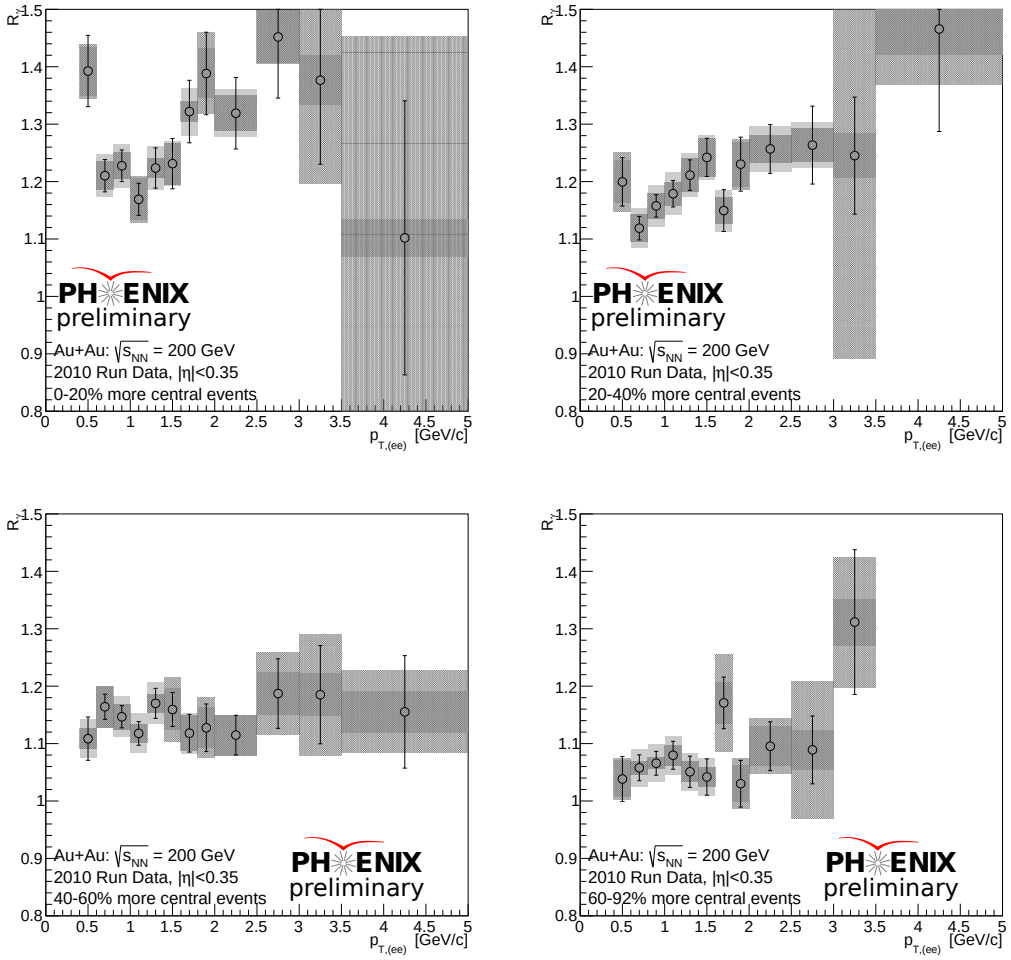

Figure 3.23: Final R_γ in centrality bin 0-20%, 20-40%, 40-60%, and 60-92%. The light gray boxes represent point-by-point correlated systematic uncertainties, the lines p_T-uncorrelated statistical uncertainties.

the most peripheral bin 60-92% still seeing a sizeable fraction of medium-induced effects from the more central events with centrality around 60%. Going to more central events we see the average value of R_γ increase monotonically with centrality with R_γ showing very little dependence on p_T.

Since R_γ is a fully corrected quantity, we are now in a position to perform additional systematic checks by changing cuts. Changes in cuts would change $\langle \varepsilon f \rangle$ and simultaneously the observed raw yields so that if the cut was modelled well the result for R_γ would be identical (but for changes in the statistical uncertainties).

We first test our modelling of the EMCal photon p_T cut which is the dominant effect determining the conditional acceptance $\langle \varepsilon f \rangle$ by repeating the whole analysis using different EMCal photon p_T cuts. Since $\langle \varepsilon f \rangle$ is a strong function of the EMCal photon p_T cut any problems would show up as dramatically different R_γ measurements for different cuts. Specifically, we repeated the whole analysis and calculation of $\langle \varepsilon f \rangle$ for cuts $p_T > 0.2, 0.3, \ldots, 1.0\,\mathrm{GeV}/c$. In Fig. 3.24 we compare the R_γ results with closely spaced cuts $p_T > 0.3, 0.4, 0.5\,\mathrm{GeV}/c$ where statistical uncertainties in the results do not change too much with respect to the nominal cut value and find no significant differences when changing p_T cuts. More dramatic variations in the cuts show similar consistency inside statistical uncertainties.

As a second check we evaluate how insufficient description of detector edges might influence the results for R_γ and repeat the analysis far away from central arm detector edges. Figure 3.25 shows the measured ϕ distribution of reconstructed conversion pairs. To select a sample of converted photons from electrons away from a central arm detector edges we restrict our analysis to converted photons emitted into the middle of one arm,

$$0 < \phi_{(ee)} < 0.5 \text{ or } 2.65 < \phi_{(ee)} < 3.15 \tag{3.26}$$

We then repeat the yield extraction procedure with a conditional acceptance correction for that particular acceptance, and produce R_γ measurements. Since the directions of converted and calorimeter photons are strongly correlated restricting the converted photon to same angle indirectly restricts the angular distribution of calorimeter photons as well and probes our assumption of uniform efficiencies in the EMCal subdetectors. The measurements in this narrower acceptance are compatible inside statistical uncertainties with the measurement made using the full acceptance, see Fig. 3.26, and we do not include an additional systematic uncertainty for any mismatch between data and simulation with respect to detector edges.

In Section 3.7 and 5 we discuss the direct photon yield further.

3.7 The 2010 and 2007 R_γ results

In the previous section we have shown how R_γ was calculated for the 2010 data set. In Section 3.4 we presented a fast, parametric Monte Carlo model for the detector response

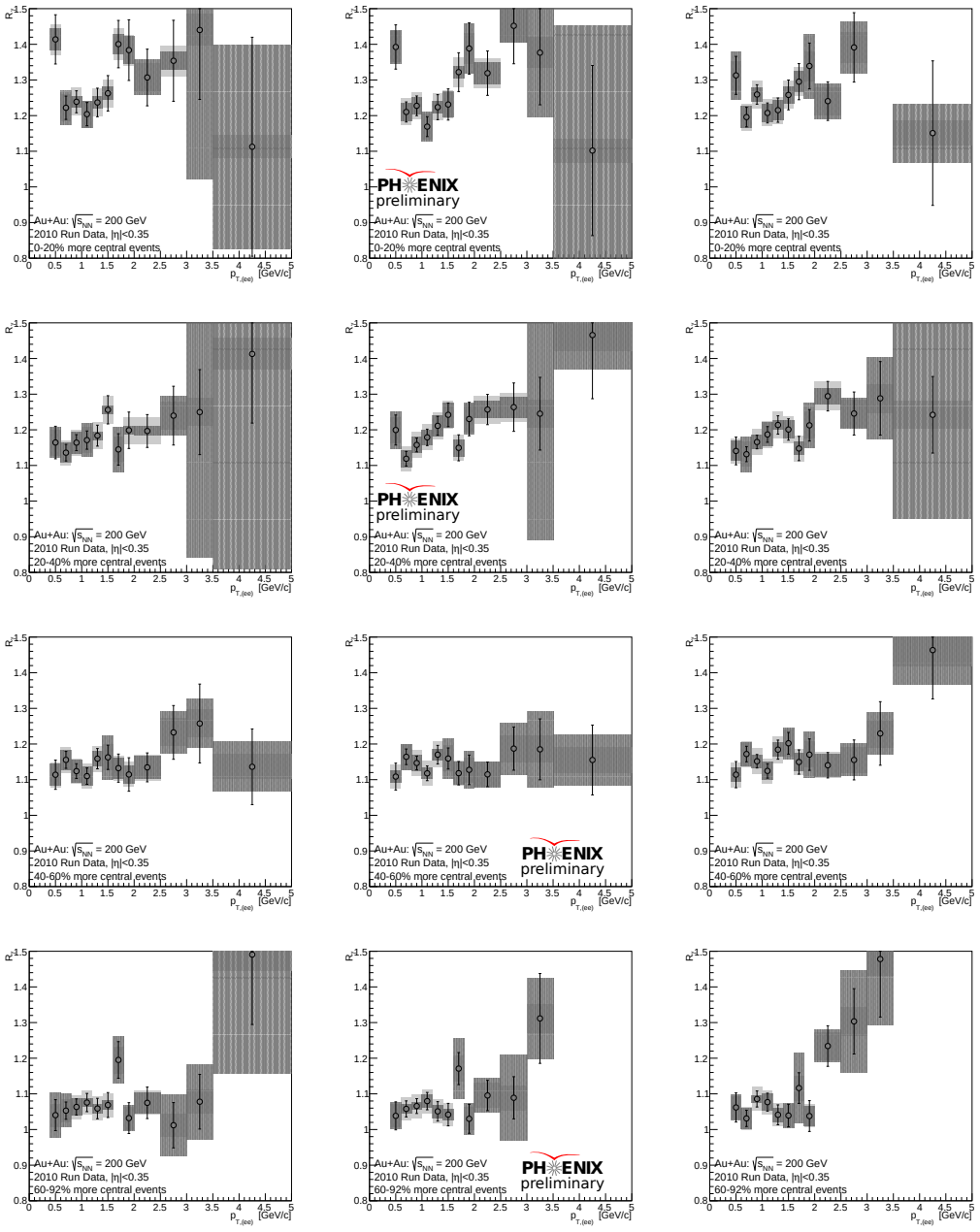

(a) $p_T > 0.3\,\mathrm{GeV}/c$ (b) $p_T > 0.4\,\mathrm{GeV}/c$ (c) $p_T > 0.5\,\mathrm{GeV}/c$

Figure 3.24: Centrality-dependent R_γ for different EMCal photon p_T cuts. The different rows correspond to centrality bins 0-20%, 20-40%, 40-60% and 60-92%. For all cuts the same cocktail ratio $Y_\gamma^{\mathrm{hadrons}}/Y_\gamma^{\pi^0}$ was used. We find no dependence of R_γ on the p_T cut used. The results for $p_T > 0.4\mathrm{GeV}/c$ are identical to the nominal results shown in Fig. 3.23. Also see there for definitions of the shown uncertainties.

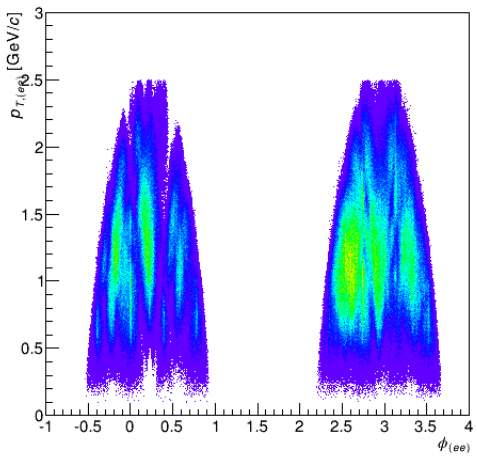

Figure 3.25: ϕ distribution of reconstructed converted photons.

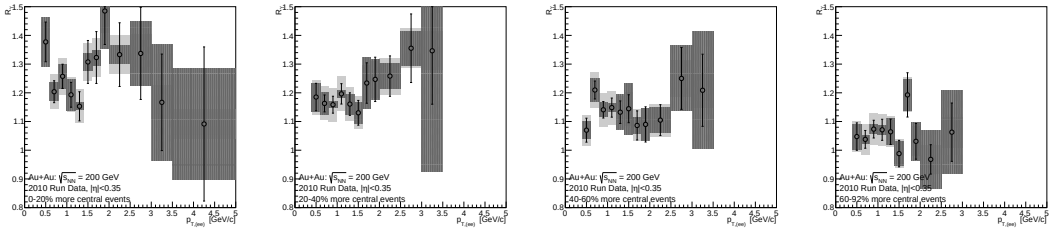

(a) In narrow acceptance

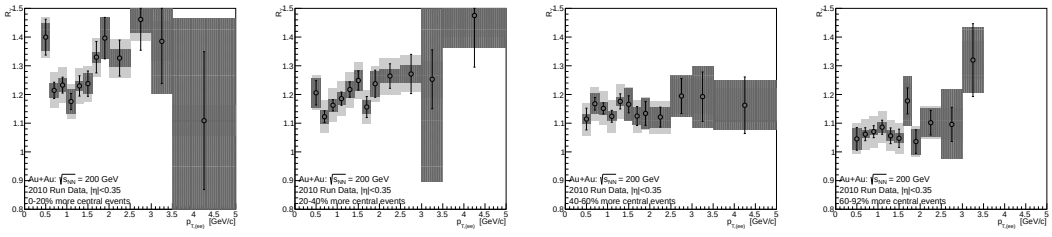

(b) In nominal acceptance

Figure 3.26: R_γ for $p_T > 0.4\text{GeV}/c$ in 0-20%, 20-40%, 40-60% and 60-92% centrality bins for the narrow acceptance and the nominal acceptance. Error bars are the statistical uncertainties, dark grey boxes per-point yield extraction uncertainties and light grey boxes the combined correlated systematic uncertainty. See also Fig. 3.23.

used for the calculation of the tagging efficiency correction $\langle \varepsilon f \rangle$. The method of using external conversion pairs was first developed and used to analyze 2007 data [39]. There the response of the detector was modeled with a full Monte Carlo simulation with the GEANT3 [55]-based detector-specific simulation package PISA which while computationally demanding should be able to capture the full physics of final state particle transport and reconstruction with the detector. Having these two technically independent measurements of R_γ allows us to evaluate the quality of the fast Monte Carlo. Also, the two measurements can be combined to increase the sample size and decrease statistical uncertainties.

In both 2007 and 2010 the yield of direct photons was measured via the double ratio R_γ defined in Eq. (3.5) composed of an efficiency- and acceptance-corrected data ratio in the numerator and a simulated yield ratio in the denominator. Since the acceptance of the detector was not identical in both years we can only compare efficiency- and acceptance-corrected physical quantities; we e.g. do not expect the ratio $\frac{N_{ee}^{\text{incl}}}{N_{ee}^{\pi^0}}$ to be identical between 2007 and 2010, but the numerators of Eq. (3.5) should be compatible in statistical uncertainties. The denominator in Eq. (3.5) only depends on fully corrected yields of hadrons and π^0 and their branching ratios to photons, so the 2007 and 2010 denominators are constructed identical.

The fast Monte Carlo simulation was constructed in such a way that adjusting it for the 2007 conditions requires only determining the centrality-dependent 2007 single photon efficiency ε and determining the detector live area for calorimeter photons (i.e. a list of live towers in the calorimeter), and for electrons and positrons (i.e. acceptance maps in electron ϕ and q/p_T analog to the 2010 Fig. 3.13). The 2007 analysis did not use run group-dependent fiducial cuts. From these run-specific inputs a 2007 $\langle \varepsilon f \rangle$ can be calculated. In Fig. 3.27 we show the relative difference between the tagging efficiency correction $\langle \varepsilon f \rangle$ calculated with the fast Monte Carlo and the full PISA simulation. We find that differences are smaller than the typical systematic uncertainties associated with either method and that both models agree well. This allows us to use a tagging efficiency corrections $\langle \varepsilon f \rangle$ calculated with the same fast Monte Carlo model for both the 2010 and 2007 data sets with their systematic uncertainties completely correlated.

We can then calculate combined 2007+2010 results by averaging the corrected 2007 and 2010 data ratios, i.e. we calculate as a function of converted photon p_T

$$\text{data ratio}_{2007+2010} = \frac{1}{w_{2007} + w_{2010}} \left(\left(w \langle \varepsilon f \rangle \frac{N_{ee}^{\text{incl}}}{N_{ee}^{\pi^0}} \right)_{2007} + \left(w \langle \varepsilon f \rangle \frac{N_{ee}^{\text{incl}}}{N_{ee}^{\pi^0}} \right)_{2010} \right) \tag{3.27}$$

where the w_i are related to the point-by-point statistical uncertainties in the year-dependent ratios σ_i with $w_i = \sigma_i^{-2}$. We can use this data ratio to calculate R_γ Eq. (3.5) and the decay photon yield ratios shown in Section 3.5.

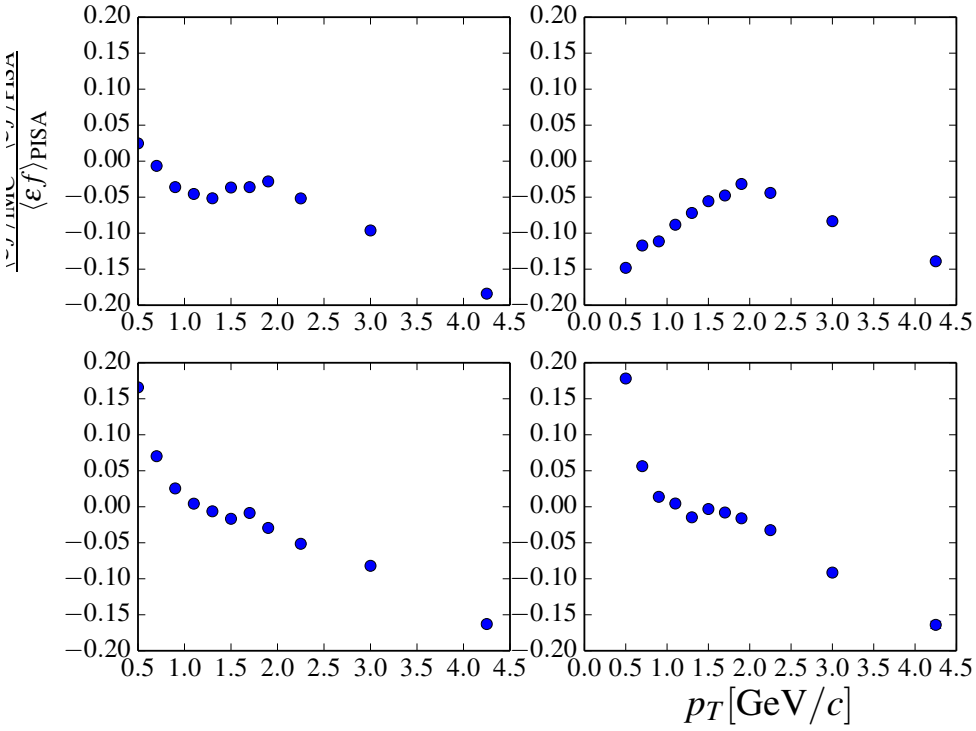

Figure 3.27: Comparisons of photon tagging efficiencies $\langle \varepsilon f \rangle$ for the 2007 data set calculated with a full PISA simulation $\langle \varepsilon f \rangle_{\mathrm{PISA}}$ and the fast Monte Carlo described in Section 3.4 $\langle \varepsilon f \rangle_{\mathrm{fMC}}$. The panels are centrality bins 0-20%, 20-40%, 40-60% and 60-92%. Plotted is $\frac{\langle \varepsilon f \rangle_{\mathrm{fMC}} - \langle \varepsilon f \rangle_{\mathrm{PISA}}}{\langle \varepsilon f \rangle_{\mathrm{PISA}}}$ as a function of photon p_T. The systematic uncertainty on either $\langle \varepsilon f \rangle$ is $\sim 5\%$ and we find good agreement.

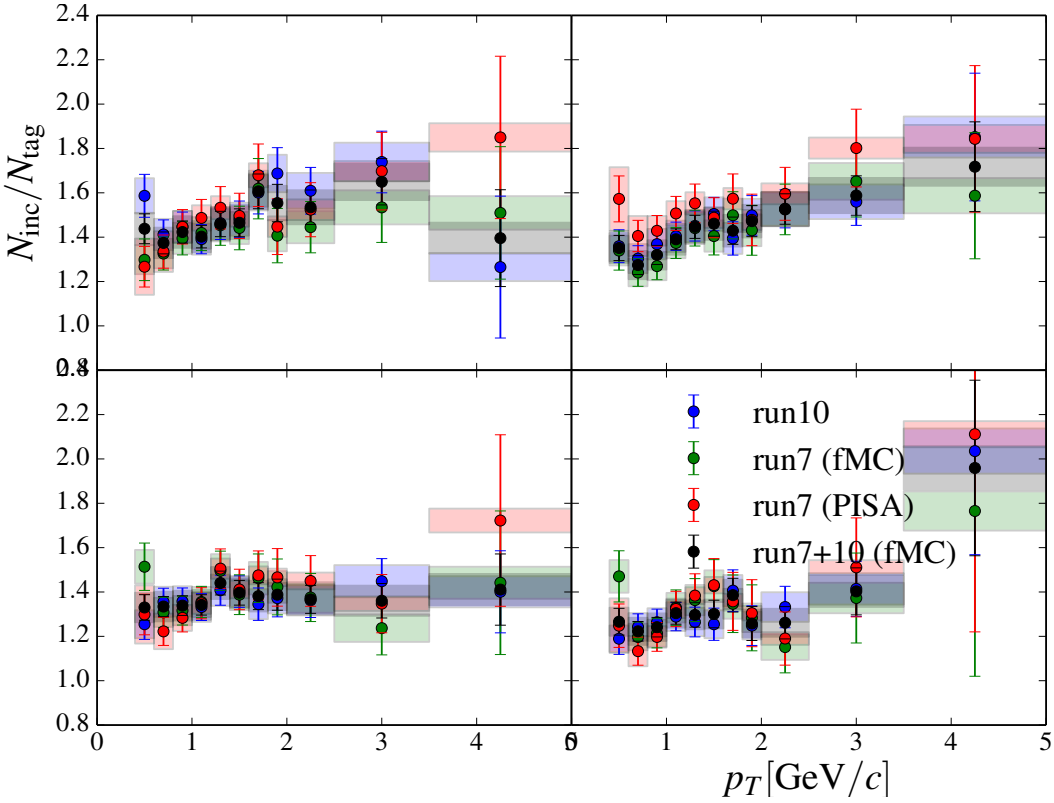

Figure 3.28: The tagging efficiency-corrected data ratios from 2007 and 2010, corrected either with a correction measured in a full PISA simulation (PISA) of with a fast Monte Carlo (fMC). The panels are centrality bins 0-20%, 20-40%, 40-60% and 60-92%.

In Fig. 3.28 we show the tagging efficiency-corrected data ratios calculated for the different data sets calculated with the fast Monte Carlo and the full PISA simulation. We also show the combined 2007+2010 measurement where both measurements have been corrected with the fast Monte Carlo correction. Again we find good agreement between the different measurements so that we calculate R_γ with Eq. (3.5). The different R_γ are shown in Fig. 3.29 where we find consistent measurements across data sets and methods. In Fig. 3.30 and Fig. 3.31 we compare our results to the R_γ obtained in an analysis using an extrapolation of a virtual photon measurement extrapolated to the photon point $m = 0$ [11] and find consistency as well.

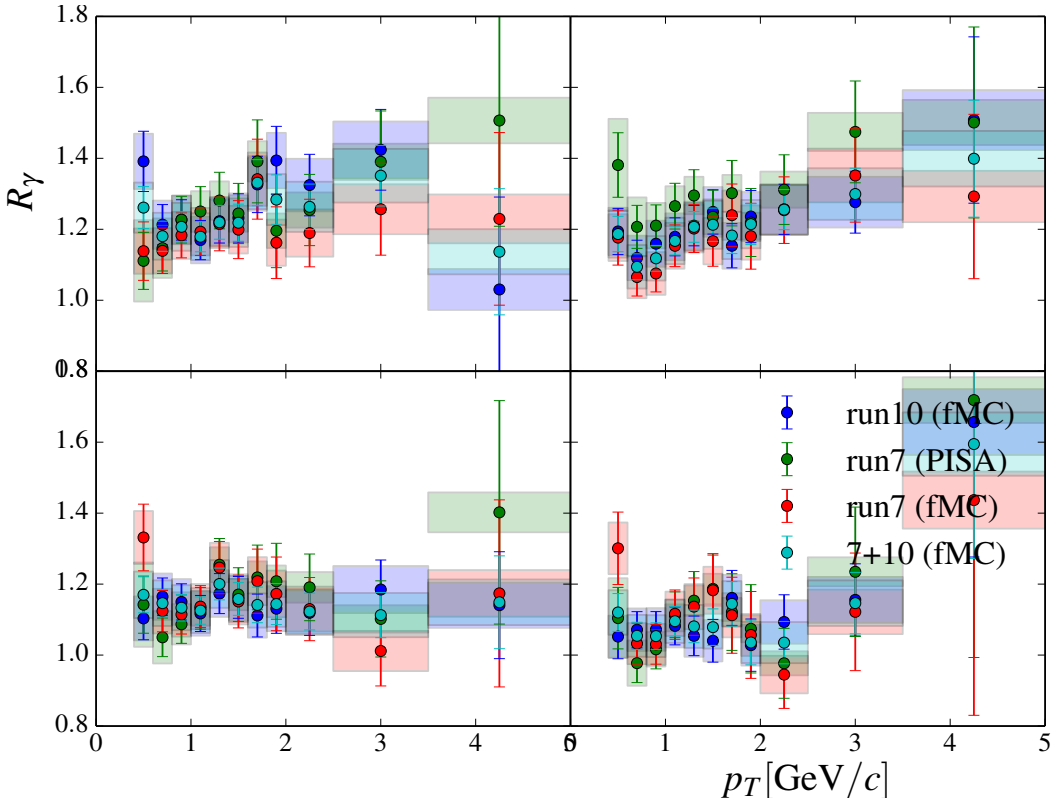

Figure 3.29: R_γ from the 2007 and 2010 dataset using a tagging efficiency derived from a from a full PISA simulation (PISA) and from a fast Monte Carlo (fMC). The panels are centrality bins 0-20%, 20-40%, 40-60% and 60-92%. R_γ is calculated using the same cocktail ratio for all data sets.

To calculate R_γ for a minimum bias sample, we sum the yields N_{ee}^{incl} and $N_{ee}^{\pi^0}$ measured in each centrality class. To obtain minimum bias efficiency corrections $\langle \varepsilon f \rangle$ we calculated the centrality-dependent yields of all and the π^0-decay tagged photons in each centrality class; since centrality-dependent π^0 yields where used the minimum bias $\langle \varepsilon f \rangle$ is the ratio of the centrality-summed yields. Similarly, the cocktail ratios where obtained by summing

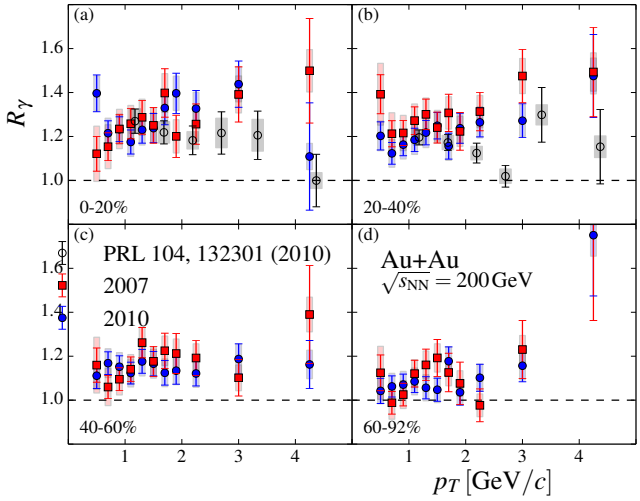

(a) R_γ for 2007 and 2010 measurements separately. The 2007 measurement uses a tagging efficiency correction $\langle \varepsilon f \rangle$ derived from a full detector Monte Carlo simulation; the 2010 measurement uses the fast Monte Carlo described in Section 3.4.

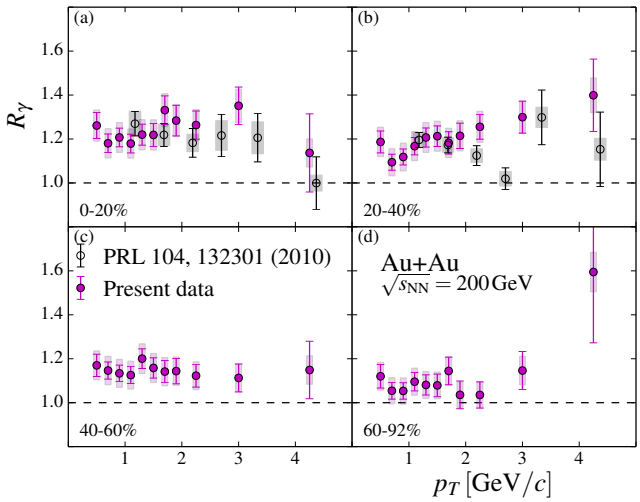

(b) R_γ for the combined 2007+2010 measurement. Both measurements use a efficiency correction $\langle \varepsilon f \rangle$ derived from the fast Monte Carlo described in Section 3.4.

Figure 3.30: R_γ from the 2007, 2010 and 2007+2010 combined measurement compared to the 2004 virtual photon measurement [11]. The different panels are centrality bins 0-20%, 20-40%, 40-60% and 60-92$. All measurements are consistent within uncertainties.

centrality-dependent photon yields from all hadron and π^0 decays exclusively and taking the ratio of the summed yields.

These comparisons show that the fast Monte Carlo correction produces results equivalent to the full PISA simulation and consistency with the virtual photon analysis [11]. To ensure maximally correlated systematic uncertainties when combining the 2007 and 2010 measurements will subsequently use the fast Monte Carlo calculation for both data sets.

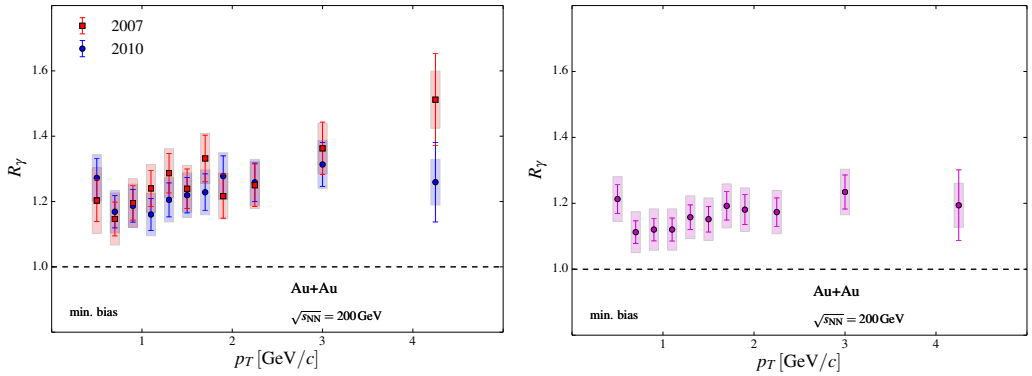

(a) See Fig. 3.30a

(b) See Fig. 3.30b

Figure 3.31: Like Fig. 3.30, but for a minimum bias sample.

3.8 Summary

We have measured the relative direct photon yield R_γ in four centrality classes in the low momentum range, $0.4\,\text{GeV}/c < p_T < 5.0\,\text{GeV}/c$

- While R_γ approaches unity, i.e. a minimal direct photon signal, in peripheral collisions, its magnitude increases towards more central collisions, revealing an increasing direct photon signal.
- With our uncertainties R_γ is roughly featureless and flat with p_T over the whole covered momentum range.

Chapter 4

Direct photon flow

In Chapter 3 we have shown how a clean sample of real photons can be measured in external conversions to electron-positron pairs. In this chapter we will use that same photon sample to measure correlations of the measured photons with the event plane.

4.1 Method

4.1.1 Measurements of anisotropies

We start with the same list of runs and sample of inclusive photons described in Chapter 3. We then measure the uncorrected anisotropies $v_n^{i\prime}$ against reaction planes in the RXP and MPC detectors where the prime denotes an uncorrected quantity. With ϕ the azimuthal angle of a reconstructed photon and Ψ_k^i the angle of the kth reaction as measured in detector i with $n = km$ the $v_n^{i\prime}$ can be calculated as

$$v_n^{i\prime} = \langle \cos km(\phi - \Psi_k^i) \rangle \tag{4.1}$$

where the angle brackets denote the average over the photon sample and $m = 1, \ldots$. This simple relation follows from the orthogonality of the different Fourier components of the correlation function $\mathrm{d}N/\mathrm{d}(\phi - \Psi_k^i)$ and allows to measure the nth Fourier coefficient with the same or any lower order event plane Ψ_k as long as n is an integer multiple of k.

Alternatively the anisotropies can be extracted from fits of the v_n' to the correlation function

$$\frac{\mathrm{d}N}{\mathrm{d}(\phi - \Psi_k^i)} \propto 1 + \sum_{k=1}^{\infty} v_{km}^{i\prime} \cos km(\phi - \Psi_k^i) \tag{4.2}$$

but in this work we use the averages as defined in Eq. (4.1) to extract the coefficients.

4.1.2 Resolution corrections

To recover the actual anisotropies v_n in each detector the measured anisotropies v'_n need to be corrected for finite resolution effects.

$$v_n^i = \frac{v_n^{i\prime}}{\mathrm{Res}(v_n^i)} \tag{4.3}$$

The resolution corrections $\mathrm{Res}(v_n^i)$ can be determined by a number of different methods. In this analysis we use the 2- and 3-subevent methods [56, 57]

2-subevent method The 2-subevent method divides the measurement in a detector into two equally-sized subevents with similar coverage. Here we measure the reaction plane angles Ψ_k by combining hits in the north and south halfs of the RXP or MPC detectors, and it is natural to to form subevents by only using hits in the north or south detectors. To estimate the resolution correction we measure from the north-south differences [56]

$$\langle \cos k m(\Psi_k^{\mathrm{North}} - \Psi_k^{\mathrm{South}}) \rangle = \sqrt{\frac{\pi}{8}} \chi e^{-\chi^2/4} \left(I_{\frac{k-1}{2}}(\chi^2/4) + I_{\frac{k+1}{2}}(\chi^2/4) \right) \tag{4.4}$$

where the I_ν are modified Bessel functions of order ν. Given a measured $\langle \cos k m(\Delta\Psi_k^{\mathrm{N,S}}) \rangle$ this relation can numerically be inverted to yield χ. Replacing χ with $\sqrt{2}\chi$ in above relation then gives the resolution correction for the north-south combined measurement. In our case we invert above relation with Brent's method using the implementation in ROOT [58]. Since the inverted function has a smooth dependence on χ any other reasonable root finding algorithm would arrive at similar results.

3-subevent method The 3-subevent method for the estimation of the resolution correction makes no assumption about equal samples sizes in the subevents, but instead uses two auxiliary subevents. To determine the resolution corrections for a measurement in detector A (e.g. from the north-south combined RXP measurement) we pick as auxiliary subevents subevents in another detector B and C (e.g. from the measurement in the north and south subdetector of the MPC). The resolution correction can be calculated from the observed differences between detectors

$$\mathrm{Res}(v_n^A) = \sqrt{\frac{\langle \cos n(\Psi_k^A - \Psi_k^B) \rangle \langle \cos n(\Psi_k^A - \Psi_k^C) \rangle}{\langle \cos n(\Psi_k^B - \Psi_k^C) \rangle}} \tag{4.5}$$

4.1.3 Direct photon v_n

With measured and resolution corrected inclusive photon anisotropies v_n^{incl}, a known yield ratio of inclusive photons to photons from hadron decays R_γ, and the photon anisotropies

expected from hadron decays v_n^{hadrons} the direct photon v_n^{direct} can directly be extracted with

$$v_n^{\text{direct}} = \frac{R_\gamma v_n^{\text{incl}} - v_n^{\text{hadrons}}}{R_\gamma - 1} \tag{4.6}$$

Since R_γ is only slightly larger than unity the direct photon v_n will strongly pick up any uncertainties in the input v_n.

In the following we will describe measurements of momentum anisotropies v_n. Like we will show in Section 4.2.1 the RXP detector has the better resolution when compared with the MPC detector and we will use it to measure the central values. Additionally we will use the MPC detector to evaluate systematic uncertainties.

4.1.4 Propagation of uncertainties

All statistical uncertainties are propagated as usual with Gaussian error propagation, i.e. for a quantity $y = f(x_1, x_2, \ldots)$ derived from inputs x_i the absolute uncertainty on y is

$$\Delta y = \sum_i \left| \frac{\partial y}{\partial x_i} \Delta x_i \right|^2 \tag{4.7}$$

The effect of systematic uncertainties in inputs are estimated by varying one input value at a time both up and down by σ_{sys} and recalculating the derived quantity while leaving all other inputs fixed at their respective nominal values. We then calculate the relative difference of the derived quantity with respect to the varied value. The total systematic uncertainty in the derived quantity from all inputs is then given by the quadratic sum of contributions, more specifically the relative uncertainty δ_i in $f(x_1, x_2, \ldots)$ due x_i to is estimated as

$$y\delta_y^i = \frac{1}{2}\left(\left| \frac{f(x_1, \ldots, x_i + \delta_i, \ldots) - f(x_1, x_2, \ldots)}{f(x_1, x_2, \ldots)} \right| + \left| \frac{f(x_1, \ldots, x_i + \delta_i, \ldots) - f(x_1, x_2, \ldots)}{f(x_1, x_2, \ldots)} \right| \right) \tag{4.8}$$

and the total systematic uncertainty is the quadratic sum of the individual contributions,

$$\Delta y_{\text{sys}} = \sqrt{\sum_i \left(y\delta_y^i \right)^2} \tag{4.9}$$

In the case of uncorrelated systematic uncertainties this method reproduces the Gaussian propagation in quadrature.

4.2 Analysis

4.2.1 Resolution corrections

The resolution corrections for the MPC and RXP detectors are shown in Fig. 4.1 for the centrality binning of the direct photon analysis and for 10% bins. They show the expected behavior with the RXP measurement needing less corrections than the measurement in the MPC. Also their behavior with centrality behaves as expected, e.g. the resolution corrections for v_2 measurements are small in most central collisions where the v_2 of the particles used to measure the reaction plane is so small that even the large yield of these particles cannot improve the resolution enough. Going to semi-central collisions the number of particles goes down, but since v_2 increases the resolution improves so that the correction is closer to unity. When going to peripheral and very peripheral collisions v_2 continues to increase, but the yield gets so small that ultimately we loose all resolution.

4.2.2 Measurements of anisotropies v_n

The v_n' are measured directly by averaging $\cos(mk(\phi - \Psi_k))$ in p_T bins. To be able to extract the direct photon v_n with Eq. (4.6) using the R_γ values shown in Fig. 3.23 we use the same binning in p_T and centrality as used when extracting R_γ.

Even though the event planes are measured in forward detectors with full coverage in azimuth and correlated with mid-rapidity particles measured with completely different detectors there is a possibility that detection biases could introduce non-zero v_n even if there was no true correlation between the measured photon and the event plane (in this case one should recover $v_n = 0$). To model these effects we create measurements v_n^{BG} where the event plane is completely uncorrelated to the photon by pairing photons with event planes from different events with similar collision vertex and centrality. The true, correlated and bias-corrected measurement is then

$$v_n = v_n^{\mathrm{FG}} - v_n^{\mathrm{BG}} \tag{4.10}$$

We find that v_n^{BG} is much smaller than v_n^{FG}, and typically smaller than the systematic uncertainty on v_n^{FG}.

Charged track v_n

To verify our resolution correction and v_n extraction procedure and to extract systematic uncertainties from a large sample we first measure the v_n of charged tracks. To select charged tracks we make the following standard selections:

- $p_T > 0.2\mathrm{GeV}/c$
- charge $\neq 0$

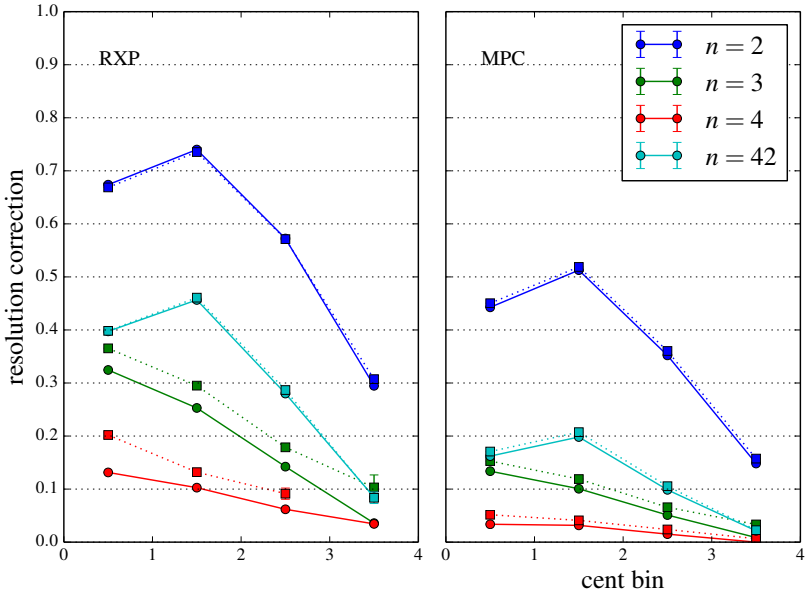

(a) Resolution correction for 20% centrality bins

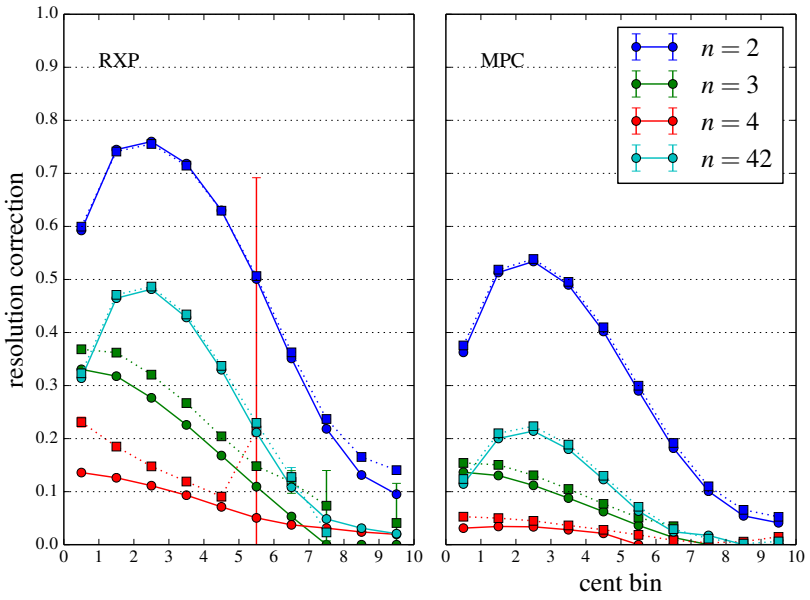

(b) Resolution correction for 10% centrality bins

Figure 4.1: Resolution corrections for the RXP and MPC. The centrality bins are 0-20%, 20-40%, 40-60% and 60-92% when for the first case and 0-10%, 10-20%, ..., 90-100% for the second case. The labels n correspond to the corrections for $v_2\{\Psi_2\}$, $v_3\{\Psi_3\}$, $v_4\{\Psi_4\}$ and $v_4\{\Psi_2\}$. The circle/full lines are from a 2-subevent correction, the squares/dashed lines from a 3-subevent correction. The relative differences between the different correction methods directly translate to a systematic uncertainty on the measured v_n.

- quality $\in \{31, 51, 63\}$
- $\Delta\phi < 2\sigma_{\Delta\phi}, \Delta z < 2\sigma_{\Delta z}$
- $n_0 = -9999$

The first three cuts select good charged tracks and are very similar to the cuts used for electrons in Section 3.2.1. Additionally, we here require a good match of the fitted track to the cluster reconstructed in the EMCal to reduce background from fake tracks, i.e. wrong trajectories reconstructed from uncorrelated detector hits in e.g. the tracking detectors, especially at large $p_T > 2\text{GeV}/c$, and also that no scintillation light was recorded in the RICH which mainly removes background from conversion electrons at low p_T. After resolution correction and background subtraction we arrive at the charged track anisotropies shown in Figs. 4.2 to 4.4 which are in generally good agreement with earlier measurements [59]. The small disagreement at low p_T might be due to the fact that our measurement is not corrected for occupancy effects which are known to produce small absolute offsets and are independent of p_T [60]; this effect would be especially noticeable when the v_n are small, e.g. at low p_T.

Inclusive photon v_n

We have confirmed that our method of resolution correction and v_n measurement produces charged track results consistent with earlier PHENIX measurements. To measure the raw inclusive photon v_n we can use the exact same procedure on our conversion photon sample. Our photon sample is identical to the photon sample used to calculate R_γ, see Section 3.2. Since systematic uncertainties are completely dominated by the resolution corrections we reuse the systematic uncertainties derived from that large statistics charged track sample. The resulting inclusive photon anisotropies are shown in Fig. 4.5 for smaller centrality bin, and in Fig. 4.6 after combining several centrality bins. We find that the inclusive photon v_n are roughly of the magnitude expected from hadron decays.

4.2.3 v_n for photons from hadron decays

To estimate the expected anisotropies of photons from hadron decays, which make up roughly 80% of the inclusive photon sample, a cocktail simulation is used. We already built a cocktail simulation for the yield of photons from hadron decays to determined R_γ, see Section 3.5. Since there we were only concerned with the yield of photons produced at midrapidity and not their correlation with event planes parent particles were produced without preferred emission angles. To correctly estimate hadron decay photon v_n the parent particles need to be correctly correlated with the event planes.

As a general procedure we will parametrize measured hadron v_n in the p_T range relevant for our decay photon sample and generate the parent particles according to them.

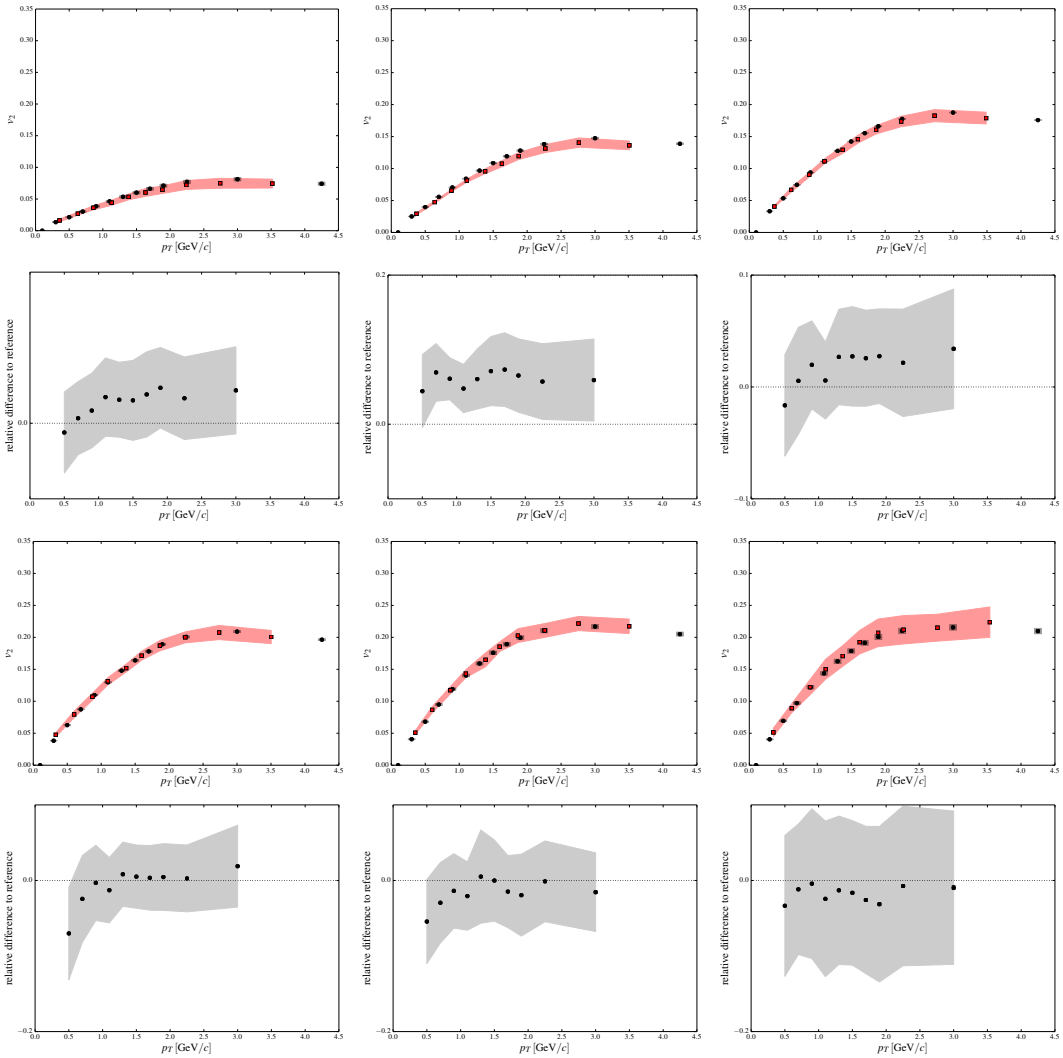

Figure 4.2: Charged track v_2 in 10% centrality bins from this measurement (black points) and reference [59], and relative difference of this measurement to reference (black points, gray bands). In comparison the reference is interpolated to the p_T of this measurement. Our measurement does not include a systematic uncertainty accounting for track sample impurity which is included in the reference.

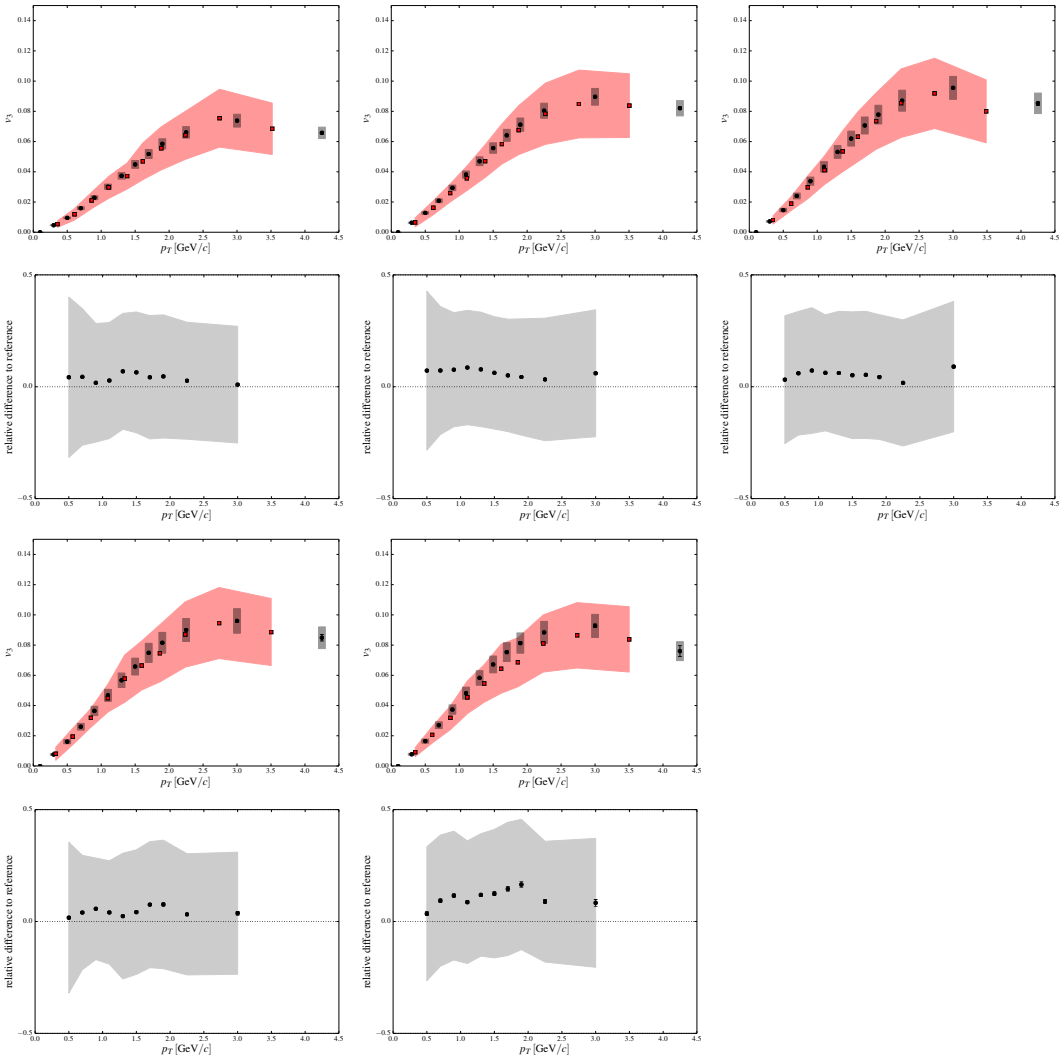

Figure 4.3: Charged track v_3 in 10% centrality bins and relative difference of this measurement to reference. Also see additional comments on page 81.

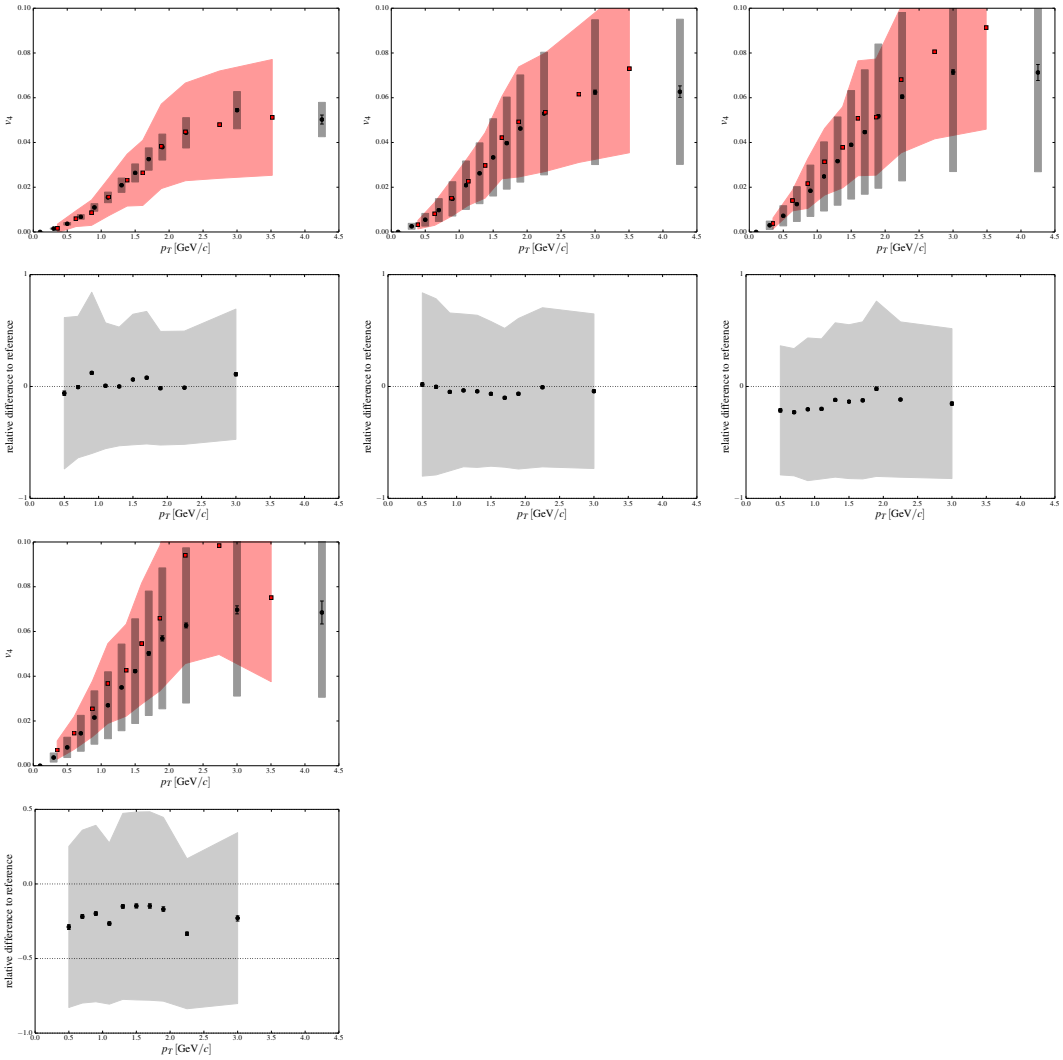

Figure 4.4: Charged track v_4 against the 4th order reaction plane in 10% centrality bins and relative difference of this measurement to reference. Also see additional comments on page 81.

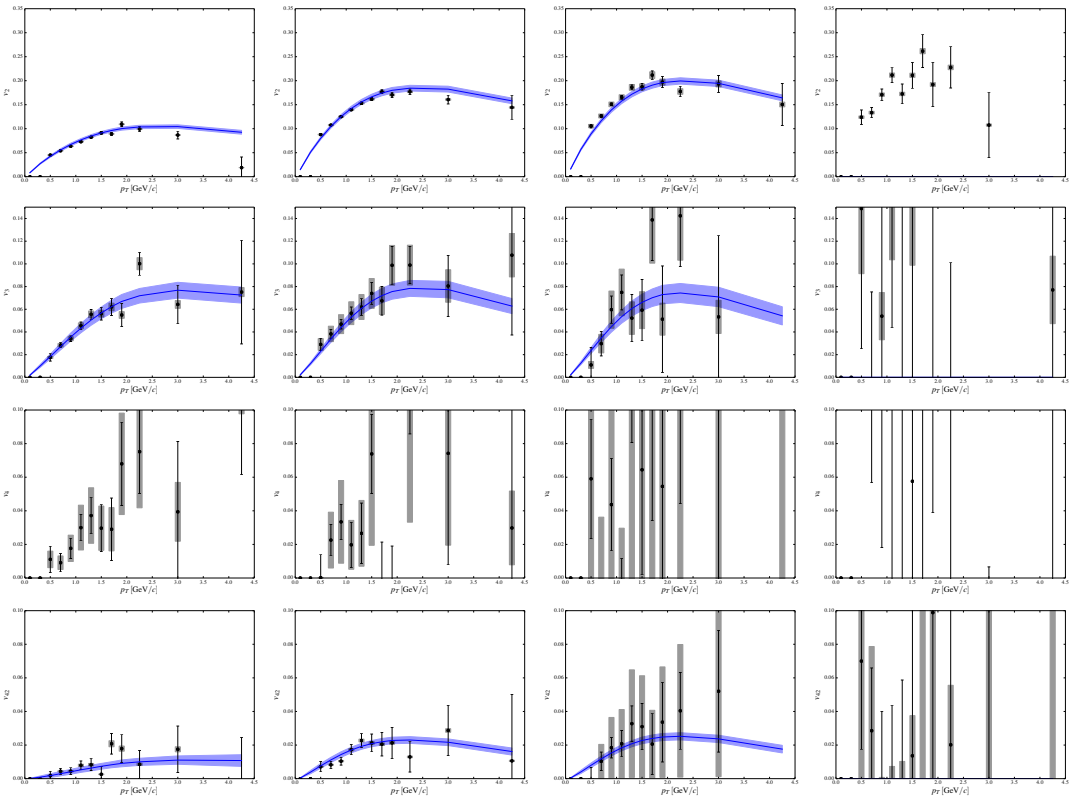

Figure 4.5: Inclusive photon v_n in centrality bins 0-20%, 20-40%, 40-60% and 60-92% (columns). The different rows show v_2, v_3, $v_4\{\Psi_4\}$ and $v_4\{\Psi_2\}$. The blue lines show expectations for photons from hadron decays calculated with the cocktail described in Section 4.2.3.

Since charged pion data has the smallest uncertainty in the low momentum range we are most interested in and hadron v_n are known to follow a scaling relation with their number of constituent quark [61], we will parametrize charged pion data [60, 62, 63] and estimate our hadron v_n with

$$\frac{v_n}{n_q^{n/2}} = N_1 \arctan(ax) + N_2(x^2 + bx)e^{-\lambda x} \tag{4.11}$$

where n_q is the number of quarks in the hadron, two for all sources we consider; the scaled kinetic energy $x = \frac{1}{n_q}\left(\sqrt{{p_T}^2 + m^2} - m\right)$, m the hadron mass and fit parameters N_1, N_2, a, b and λ all determined from charged pion data. We perform individual fits for each centrality and order, n is used just for consistency with published results. This parameterization captures the main features of the observed v_n:

- $v_n = 0$ for $p_T = 0$,
- $v_n =$ const. for $p_T \to \infty$, and
- a single peak in the low p_T range.

The systematic uncertainty in the hadron decay photon v_n comes primarily from two sources,

- a systematic uncertainty in the input data, and
- a fit uncertainty when parameterizing the data.

The fit uncertainty is given by the CL = 95% confidence intervals around the central values. Since the systematic uncertainty in the input data was determined as a relative uncertainty we assign the same relative uncertainty for each point of the parameterization. These two systematic uncertainties are uncorrelated and added in quadrature. To determine the systematic uncertainty of the hadron decay photon v_n we run our whole simulation for three set of input parameters: for the nominal value, and for all parent v_n moved up or down by 1σ of their full systematic uncertainty.

We explicitly account for acceptance effects in the data and can perform the simulation in any acceptance, e.g. in the full angle $0 < \phi < 2\pi$ and $|y| \leq 1$. Since no acceptance effects enter into the simulation we can put the angles of all event planes at $\phi = 0$; with that instead of generating ϕ and random event plane orientations generating just $\Delta\phi = \phi - \Psi_n$ is sufficient. In our parameterization Eq. (4.11) the hadron v_n depend on the particle p_T; this dependency makes generation of random $\Delta\phi$ with a naïve rejection sampling using functions $\mathrm{d}N/\mathrm{d}\phi(v_2, v_3, \ldots)$ like implemented in ROOT's `TF1` class unfeasible. Instead we use a modified rejection sampling algorithm which is an extended version of the algorithm used by the PHENIX Tsukuba group,

```
// v2, v3, v4 given
// ran() is a suitable RNG; we use TRandom3::Rndm()
do {
  // throw a random phi
  phi = 2*PI*ran();

  // calculate the even and odd dN/dphi values for this phi
  sim_ev = 1 + 2*v2*cos(2*phi) + 2*v4*cos(4*phi);
  sim_od = 1 + 2*v3*cos(3*phi);

  // calculate random dN/dphi values follow these vn
  ran_ev = (1 + 2*abs(v2) + 2*abs(v4)) * ran();
  ran_od = (1 + 3*abs(v3)) * ran();
} while (sim_ev<ran_ev or
         sim_od<ran_or);
return phi;
```

The resulting hadron decay photon anisotropies are again calculated by measuring $\langle \cos k m(\phi - \Psi_k) \rangle$, where we again use ROOT's `TProfile2D` in decay photon p_T and $\cos k m(\phi - \Psi_k)$. Since we explicitly used Ψ_k when throwing random angles these averages directly correspond to the expected hadron decay photon v_n (i.e. the resolution corrections are all 1 here). The input data with the parameterization and the generated source v_n are shown for charged pions in Figs. 4.7 to 4.9; the expectation for hadron decay photon v_n we already showed in Fig. 4.5 and 4.6

4.2.4 Direct photon v_n

Given the inclusive photon v_n calculated in Section 4.2.2 and the hadron decay photon v_n from 4.2.3 we can now calculate the direct photon v_n with Eq. (4.6). Since the hadron and inclusive photon v_n were measured in different data sets with e.g. different detector calibrations we cannot assume correlation of systematic uncertainties – in fact the resolution correction which directly depend on the event plane detector calibrations dominate the systematic uncertainties in the measurement. For that reason we here assume that systematic uncertainties in the decay and inclusive photon v_n measurements are completely uncorrelated.

The results for the direct photon anisotropies are shown in Fig. 4.10 and 4.11. Since $R_\gamma v_n^{\text{incl}}$ is not much larger than v_n^{decay} and the respective uncertainties are both not small and assumed to be uncorrelated many of the measurements, especially in more peripheral collisions or for higher n provide no strong constraints on the value of the anisotropy.

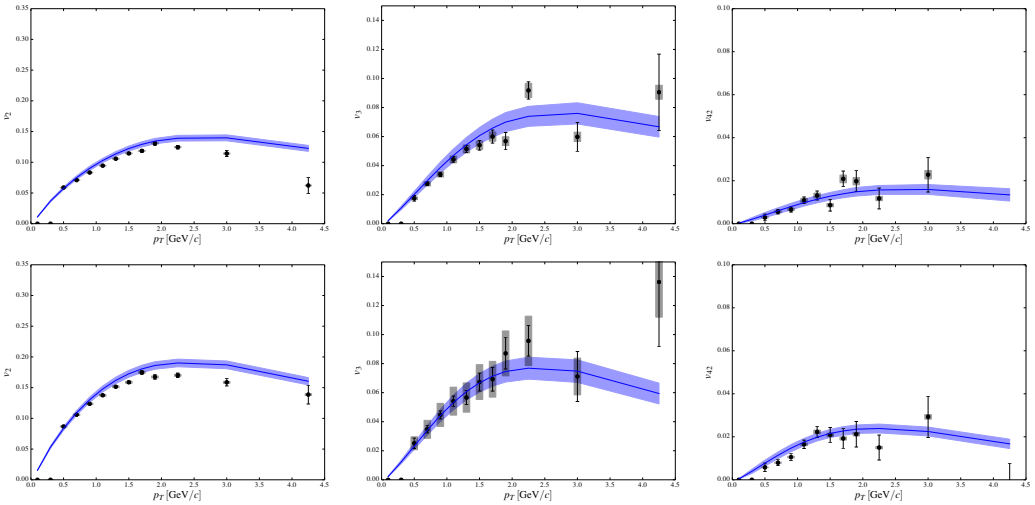

(a) v_2 in 0-60% and 20-60% (b) v_3 in 0-60% and 20-60% (c) $v_4\{\psi_2\}$ in 0-60% and 20-60%

Figure 4.6: Inclusive photon v_n in combined centrality bins. also see Fig. 4.5.

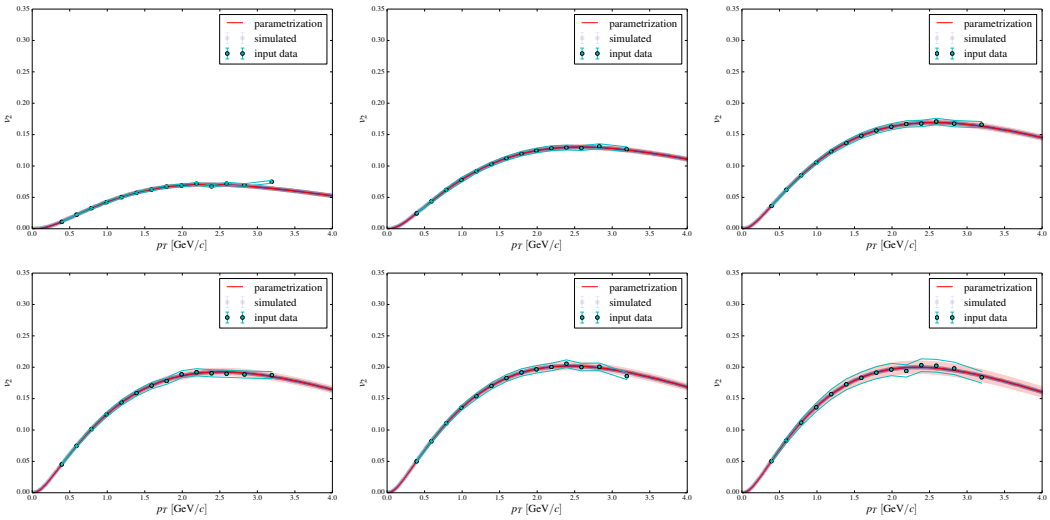

Figure 4.7: Simulated pion v_2 in centrality bins 0-10%, …, 50-60%. The red bands denote the quadratic sum of the systematic uncertainty in the input data and the uncertainty in the fit of the parametrization.

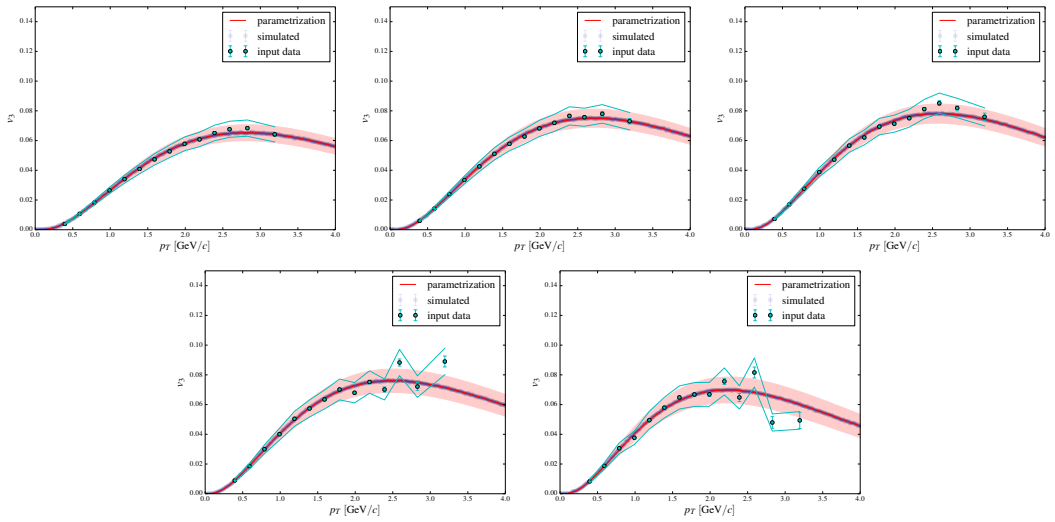

Figure 4.8: Simulated pion v_3 in centrality bins 0-10%, …, 40-50%. Also see Fig. 4.7.

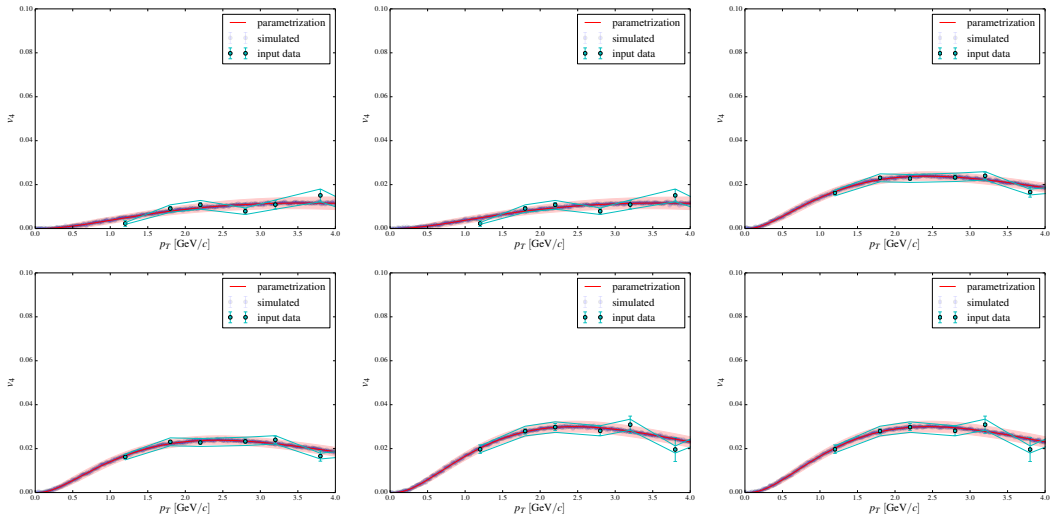

Figure 4.9: Simulated pion $v_4\{\Psi_2\}$ in centrality bins 0-20%, 20-40%, 40-60%. Also see Fig. 4.7.

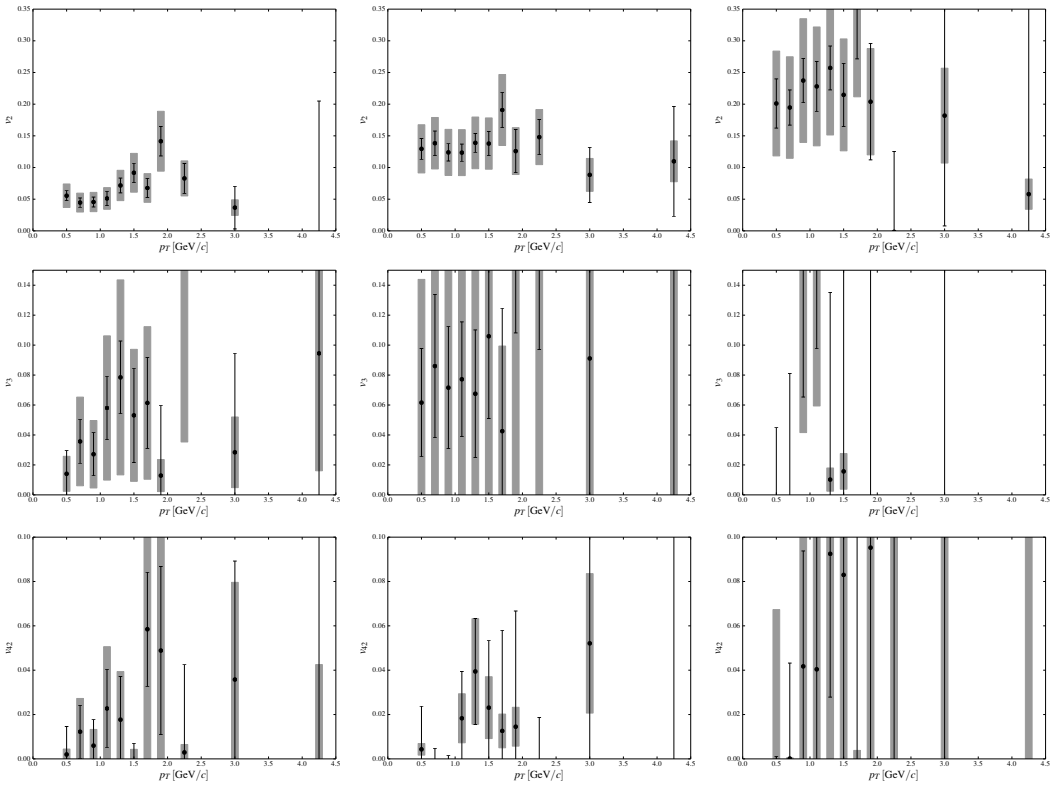

Figure 4.10: Direct photon v_n in centrality bins 0-20%, 20-40% and 40-60% (columns). The different rows show v_2, v_3 and $v_4\{\Psi_2\}$.

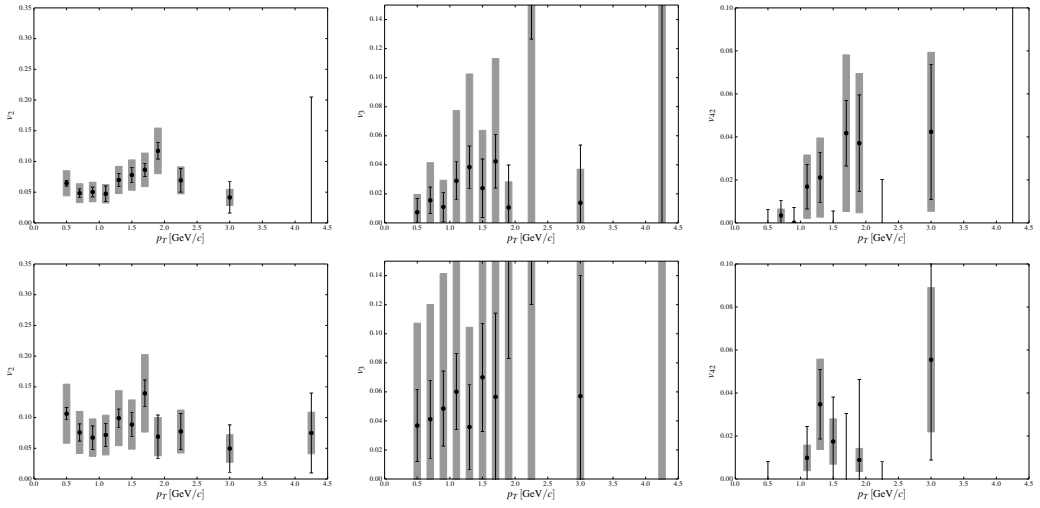

(a) v_2 in 0-60% and 20-60% (b) v_3 in 0-60% and 20-60% (c) $v_4\{\Psi_2\}$ in 0-60% and 20-60%

Figure 4.11: Direct photon v_n in combined centrality bins.

Part III

Discussion

Chapter 5

Discussion of the measurements

In Chapter 3 we have extracted R_γ, which is the ratio of the inclusive photon yield to the yield of photons from hadron decays, from the 2010 data set, which we have combined with an earlier measurement in Section 3.7. To better understand the implications of these measurement for the direct photon yield we will in the following derive the direct photon spectra and study its features. We will use the result from the combined 2007 and 2010 measurements.

5.1 Direct photon momentum spectra

We will transform the 2007+2010-combined R_γ measurements shown in Section 3.7 to direct photon p_T spectra with Eq. (3.6),

$$Y_\gamma^{\text{direct}} = (R_\gamma - 1) Y_\gamma^{\text{hadrons}}. \tag{5.1}$$

The photon yield from hadron decays was already calculated as contribution to the calculation of R_γ, see Section 3.5. We use the decay photon spectra shown in Fig. 3.20. Here the relative uncertainty on the π^0 yield does not drop out as in the cocktail ratio calculated earlier but needs to be taken into account. The calculated direct photon p_T spectra are shown in Fig. 5.1 and Fig. 5.2.

5.2 Excess photon momentum spectra

In heavy-ion collisions direct photons can be produced both from early hard processes and later from interactions due the produced medium. While the first kind is present in $p + p$ collisions as well, the second is unique to heavy-ion collisions. To isolate the signal of photons unique to the heavy-ion environment, we parametrize measurements of direct

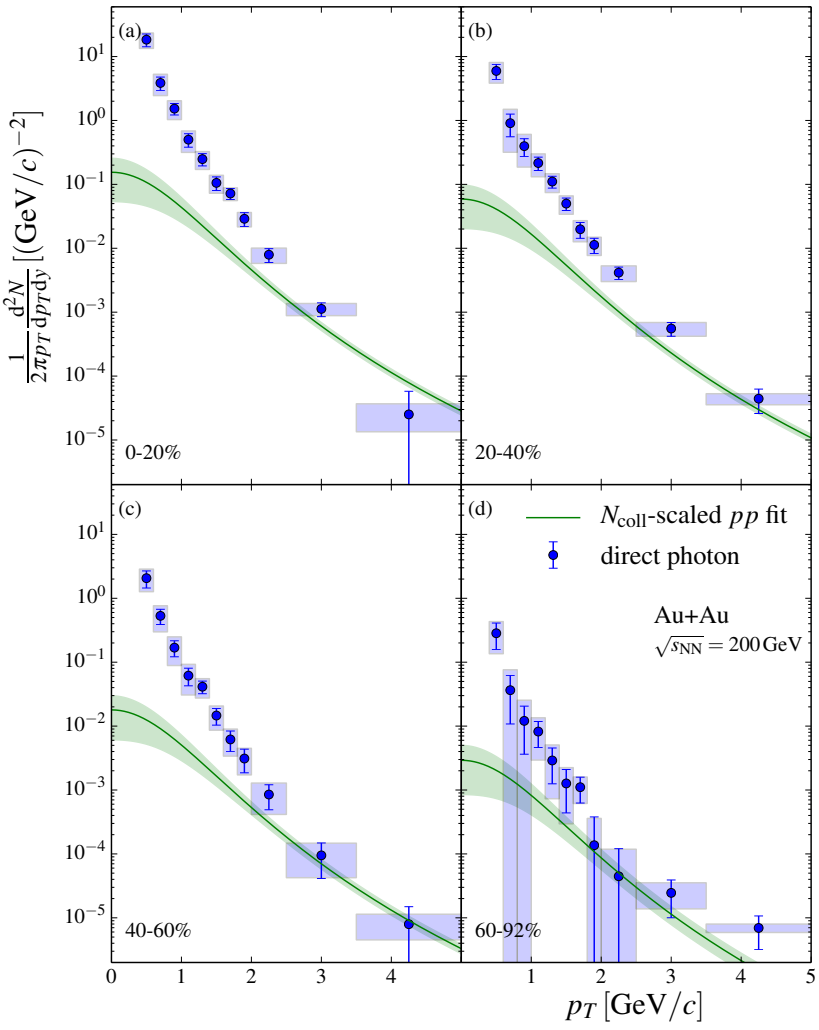

Figure 5.1: Spectra of direct photons in centrality bin 0-20%, 20-40%, 40-60% and 60-92%. The green lines are N_{coll}-scaled parameterizations of the direct photon yield in $p + p$ collisions.

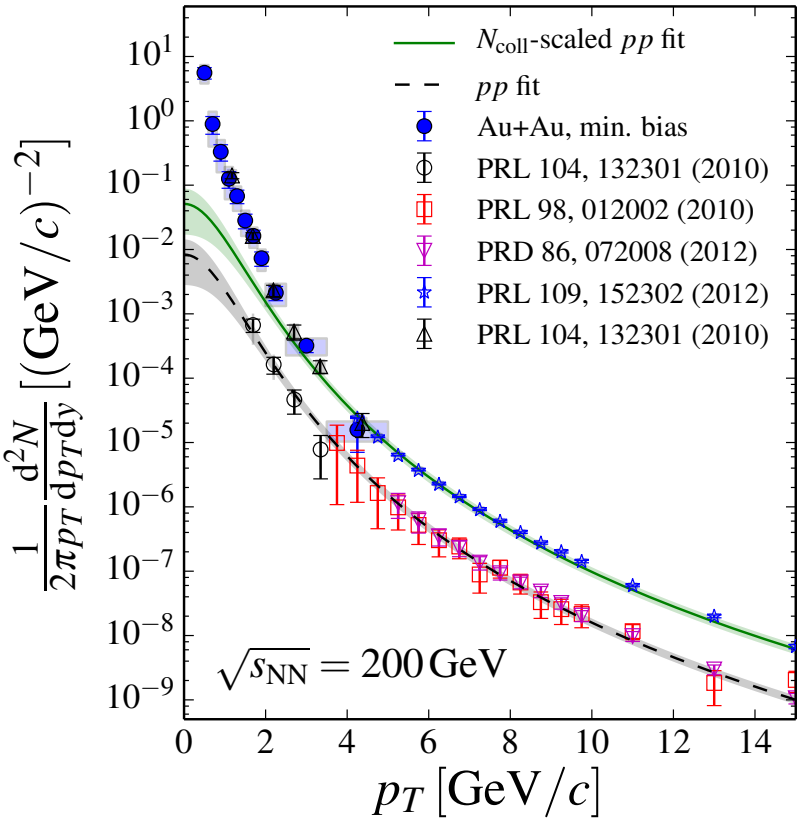

Figure 5.2: Spectrum of direct photons in Au+Au minimum bias and $p+p$ collisions. Full circles are from this measurement in Au+Au. Upwards triangles where measured in Au+Au collisions, open circles in $p+p$ with virtual photons [11]. Open squares and downwards triangles were measured with the calorimeter in $p+p$ collisions in 2003 and 2006, respectively [64, 65]. Open pentagons where measured in Au+Au collisions with the calorimeter in 2004 [66]. The dashed black line is a fit to the combined $p+p$ data, while the full line is the $p+p$ fit scaled to the minimum bias N_{coll}.

photon spectra taken in $p+p$ collisions [11, 64, 65] with a pQCD-inspired functional form

$$\frac{1}{2\pi}\frac{\mathrm{d}^2N}{\mathrm{d}p_T\mathrm{d}y} = a\left(1+\frac{{p_T}^2}{b}\right)^{-c} \tag{5.2}$$

We obtain $a = (8.3 \pm 7.5) \times 10^{-3}$, $b = 2.26 \pm 0.78$ and $c = 3.457 \pm 0.079$. The input data and the fit are shown in Fig. 5.2.

To calculate the yield from hard interactions in each centrality class, we scale the $p+p$ yields with the N_{coll} in each class, where N_{coll} was measured in a Glauber Monte Carlo simulation [67, 68]. The N_{coll} values we are using are listed in Table 5.1. The calculated expectation for direct photons from hard processes is shown in Fig. 5.1 and Fig. 5.2. We find clear indication of an additional direct photon yield at low momenta over the expectation from hard processes.

Table 5.1: The number of nucleon participants N_{part}, number of binary nucleon-nucleon collisions, and constituent-quark participants N_{qpart} measured in a Glauber Monte Carlo [67]. Also shown are the values of local inverse slopes of the excess photon spectra determined in the p_T range 0.6 to 2GeV/c.

centrality	N_{part}	N_{coll}	N_{qpart}	T_{eff} (MeV/c)
0-20%	279.9 ± 5.7	779.0 ± 75.2	735.2 ± 16.2	$239 \pm 25 \pm 7$
20-40%	140.4 ± 7.0	296.8 ± 31.1	333.2 ± 12.2	$260 \pm 33 \pm 8$
40-60%	59.9 ± 5.0	90.6 ± 11.8	126.5 ± 6.8	$225 \pm 28 \pm 6$
60-92%	17.6 ± 4.2	14.5 ± 4.0	30.2 ± 7.1	$238 \pm 50 \pm 6$

We now subtract the direct photon yield from hard processes and arrive at the excess photon p_T spectra shown in Fig. 5.3 and Fig. 5.4. To characterize the shape of the excess photon spectra at low p_T we can parametrize the data with falling exponential functions

$$\frac{1}{2\pi}\frac{\mathrm{d}^2N}{\mathrm{d}p_T\mathrm{d}y} \propto e^{-p_T/T_{\mathrm{eff}}} \tag{5.3}$$

where T_{eff} quantifies the shape of the spectra. For excess photons emitted from a static black body radiator we would expect above expression to be a good description of the spectra, but it was shown that direct photons show large flow in Au+Au collisions, cf. Chapter 4. Since the flow of photons from hard processes is minimal at most, the direct photon flow can be attributed largely to the excess photons. If the photons show considerable flow we expect modifications to their momentum spectra [21]; moreover in this case the inverse

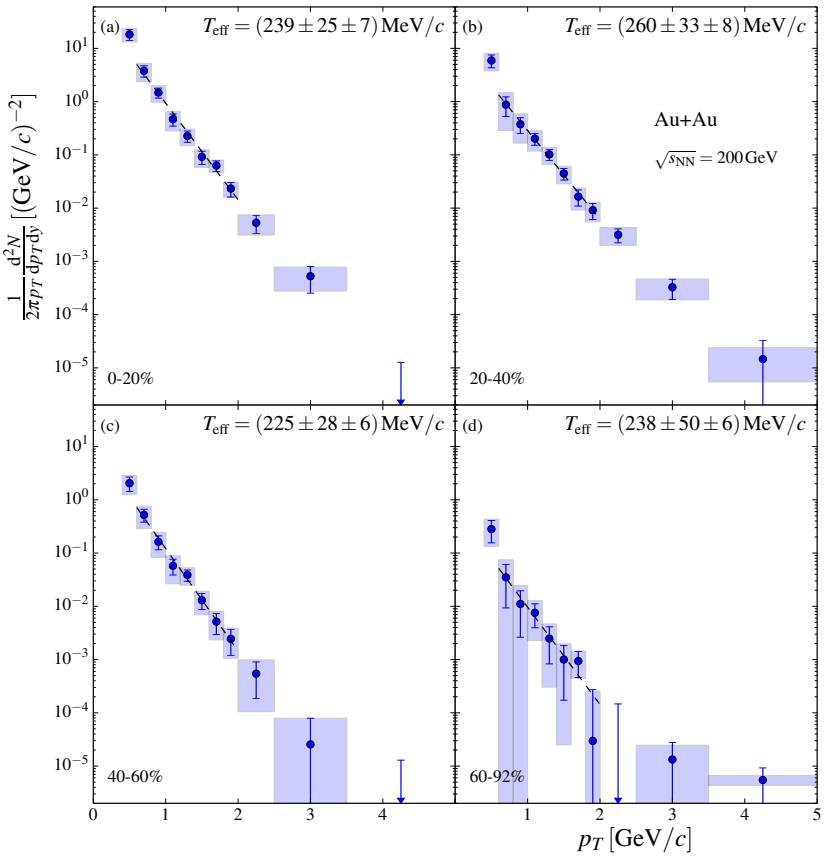

Figure 5.3: Spectrum of excess photons in centrality bin 0-20%, 20-40%, 40-60% and 60-92%. The black line is a fit to an exponential in the range $0.6\mathrm{GeV}/c < p_T < 2.0\mathrm{GeV}/c$.

slope cannot be easily related to the medium temperature anymore [26]. In that sense T_{eff} is strictly a shape parameter for our discussion.

We find strikingly similar inverse slope parameters for the different centralities while the yield varies over more than 2 order of magnitude. The fitted inverse slope values are shown in Table 5.1. We restricted the fit to the momentum range $0.6\,\text{GeV}/c < p_T < 2.0\,\text{GeV}/c$ since the lowest p_T points do not follow the general exponential trend; similarly the spectra noticeably harden towards larger p_T. However when looking at the fit residuals in Fig. 5.5 we find similar deviations from purely exponential shapes across all centralities, underlining the observation that the shape of the excess photon spectrum is not a strong function of centrality.

5.3 N_{part}-dependence of the excess photon yield

To characterize the evolution of the excess photon yield with centrality we can examine the p_T-integrated excess photon yield calculated from the measured invariant yield spectra with

$$\frac{\mathrm{d}N}{\mathrm{d}y} = 2\pi \int_{p_{T,\text{min}}}^{5\,\text{GeV}/c} \mathrm{d}p_T\, p_T \left(\frac{1}{2\pi p_T} \frac{\mathrm{d}^2 N}{\mathrm{d}p_T \mathrm{d}y} \right). \tag{5.4}$$

Here we have integrated from a minimal p_T up to the end of the covered p_T range. However, since the photon spectra are steeply falling in photon p_T any such integrated yield will be dominated by the behavior of the lowest p_T points which contribute most of the yield. For this reason we will study the integrated yield for a number of minimal photon p_T. We have to keep in mind that this procedure yields correlated results since we reuse measurements from same p_T bins for performing different integrations.

The integrated excess photon yields as a function of the number of participants N_{part} are shown in Fig. 5.6 for lower integration limits $p_T = 0.4 \ldots 1.4\,\text{GeV}/c$. We find that the yield has a power-law dependence on N_{part}, i.e. $\mathrm{d}N/\mathrm{d}y \propto N_{\text{part}}^{\alpha}$ with very similar powers independent of the lower integration limit. The fact that we find very similar powers for all lower integration limits is another manifestation of the similar shapes of the excess photon spectra already observed when extracting inverse slopes earlier, and a combined fit of the different results in Fig. 5.6 gives a power $\alpha = 1.48 \pm 0.08(\text{stat}) \pm 0.04(\text{sys})$ which is able to describe the centrality dependence for all considered momentum ranges.

One of the earliest results from RHIC was that the rapidity-integrated charged particle yield is roughly proportional to N_{part} [69]. Deviations from this linear dependence at midrapidity can be understood by considering a mix of soft and hard processes whose scaling behavior depend on the number of participants N_{part} and the number of binary collisions N_{coll}, respectively [70]. The N_{part}-dependence we show here shows a stronger increase with centrality than that seen for charged particles. A recent analysis suggests that a linear scaling behavior for the charged particle yield can be recovered at midrapidity

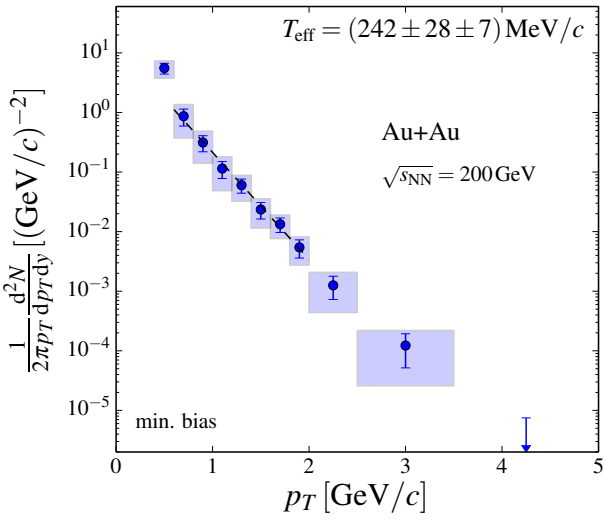

Figure 5.4: Spectrum of excess photons in the minimum bias sample. The black line is a fit to an exponential in the range $0.6\,\mathrm{GeV}/c < p_T < 2.0\,\mathrm{GeV}/c$.

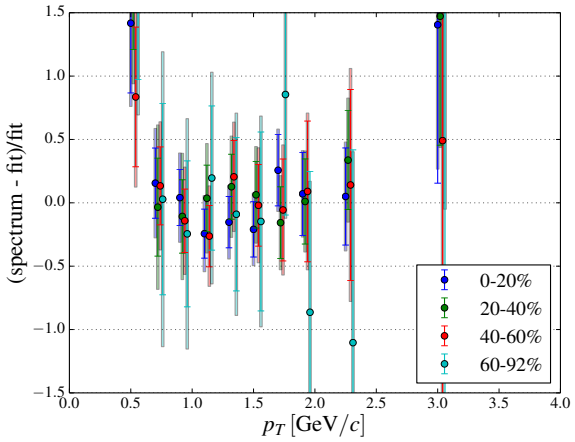

Figure 5.5: Fit residuals for different centralities of exponential fits of excess photon spectra in Fig. 5.3.

when considering the number of participating quarks N_{qpart} instead of nucleons N_{part} [71]. In Fig. 5.7 we show the dependence of the integrated photon yields on N_{qpart}. We do find a scaling behavior $\propto N_{\mathrm{qpart}}^{\alpha}$, albeit with a power α significantly different from unity, $\alpha = 1.31 \pm 0.07(\mathrm{stat}) \pm 0.03(\mathrm{sys})$.

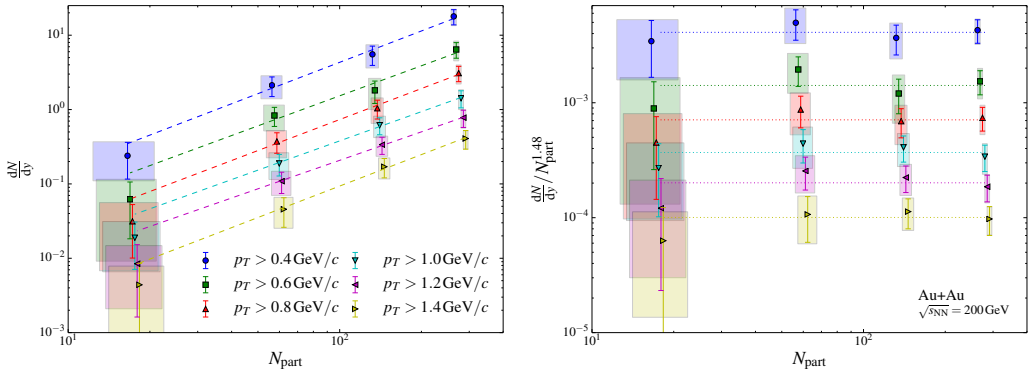

(a) integration limits $p_{T\,\mathrm{min}}$ as functions of N_{part}. The dashed lines are individual fits to power laws $\mathrm{d}N/\mathrm{d}y = AN_{\mathrm{part}}^{\alpha}$.

(b) int. yield normalized by common power law fit

Figure 5.6: Integrated excess photon yield as functions of N_{part}. We find a common power $\alpha = 1.48 \pm 0.08(\mathrm{stat}) \pm 0.04(\mathrm{syst})$.

5.4 Anisotropies v_2 and v_3 in a larger momentum range

We have presented our measurements for the inclusive and direct photon in Chapter 4. In Fig. 5.8 we show for the two most central classes in centrality our results together with the last published PHENIX measurement of the direct photon v_2 [13]. In this measurement photons were reconstructed in the calorimeter. Our photon sample is by construction very pure, but of limited size, especially when going to larger p_T. The sample of photons from the calorimeter is on the other hand much larger, but suffers from backgrounds, e.g. from hadrons, especially at low p_T and is limited to $p_T > 1\,\mathrm{GeV}/c$. Both datasets agree well in the overlap region and follow a smooth trend. While the calorimeter measurement considered in isolation seems to imply a dropping direct photon v_2 towards smaller p_T taking the low p_T direct photon v_2 measured here with conversions into account clearly shows a different trend of a direct photon v_2 flat and non-zero in the low transverse momentum range. A similar observation was made in an earlier analysis of the direct photon v_2 with external conversion pairs in minimum bias data [39, 72] reproduced in

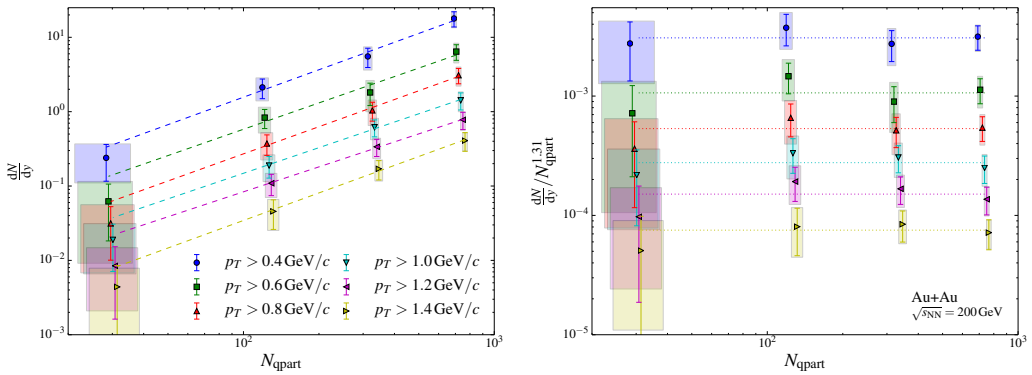

(a) Integrated direct photon yields for different lower integration limits $p_{T\,\mathrm{min}}$ as functions of N_{qpart}. The dashed lines are individual fits to power laws $\mathrm{d}N/\mathrm{d}y = AN_{\mathrm{qpart}}^{\alpha}$.

(b) Integrated yield normalized by common power law fit

Figure 5.7: Integrated excess photon yield as functions of N_{qpart}. We find a common power $\alpha = 1.31 \pm 0.07(\mathrm{stat}) \pm 0.03(\mathrm{sys})$.

Fig. 5.9 which we can confirm here. In Fig. 5.10 we show a comparison to another recent PHENIX analysis of the direct photon v_2 and v_3 using calorimeter photons [73]. We find similarly good agreement as with the published result.

Due to large systematic uncertainties, drawing strong conclusions about the precise values of v_3 is not possible with our measurement. We do, however, measure a v_3 in most central collisions that is non-zero, positive and of similar magnitude as the direct photon v_2 in that centrality. In Fig. 5.10 we show our result for the direct photon v_3 in most central collisions with a measurement from photons reconstructed in the calorimeter [73]. The two results agree inside their large systematic uncertainties. While we observed a flat v_2 in the low transverse momentum range our v_3 measurement tends to imply v_3 becoming smaller as the direct photon p_T decreases.

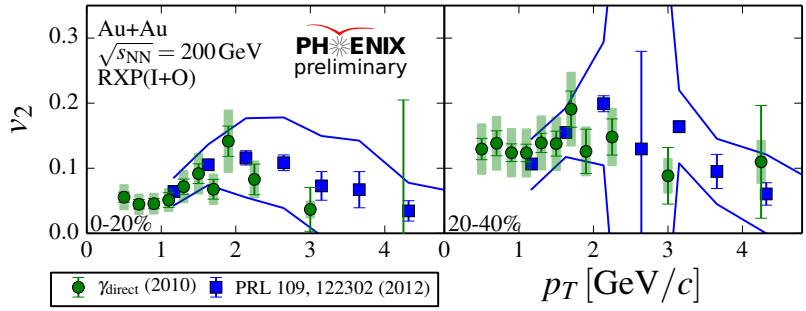

Figure 5.8: Comparison of our direct photon v_2 with the published PHENIX result using calorimeter photons [13]. In that analysis another event plane detector, the BBC, with lower resolution was used.

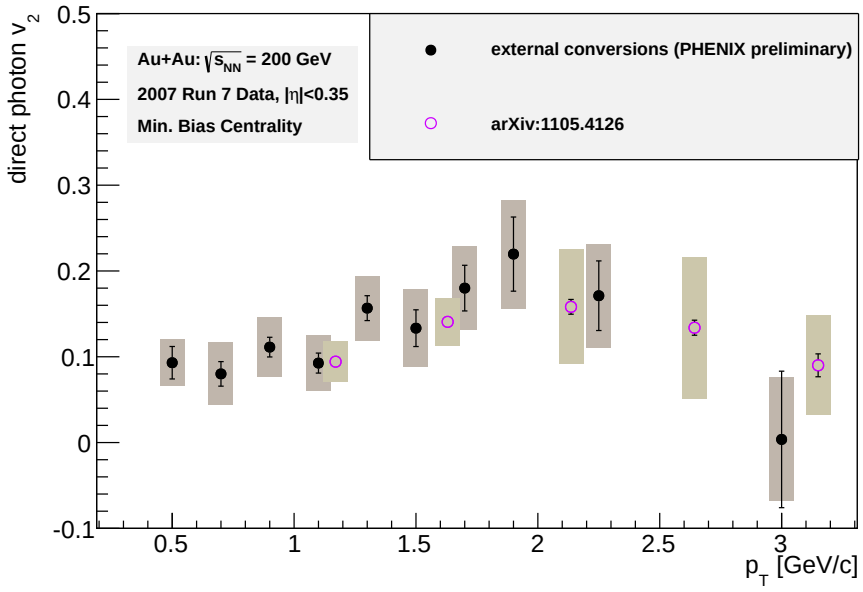

Figure 5.9: Comparison of the preliminary direct photon v_2 measured in external conversion pairs in the 2007 data set [39, 72] with the result using calorimeter photons [13], labeled with the then not yet published arXiv reference. Plot is reproduced from Ref. [39, 72].

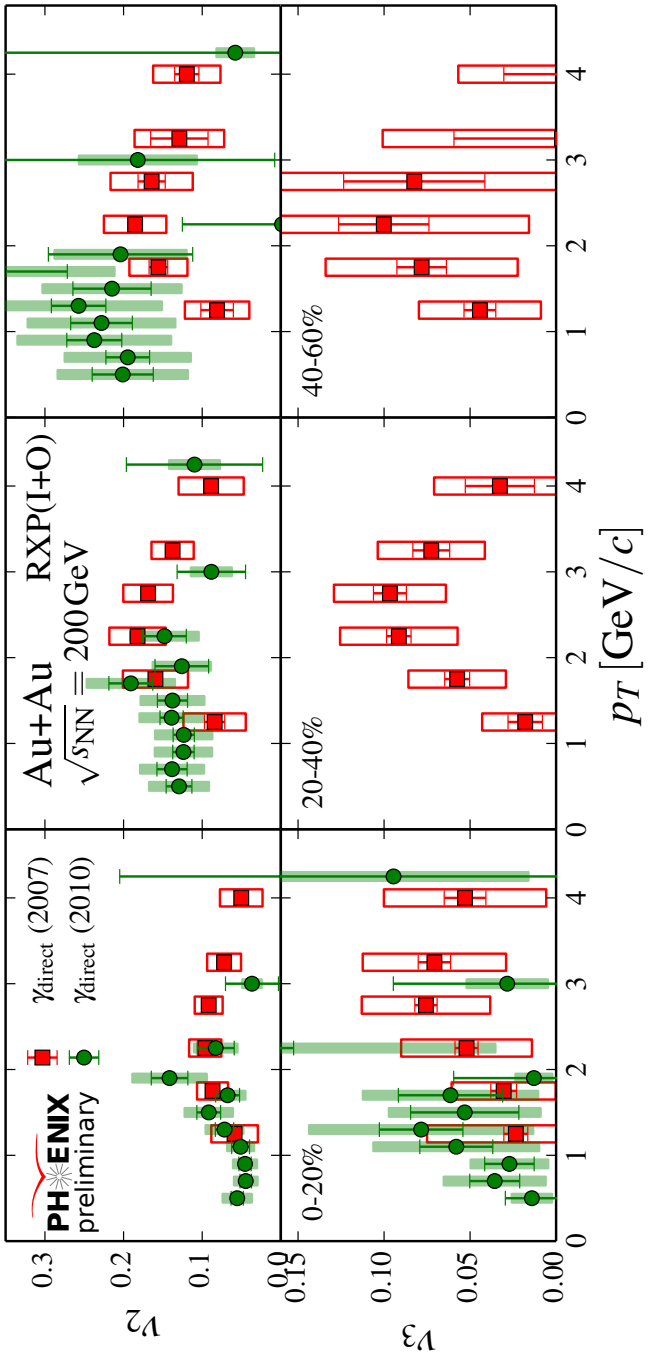

Figure 5.10: Direct photon v_2 and v_3 from this analysis of the 2007 data set using external conversions and from an analysis using photons reconstructed in the calorimeter [73].

Chapter 6

Comparisons with models

6.1 The direct photon yield

The conceptually simplest comparison of our data with models is possible using the direct photon yield. It is strongly related to the total rate of direct photons, but might still show dependency on the dynamics of the medium. In Fig. 6.1 we compare our results to different model calculations. The high-p_T (hard scattering-like) part of the spectrum is usually described reasonably well, yet is not a prediction from the PHSD and fireball models shown here. Instead parameterizations of PHENIX $p+p$ data like shown in 5.2 are used. The shown models tend to consistently predict a yield smaller than seen experimentally in the low p_T range, by factors of 2-3 in the PHSD model by Linnyk *et al.* and the fireball model by van Hees *et al.*, and by more in the hydrodynamic calculation by Shen *et al.*, see Fig. 6.2. Here the first two models include increased photon emission rates in the hadron gas phase which is absent in the hydrodynamic model.

A calculation by Chatterjee *et al.* [74] has found that including fluctuating initial conditions in their ideal hydrodynamic calculation did not increase yield for low p_T direct photons, but instead for the range $p_T > 2\ldots3\,\mathrm{GeV}/c$.

6.2 Centrality-dependence of the direct photon yield

The centrality-dependence of the direct photon yield captures the complex interplay between different mechanisms of direct photon production. While e.g. a QGP medium would have its largest volume in most central collisions, a magnetic field would vanish for vanishing impact parameters $b = 0$. Conversely, very peripheral collisions would create large magnetic fields but only a very small QGP volume.

Recent model calculations have investigated the centrality-dependence of the excess photon yield and confirmed its power-law dependence on N_{part}. In a transport model calculation [19] a power $\alpha \approx 1.5$ with no strong change in spectral shape was found for

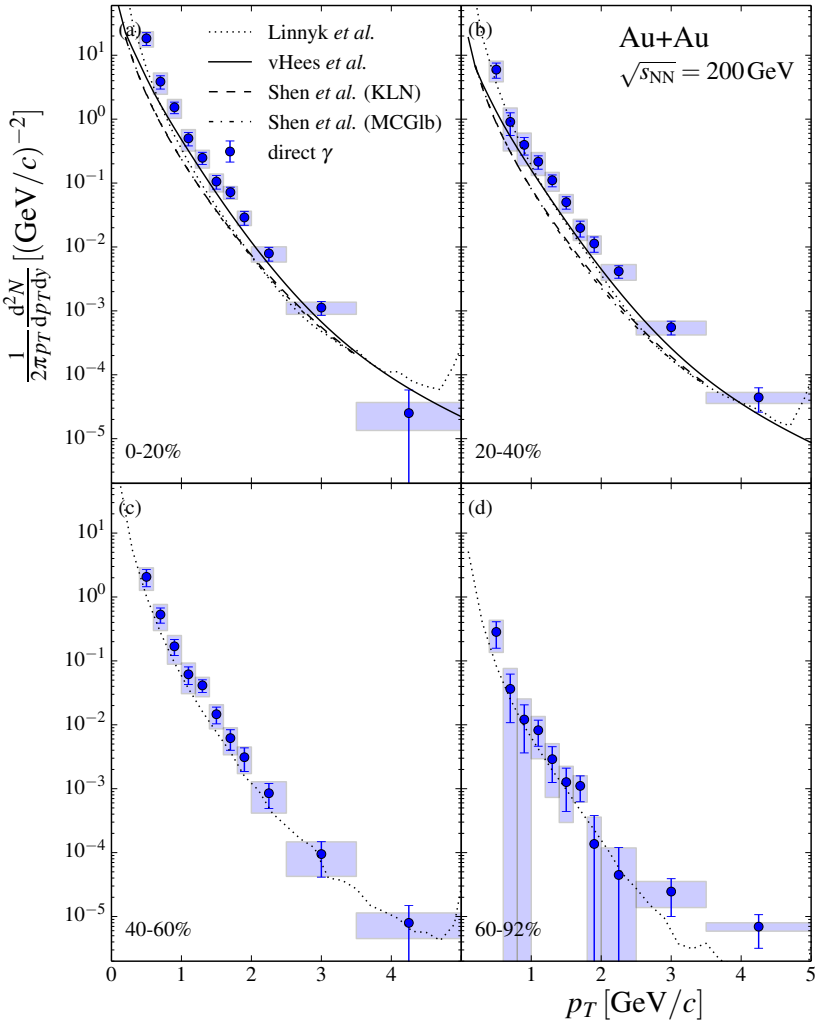

Figure 6.1: Spectra of direct photons in centrality bin 0-20%, 20-40%, 40-60% and 60-92% compared to different model calculations. The dotted lines are from transport calculations in the PHSD framework which includes production from Bremsstrahlung processes in the hadron gas phase [19]; the full lines are from a fireball model [21]; the dashed and dot-dashed lines are from a viscous hydrodynamic model using either KLN or Monte Carlo Glauber initial conditions [26]. The PHSD calculation is a postdiction, all other calculations are predictions. In the PHSD and fireball model a parameterization from data is used to model the hard part of the spectrum.

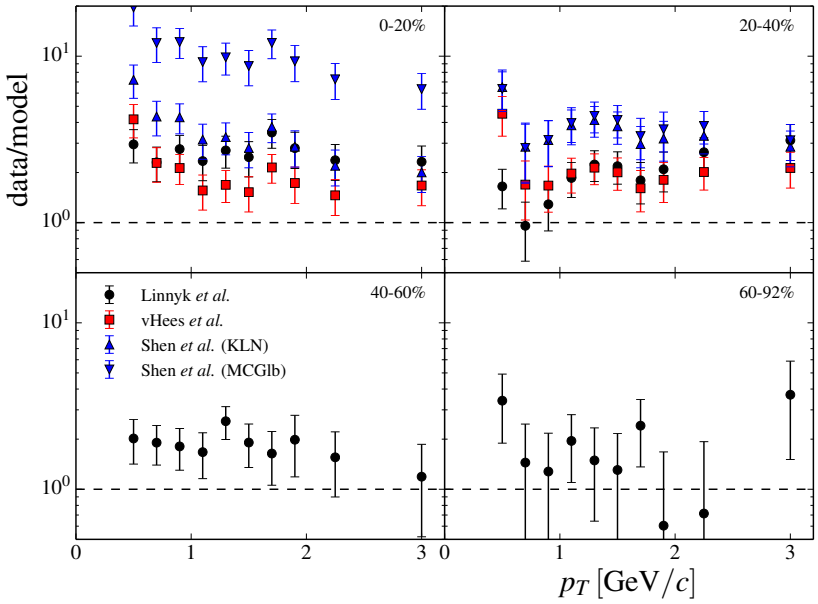

Figure 6.2: Ratio of p_T spectra and different model calculations shown in Fig. 6.1. The details of the models are explained there and in the text.

photons produced in the hadron gas phase, and a power $\alpha \sim 1.75$ for photons from the QGP phase. A similar value was reported from a hydrodynamic calculation of the QGP evolution with powers in the range $1.67 < \alpha < 1.9$ with the power increasing when increasing the lower integration limit [26]. The excess photon yield from a very early Glasma phase is expected to scale with powers $1.47 < \alpha < 2.20$ [29]. We summarize the available predictions in Table 6.1.

The magnetic field created by the colliding nuclei decreases as the nuclei overlap more and more so that they practically vanish in completely central collisions $b = 0$; consequentially one would expect the yield of photons created from the magnetic field [see e.g. 30, 31] to decrease when going to more central collisions, i.e. $\alpha < 0$. However, currently no predictions for the centrality-dependence of the yield in these kinds of models are available.

Currently none of the considered models can capture the experimentally observed direct photon yield in any centrality (the Glasma model predicts a centrality-dependence, but needs to be absolutely normalized with experimental data). The transport calculation in the PHSD framework yields a power law-dependence consistent with the observed value with a model where soft direct photons are produced predominantly as Bremsstrahlung from hadron interactions in the hadron gas phase, but due to opposite trends with N_{part} one would suspect a similar agreement for e.g. a model of production both from strong initial state magnetic fields and a QGP medium with hydrodynamic evolution. Only with

Table 6.1: Power in the N_{part}-dependence of the direct photon yield

	α in $\frac{dN}{dy} = N_{\text{part}}^{\alpha}$
this data	$1.48 \pm 0.08(\text{stat}) \pm 0.04(\text{syst})$
PHSD, hadron gas (transport) [19]	~ 1.5
PHSD, QGP [19]	~ 1.75
OHIO (hydro) [75]	$1.67 \ldots 1.9$
Glasma [29]	$1.47 \ldots 2.20$
magnetic field	< 0 (?)

quantitative consistency with the observed yields will discriminating different scenarios come in reach.

6.3 The direct photon v_2 and v_3

Our measurements of the direct photon v_2 confirm the earlier observation of their considerable flow in most and more central collisions which is of similar size as the flow of light hadrons. Going to more peripheral collisions we see a further increase of the direct photon v_2. At the same time we measured sizable direct photon flow at small photon momenta. We measure a positive v_3, possibly of similar magnitude as v_2, but with uncertainties too large to provide constrains on e.g. predictions of the viscosity of the medium from hydrodynamic calculations [76].

Since the first results of direct photon v_2 in Au+Au collisions were shown, considerable effort has been made to refine their modeling. After considering additional photon production in the hadron gas phase, transport and parametric fireball models [19, 21] predict direct photon elliptic flow closer yet thus far still below to the experimentally observed values, while still being unable to account for the measured yield, cf. Fig. 6.1 and 6.2. In studies of different initial conditions in a hydrodynamic treatment [76] it was found that the predicted dependency was unable to accommodate for the measured absolute values, see Fig. 6.4. While fully accounting for viscous corrections to the hydrodynamic evolution of the medium seems to lead to a decrease in the observed flow of photons, taking fluctuations in the initial conditions into account appears to lead to their increase by a similar amount [see e.g. 24, 25].

Practically all models predict very small v_2 of photons emitted during the QGP phase while photons from the hadron gas phase have v_2 values closer to the experimental data [21] which are similar to the v_2 values observed for hadrons. Additional photon production from e.g. Bremsstrahlung processes in the hadronic phase allows for a larger photon yield from the hadron phase, which after integrating the full time evolution leads to a larger

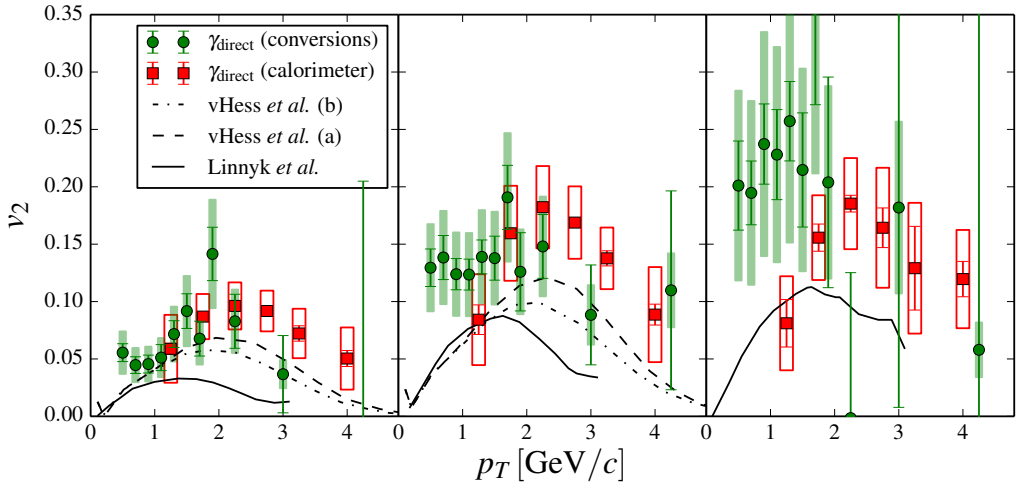

Figure 6.3: Comparison of our measurement of v_2 with two current model predictions. The transport calculation of Linnyk *et al.* [19] includes contributions from hadron interactions in the hadron gas phase and has a systematic uncertainty of about 30% which is not shown here. In the fireball calculation by van Hees *et al.* [21] two different parameterizations of the yield of direct photons from hard scattering processes were used, referred to as model (a) and (b). See the reference for details. This model considers increased direct photon rates in the hadron gas phase. Not shown here is the result from the hydrodynamic model by Shen *et al.* [76] which due to its much smaller prediction values of v_2 is shown separately in Fig. 6.4.

direct photon v_2 decreasing the difference between predicted and measured direct photon v_2.

Most current models predict the direct photon v_2 becoming small for small photon momenta, just as observed for hadrons. This is especially true for photons from the hadronic phase. These predictions seem at odds with our observation of considerable v_2 at small p_T. Photons emitted from the magnetic field in a collision are predicted to have significant v_2 values at small p_T [77]; see 6.5. Unfortunately currently no absolute predictions for the direct photon yield exist for these type of models.

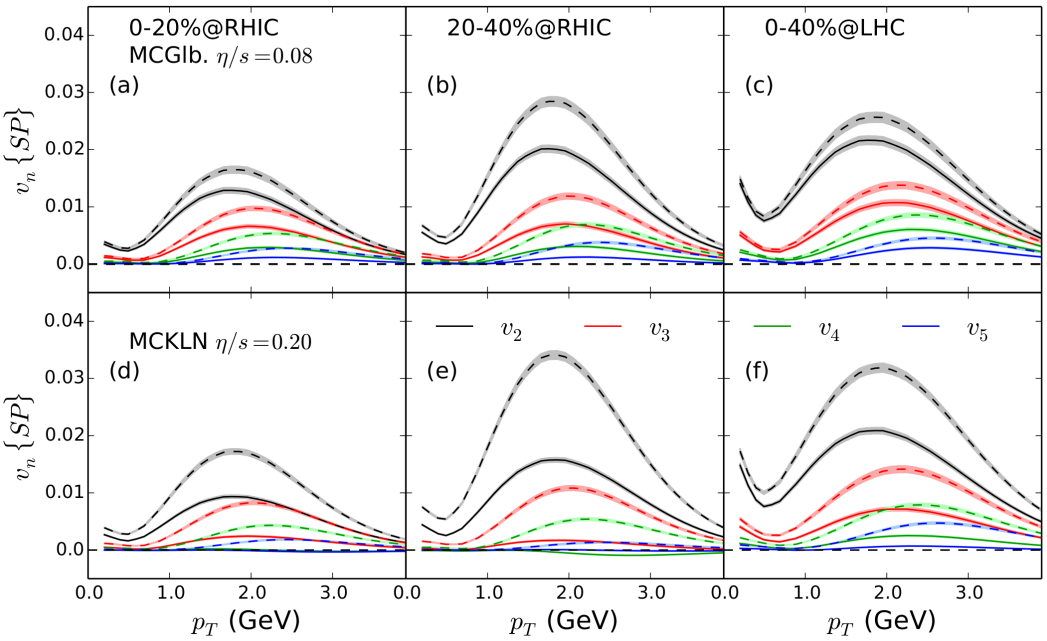

Figure 6.4: Elliptic and triangular flow v_2 and v_3 in the calculation by Shen *et al.* [76].

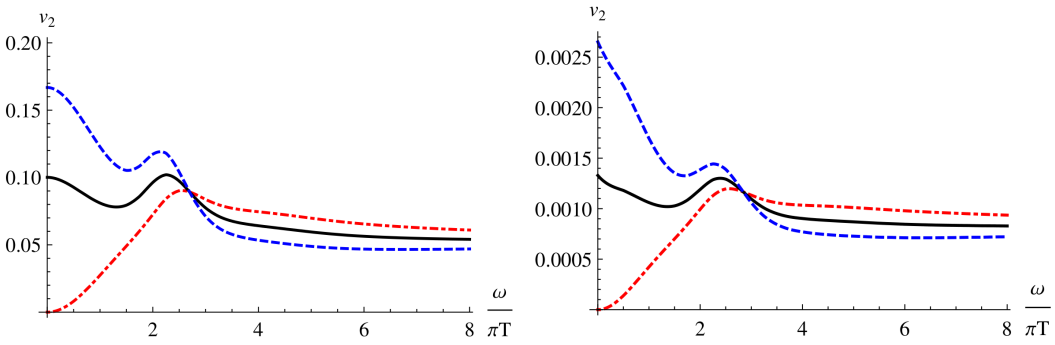

(a) $m = 1.143, B_z = 1(\pi T)^2$ (b) $m = 1.307, B_z = 0.1(\pi T)^2$

Figure 6.5: Elliptical flow of direct photons in the model by Müller *at al.* [77]. Here v_2 is given as a function of a normalized frequency with $p_T \approx \omega$. In this model photons are produced from a strongly coupled medium in a strong magnetic field. Blue curves correspond to photons with in-plane polarizations, the red curves to photons with out-of-plane polarizations. The black curves show the polarization-averaged values. Results for two different magnetic field strengths are given where $B_z = 1(\pi T)^2$ corresponds to $eB = 0.39\,\mathrm{GeV}^2$. Two bare quark masses are considered in the calculation, where $m = 1.143$ stands in for a bare quark mass $M_q \approx 204\,\mathrm{MeV}c^2$.

Chapter 7

Summary and Outlook

In this work we have extracted a high-purity sample of photons down to very low transverse momentum p_T. We have studied the full centrality-dependence of the direct photon yield and for more central collisions found an excess of direct photons at small p_T over the scaled expectation from $p + p$ collisions. While the spectral shape of the excess does not appear to depend on the particular centrality for direct photons in the low momentum range, the yield shows a strong dependence that can be described with a simple power-law relation between the number of participants in the collision and the integrated photon yield, $\frac{\mathrm{d}N}{\mathrm{d}y} = N_{\mathrm{part}}^{\alpha}$. While at RHIC energies, the yield of hadrons at midrapidity is roughly proportional to N_{part}, i.e. $\alpha_{\mathrm{hadrons}} \approx 1$, for soft direct photons we observe $\alpha = 1.48 \pm 0.08(\mathrm{stat}) \pm 0.04(\mathrm{syst})$. Irrespective of remaining model difficulties to accommodate the observed yields on an absolute scale, this simple scaling relation enables qualitative comparison of competing direct photon production scenarios.

As a quantity very sensitive to the dynamics of the system, we have extracted the elliptical and triangular flow v_2 and v_3 of direct photons from our sample extending the range of earlier measurements to much lower momenta. Not only do we find values of v_2 that are much larger than the expectation for photons emitted from e.g. a QGP or even the hadron gas phase, we also find a v_2 that is surprisingly flat down to very small momenta. Currently only very few, early calculations show such a dependence with momentum, and only after their embedding in more complete frameworks will one be able to understand their role. We were able to extract values of v_3 for most central collisions and find markedly positive values which seems to tend towards zero for very small direct photon momenta, though large systematic uncertainties make a full quantitative interpretation difficult.

Since photons have no appreciable final state interaction the observed direct photon signals are sensitive to the full time evolution of the collision, and in the absence of a single, dominant source of direct photons their modeling might require precise tuning of all contributing processes. The results we have shown here map out the dependence of the direct photon yield as a function of centrality of symmetric heavy-ion collisions. However,

in any heavy-ion collision with non-zero impact parameter the colliding nuclei can create strong magnetic fields, have varying initial state geometries, or create QGP or hadron gas media, all of which are related to soft photon observables. For symmetric collisions system like Au+Au which we analyzed here or Pb+Pb studied by ALICE at LHC energies, the relative size of the contribution due to each effect cannot be controlled experimentally: As collision becomes more central with decreasing impact parameter b, both the magnetic fields and the initial state asymmetry get smaller.

However, in an asymmetric system like e.g. d+Au the deuteron can become completely buried in the gold nucleus, forming a roughly spherical initial state, while still creating a magnetic field, albeit of smaller magnitude than in Au+Au collisions; PHENIX has studied soft direct photon production in minimum bias collisions in this system [78]. To be able to compare our Au+Au measurements and the minimum bias d+Au result we approximately scale the photon yield in d+Au and Au+Au to the same number of binary collisions N_{coll} by overlaying the spectra at large p_T, see Fig. 7.1; that is we scale out the dependence on the size of the system. Even though drawing strong conclusions is not possible with the available data the direct photon spectrum in minimum bias d+Au collisions bears a stronger resemblance with the 60-92% than with the 0-20% Au+Au spectrum. A d+Au measurement extending towards lower p_T should make it possible to discriminate among effects due to the magnetic field, the relative size of density fluctuations and e.g. medium lifetime. Similarly, measurements of the direct photon spectra in larger asymmetric systems like U+U, or centrality-dependent measurements in e.g. Cu+Au would allow to study to relative importance of different sources.

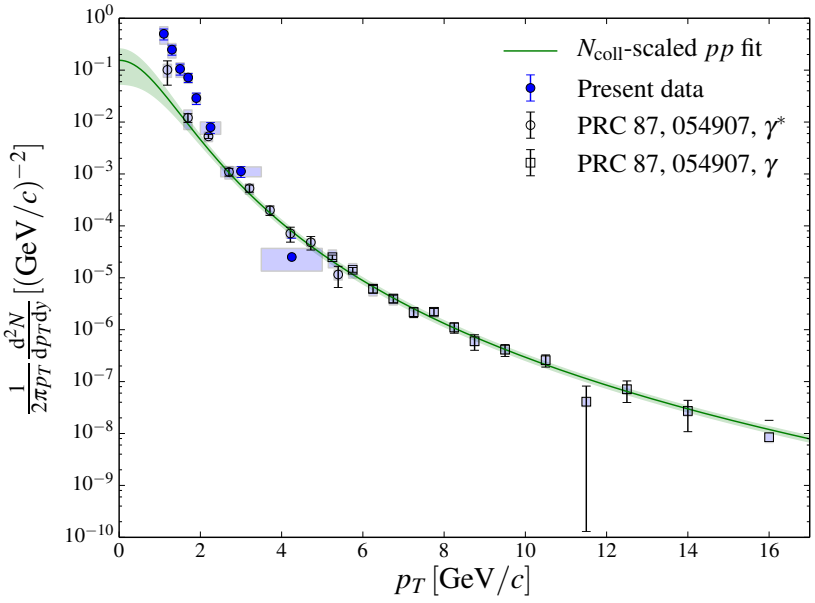

(a) Au+Au 0-20%

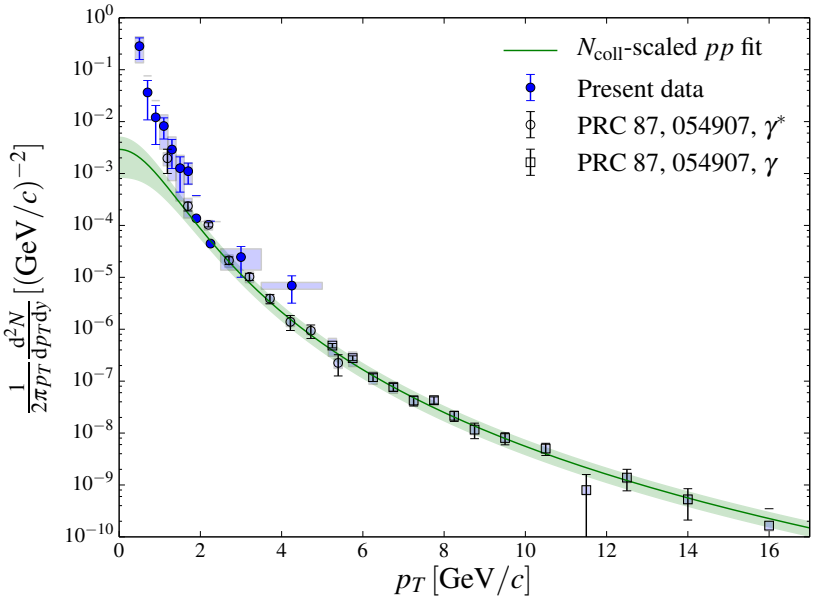

(b) Au+Au 60-92%

Figure 7.1: Direct photon yield in most central and peripheral Au+Au collisions (filled circles) compared with the yield measured in minimum bias d+Au collisions measured in the calorimeter (open squares, γ) and virtual photons (open circles, γ^*) [78]. The yield in d+Au is scaled by eye to the N_{coll} of the respective Au+Au measurement, i.e. such that the yield at large p_T is well described by the N_{coll}-scaled $p+p$ fit.

Bibliography

[1] R. Hagedorn, Nuovo Cim.Suppl. **3**, 147 (1965).

[2] J. Cleymans and D. Worku, Mod.Phys.Lett. **A26**, 1197 (2011), arXiv:1103.1463 [hep-ph] .

[3] E. V. Shuryak, Phys.Rept. **61**, 71 (1980).

[4] I. Arsene *et al.* (BRAHMS collaboration), Nucl.Phys. **A757**, 1 (2005).

[5] B. Back *et al.* (PHOBOS collaboration), Nucl.Phys. **A757**, 28 (2005).

[6] K. Adcox *et al.* (PHENIX Collaboration), Nucl.Phys. **A757**, 184 (2005), arXiv:nucl-ex/0410003 [nucl-ex] .

[7] J. Adams *et al.* (STAR Collaboration), Nucl.Phys. **A757**, 102 (2005), arXiv:nucl-ex/0501009 [nucl-ex] .

[8] R. Hanbury Brown and R. Twiss, Phil.Mag. **45**, 663 (1954).

[9] M. A. Lisa, S. Pratt, R. Soltz, and U. Wiedemann, Ann.Rev.Nucl.Part.Sci. **55**, 357 (2005), arXiv:nucl-ex/0505014 [nucl-ex] .

[10] D. Sharma (PHENIX Collaboration), J.Phys. **G38**, 124082 (2011).

[11] A. Adare *et al.* (PHENIX Collaboration), Phys.Rev.Lett. **104**, 132301 (2010), arXiv:0804.4168 [nucl-ex] .

[12] M. Wilde (ALICE Collaboration), Nucl.Phys. **A904-905**, 573c (2013).

[13] A. Adare *et al.* (PHENIX Collaboration), Phys.Rev.Lett. **109**, 122302 (2012), arXiv:1105.4126 [nucl-ex] .

[14] EMMI Rapid Reaction Task Force "Direct photon flow puzzle", "Report of the EMMI RRTF "Direct photon flow puzzle"," (2014), in preparation.

[15] M. L. Miller, K. Reygers, S. J. Sanders, and P. Steinberg, Ann.Rev.Nucl.Part.Sci. **57**, 205 (2007), arXiv:nucl-ex/0701025 [nucl-ex] .

[16] D. Kharzeev, E. Levin, and M. Nardi, Phys.Rev. **C71**, 054903 (2005), arXiv:hep-ph/0111315 [hep-ph] .

[17] R. Venugopalan, J.Phys. **G35**, 104003 (2008), arXiv:0806.1356 [hep-ph] .

[18] W. Cassing, Nucl.Phys. **A791**, 365 (2007), arXiv:0704.1410 [nucl-th] .

[19] O. Linnyk, W. Cassing, and E. Bratkovskaya, Phys.Rev. **C89**, 034908 (2014), arXiv:1311.0279 [nucl-th] .

[20] S. Turbide, R. Rapp, and C. Gale, Phys.Rev. **C69**, 014903 (2004), arXiv:hep-ph/0308085 [hep-ph] .

[21] H. van Hees, C. Gale, and R. Rapp, Phys.Rev. **C84**, 054906 (2011), arXiv:1108.2131 [hep-ph] .

[22] J. Cleymans, K. Redlich, and D. Kumar Srivastava, Phys.Lett. **B420**, 261 (1998), arXiv:nucl-th/9702004 [nucl-th] .

[23] K. Dusling, Nucl.Phys. **A839**, 70 (2010), arXiv:0903.1764 [nucl-th] .

[24] M. Dion, J.-F. Paquet, B. Schenke, C. Young, S. Jeon, *et al.*, Phys.Rev. **C84**, 064901 (2011), arXiv:1109.4405 [hep-ph] .

[25] G. Vujanovic, J.-F. Paquet, G. S. Denicol, M. Luzum, B. Schenke, *et al.*, (2014), arXiv:1404.3714 [hep-ph] .

[26] C. Shen, U. W. Heinz, J.-F. Paquet, and C. Gale, Phys.Rev. **C89**, 044910 (2014), arXiv:1308.2440 [nucl-th] .

[27] H. Holopainen, S. Rasanen, and K. J. Eskola, Phys.Rev. **C84**, 064903 (2011), arXiv:1104.5371 [hep-ph] .

[28] O. Linnyk, V. Konchakovski, W. Cassing, and E. Bratkovskaya, Phys.Rev. **C88**, 034904 (2013), arXiv:1304.7030 [nucl-th] .

[29] M. Chiu, T. K. Hemmick, V. Khachatryan, A. Leonidov, J. Liao, and L. McLerran, Nucl.Phys. **A900**, 16 (2013), arXiv:1202.3679 [nucl-th] .

[30] D. E. Kharzeev, Prog.Part.Nucl.Phys. **75**, 133 (2014), arXiv:1312.3348 [hep-ph] .

[31] G. Basar, D. E. Kharzeev, and E. V. Shuryak, (2014), arXiv:1402.2286 [hep-ph] .

[32] K. Adcox *et al.* (PHENIX Collaboration), Nucl.Instrum.Meth. **A499**, 469 (2003).

[33] K. Adcox *et al.* (PHENIX Collaboration), Nucl.Instrum.Meth. **A499**, 489 (2003).

[34] M. Aizawa *et al.* (PHENIX Collaboration), Nucl.Instrum.Meth. **A499**, 508 (2003).

[35] L. Aphecetche *et al.* (PHENIX Collaboration), Nucl.Instrum.Meth. **A499**, 521 (2003).

[36] M. Allen *et al.* (PHENIX Collaboration), Nucl.Instrum.Meth. **A499**, 549 (2003).

[37] H. Akikawa *et al.* (PHENIX Collaboration), Nucl.Instrum.Meth. **A499**, 537 (2003).

[38] S. Aronson *et al.* (PHENIX Collaboration), Nucl.Instrum.Meth. **A499**, 480 (2003).

[39] R. M. Petti, *Low Momentum Direct Photons as a Probe of Heavy Ion Collisions*, Ph.D. thesis, Stony Brook University (2013).

[40] M. Chiu (PHENIX Collaboration), AIP Conf.Proc. **915**, 539 (2007), arXiv:nucl-ex/0701031 [nucl-ex] .

[41] E. Richardson *et al.* (PHENIX Collaboration), Nucl.Instrum.Meth. **A636**, 99 (2011), arXiv:1012.0873 [nucl-ex] .

[42] W. Anderson, B. Azmoun, A. Cherlin, C. Chi, Z. Citron, *et al.*, Nucl.Instrum.Meth. **A646**, 35 (2011), arXiv:1103.4277 [physics.ins-det] .

[43] F. Sauli, "Principles of Operation of Multiwire Proportional and Drift Chambers," (1977), CERN-77-09.

[44] J. Mitchell *et al.* (PHENIX Collaboration), Nucl.Instrum.Meth. **A482**, 491 (2002), arXiv:nucl-ex/0201013 [nucl-ex] .

[45] E. Atomssa, J. Sun, B. Bannier, V. K. Khachatryan, A. Drees, and T. Hemmick, "Di-electron analysis for Run 10 Au+Au 200 GeV data using HBD," PHENIX analysis note AN1050.

[46] A. Adare *et al.* (PHENIX Collaboration), Phys.Rev. **C81**, 034911 (2010), arXiv:0912.0244 [nucl-ex] .

[47] R. Averbeck, A. Drees, Y. Akiba, and T. Hachiya, "An electron cocktail for central and peripheral Au+Au collisions at $\sqrt{s_{\mathrm{NN}}} = 130\,\mathrm{GeV}$," PHENIX analysis note 089.

[48] *Geant4 Physics Reference Manual* (2013), `http://geant4.cern.ch/support/userdocuments.shtml`.

[49] S. Adler *et al.* (PHENIX Collaboration), Phys.Rev.Lett. **91**, 072301 (2003), arXiv:nucl-ex/0304022 [nucl-ex] .

[50] S. Adler *et al.* (PHENIX Collaboration), Phys.Rev. **C69**, 034909 (2004), arXiv:nucl-ex/0307022 [nucl-ex] .

[51] S. Adler *et al.* (PHENIX Collaboration), Phys.Rev. **C75**, 024909 (2007), arXiv:nucl-ex/0611006 [nucl-ex] .

[52] A. Adare *et al.* (PHENIX Collaboration), Phys.Rev. **C84**, 044902 (2011), arXiv:1105.3467 [nucl-ex] .

[53] A. Adare *et al.* (PHENIX Collaboration), Phys.Rev. **D83**, 052004 (2011), arXiv:1005.3674 [hep-ex] .

[54] A. Adare *et al.* (PHENIX Collaboration), Phys.Rev. **C87**, 034911 (2013), arXiv:1208.2254 [nucl-ex] .

[55] R. Brun, F. Bruyant, M. Maire, A. McPherson, and P. Zanarini, *GEANT3* (1987), CERN-DD-EE-84-1.

[56] A. M. Poskanzer and S. Voloshin, Phys.Rev. **C58**, 1671 (1998), arXiv:nucl-ex/9805001 [nucl-ex] .

[57] J.-Y. Ollitrault, (1997), arXiv:nucl-ex/9711003 [nucl-ex] .

[58] R. Brun and F. Rademakers, Nucl.Instrum.Meth. **A389**, 81 (1997).

[59] T. Chujo *et al.*, "v_n measurements with respect to the higher order reaction planes Ψ_n defined at forward detectors and via two-particle azimuthal $\Delta\phi$ correlation between central arm tracks and forward detectors," PHENIX analysis note 958.

[60] S. Esumi *et al.*, "Measurements of particle identified higher harmonic flow via event plane method in Run7 Au+Au 200 GeV collisions," PHENIX analysis note 1015.

[61] A. Adare *et al.* (PHENIX Collaboration), Phys.Rev.Lett. **98**, 162301 (2007), arXiv:nucl-ex/0608033 [nucl-ex] .

[62] Y. Gu *et al.*, "Flow measurements based on two particle correlation(2PC) method for identified charged hadrons in Au+Au collisions at $\sqrt{s_{\mathrm{NN}}} = 200\,\mathrm{GeV}$," PHENIX analysis note 1035.

[63] T. Todoroki and other (PHENIX collaboration), "Measurements of identified particle higher harmonic flow in Au+Au collisions at $\sqrt{s_{\mathrm{NN}}} = 200$ gev," In preparation for submission to PRL.

[64] S. Adler *et al.* (PHENIX Collaboration), Phys.Rev.Lett. **98**, 012002 (2007), arXiv:hep-ex/0609031 [hep-ex] .

[65] A. Adare *et al.* (PHENIX Collaboration), Phys.Rev. **D86**, 072008 (2012), arXiv:1205.5533 [hep-ex] .

[66] S. Afanasiev *et al.* (PHENIX Collaboration), Phys.Rev.Lett. **109**, 152302 (2012), arXiv:1205.5759 [nucl-ex] .

[67] K. Reygers, *Results of Au+Au Glauber Calculations*, Tech. Rep. (PHENIX collaboration internal report, `https://www.phenix.bnl.gov/WWW/p/draft/reygers/glauber/tables_auau_200gev.html`, 2003).

[68] B. Alver, M. Baker, C. Loizides, and P. Steinberg, (2008), arXiv:0805.4411 [nucl-ex] .

[69] B. B. Back *et al.* (PHOBOS Collaboration), Phys. Rev. Lett. **85**, 3100 (2000).

[70] X.-N. Wang and M. Gyulassy, Phys.Rev.Lett. **86**, 3496 (2001), arXiv:nucl-th/0008014 [nucl-th] .

[71] S. Adler *et al.* (PHENIX Collaboration), Phys.Rev. **C89**, 044905 (2014), arXiv:1312.6676 [nucl-ex] .

[72] A. Drees (PHENIX collaboration), Nucl.Phys. **A910-911**, 179 (2013).

[73] S. Mizuno, "Higher order azimuthal anisotropy of direct photon in Run7 Au+Au $\sqrt{s}_{NN} = 200$ GeV," PHENIX analysis note 1092.

[74] R. Chatterjee, H. Holopainen, T. Renk, and K. J. Eskola, (2012), arXiv:1207.6917 [nucl-th] .

[75] U. W. Heinz, J. Liu, and C. Shen, (2014), arXiv:1403.8101 [nucl-th] .

[76] C. Shen, U. W. Heinz, J.-F. Paquet, I. Kozlov, and C. Gale, (2013), arXiv:1308.2111 [nucl-th] .

[77] B. Muller, S.-Y. Wu, and D.-L. Yang, Phys.Rev. **D89**, 026013 (2014), arXiv:1308.6568 [hep-th] .

[78] A. Adare, S. Adler, S. Afanasiev, C. Aidala, N. Ajitanand, *et al.*, Phys.Rev. **C87**, 054907 (2013), arXiv:1208.1234 [nucl-ex] .